

Electronic Thesis and Dissertation Repository

3-2-2021 10:40 AM

Galvanic Corrosion of Carbon Steel Coupled to Copper in Used Nuclear Fuel Containers


Lindsay J. Braithwaite, *The University of Western Ontario*

Supervisor: Noël, James J., *The University of Western Ontario*

A thesis submitted in partial fulfillment of the requirements for the Master of Science degree in Chemistry

© Lindsay J. Braithwaite 2021

Follow this and additional works at: <https://ir.lib.uwo.ca/etd>

 Part of the [Analytical Chemistry Commons](#), [Materials Chemistry Commons](#), and the [Physical Chemistry Commons](#)

Recommended Citation

Braithwaite, Lindsay J., "Galvanic Corrosion of Carbon Steel Coupled to Copper in Used Nuclear Fuel Containers" (2021). *Electronic Thesis and Dissertation Repository*. 7676.
<https://ir.lib.uwo.ca/etd/7676>

This Dissertation/Thesis is brought to you for free and open access by Scholarship@Western. It has been accepted for inclusion in Electronic Thesis and Dissertation Repository by an authorized administrator of Scholarship@Western. For more information, please contact wlsadmin@uwo.ca.

Abstract

Deep geological containment of used nuclear fuel will rely on multiple engineered and natural barriers, two of which are the copper-coated used fuel containers and the compacted bentonite clay buffer boxes in which the containers will rest. This work focused on possible galvanic interactions between the copper coating and the steel substrate of the container, which may occur at a hypothetical through-coating defect. In the presence of various amounts of chloride, bentonite, and oxygen, corrosion of the copper/carbon steel couple was studied using electrochemical tests complemented by surface characterization and 3D X-ray imaging. We investigated the effects of copper-to-steel area ratio, chloride, bentonite, and coating technique on corrosion of the carbon steel. This work provided insight into the conditions which may exacerbate or mitigate galvanic corrosion in the deep geological repository, contributing to the body of research which will support prediction of the long-term performance of the used fuel container.

Key words: copper, steel, galvanic corrosion, chloride, bentonite clay, electrochemistry, nuclear

Summary for Lay Audience

The long-term management of used nuclear fuel is an important aspect of the continued viability of nuclear energy, which is one of Canada's largest sources of reliable, carbon-free electricity. A deep geological repository has been proposed to provide containment and isolation of the used fuel bundles for up to one million years, at which point the radioactivity of the fuel will have decayed to ambient levels. Multiple barriers will be in place to contain the harmful radionuclides, but the focus of this work is the copper-coated carbon steel used fuel container, which houses the fuel bundles, and the bentonite clay which surrounds it. Corrosion will be an ongoing threat to container integrity once the container is placed in the repository, though if intact, the copper coating is predicted to provide adequate protection. However, in the scenario of a defect penetrating through the copper coating to the steel substrate, galvanically accelerated corrosion of the steel substrate would be possible.

This work seeks to investigate several aspects of such a system: the effective copper-to-steel area ratio, groundwater chloride concentration, oxygen availability (as some oxygen will be trapped upon closure), presence of bentonite, and nature of the copper/steel interface, and how these aspects affect the corrosion of carbon steel. Immersion tests, electrochemical tests, surface characterization, and X-ray imaging were used to evaluate the corrosion behaviour of steel galvanically coupled to copper. The corrosion of the steel was found to be less severe when copper-to-steel area ratio was low (which can be achieved in low conductivity environments) and when bentonite was present, due to its role as a barrier to transport oxygen.

These studies provide key insights into the interactions between the copper/steel galvanic couple and the repository environment, laying the groundwork for future studies in compacted bentonite and long-term oxidants like sulphide. Due to the impracticality of performing laboratory experiments on the time scales relevant to the deep geological repository, this research contributes to the building of predictive models for how the used fuel containers will perform during long-term containment, and ultimately, the licensing basis for the repository itself.

Co-Authorship Statement

Chapter One: Written by Lindsay Braithwaite (100%); reviewed by Dr. James Noël.

Chapter Two: Written by Lindsay Braithwaite (100%); reviewed by Dr. James Noël.

Chapter Three: Experimental design by Dr. Thalia Standish (75%) with input from Dr. David Shoesmith and Dr. James Noël. Experiments were conducted by Lindsay Braithwaite (90%) with some assistance from Dr. Thalia Standish, and surface analysis was conducted by Lindsay Braithwaite and Dr. Thalia Standish together (90%). Data was plotted by Lindsay Braithwaite (90%) and results were interpreted with input from Dr. Thalia Standish, Dr. David Shoesmith, and Dr. James Noël (Lindsay Braithwaite: 35%). The original draft of the manuscript¹ was written by Dr. Thalia Standish with input from Lindsay Braithwaite (10%), and Dr. James Noël and Lindsay Braithwaite assisted in revision of the manuscript (Lindsay Braithwaite: 20%). The chapter was written by Lindsay Braithwaite and reviewed by Dr. James Noël.

Chapter Four: Experimental design by Lindsay Braithwaite (90%) with input from Dr. James Noël. Experiments were conducted by Lindsay Braithwaite (75%) and Katarina Albrechtas (25%). Experiments in Section 4.3.4 relied on software built by Dr. Dmitrij Zagidulin. Data was plotted by Lindsay Braithwaite (85%) and Katarina Albrechtas (15%) and results were interpreted with input from Dr. James Noël and Dr. David Shoesmith. The chapter was reviewed by Dr. James Noël.

Chapter Five: Experimental design by Lindsay Braithwaite (85%) with input from Dr. Thalia Standish and Dr. James Noël. Experiments were conducted by Lindsay Braithwaite (99%) with some assistance from Dr. Thalia Standish. Data was plotted by Lindsay Braithwaite and interpreted by Lindsay Braithwaite and Dr. James Noël. The chapter was written by Lindsay Braithwaite and reviewed by Dr. James Noël.

Chapter Six: Written by Lindsay Braithwaite (100%); reviewed by Dr. James Noël.

¹ T. E. Standish, L. J. Braithwaite, D. W. Shoesmith, J. J. Noël, Influence of area ratio and chloride concentration on the galvanic coupling of copper and carbon steel, *J. Electrochem. Soc.* 166 (2019) C34489–C3455

Acknowledgements

My time at Western University is coming to a bittersweet close. I would like to first acknowledge this school as the place where I learned more about myself than I thought there was to know, met mentors who built me up to be curious and resilient, and made friends who will be in my heart no matter where I go next. I cannot think of a better place to have spent the last seven years.

I'd like to thank my supervisor, Dr. James Noël, for believing in me every step of the way. Thank you for giving me the opportunity to see the world and for going out of your way, however conspicuously, to connect me with people in my field. Thank you for our thoughtful discussions, for challenging me, and for your unwavering support. I am grateful to have had the opportunity to be mentored by you. I am also grateful for your seemingly endless supply of dad jokes and garden trivia. Your wisdom will stay with me always and I will look back on my time in the Noël lab with only fondness.

To Dr. David Shoesmith, I'd like to express my thanks for your ongoing support and mentorship. I am lucky to have had the chance to work under your supervision; I will always be a bottom feeder at heart. I will miss your impeccably delivered jokes, but even more, I will miss your intellectual generosity. I hope retirement sees you atop many mountains, breathing the fresh air, and enjoying the view.

Dr. Thalia Standish, who laid the groundwork for this research, was a wonderful mentor. Thalia, you are a skilled scientist and teacher. I am grateful to have built my thesis on a foundation of work that was as careful and thorough as yours. Thank you for all you taught me and your ongoing support.

Thank you to Dr. Dmitrij Zagidulin and Dr. Jian Chen for all you do to keep the lab functioning; I am quite sure there is much more work behind the scenes than I am even aware. Dmitrij, the software you built made this thesis possible, and your expertise has been instrumental in my training – thank you. Jian, thank you for your wise words and insightful feedback. The help that you've given me and all the graduate students makes an enormous difference.

It has been an honour to work with Dr. Sridhar Ramamurthy, one of the kindest people I have met. Sridhar, thank you for the interest you took in my project and thank you for believing in me. I will

always appreciate that you are not only on all the right mailing lists, but that you made sure the opportunities that landed in your inbox landed in mine too.

I have had the good fortune to have worked with the very talented scientists and professionals at Surface Science Western. Thank you to Brad Kobe for training me on the SEM instruments, Dr. Thalia Standish for teaching me Raman spectroscopy, and Ivan Barker for allowing me to tie up the X-ray micro-CT as often as I did. My work also depended heavily on the skilled professionals at the University Machine Shop. I'd like to thank Ian Vinkenvleugel for his work and his patience.

The graduate and undergraduate students of the Noël-Shoesmith lab have been wonderful friends and colleagues. I must thank Katarina Albrechtas, whose excellent work helped make chapter four of this thesis possible. I would also like to thank my fellow office 6B occupants for all the great conversations and all the laughs. I hope to get tea with you again soon. This lab was a uniquely wonderful cast of characters, every single one of whom has left a lasting impression on me. I am very lucky to have been part of a community as talented and kindhearted as them.

This research was funded under the Collaborative Research and Development Grant (CRDPJ507465e16) agreement between the Natural Sciences and Engineering Research Council of Canada (NSERC, Ottawa) and the Nuclear Waste Management Organization (NWMO, Toronto). Thank you to Dr. Mehran Behazin, Dr. Pete Keech, and Dr. Jeff Binns from NWMO for supporting this project and giving my research such clear purpose.

Finally, I would like to thank my family, friends, and partner for their unconditional support. I cannot stress enough how much it means to have a group of people who are always there to encourage me or lend an ear when I need one. Thank you for seeing me through.

This thesis is dedicated to my parents, my brother, my partner,
and my cat, Mouse, who got me through 2020.

Table of Contents

Abstract.....	i
Summary for Lay Audience.....	ii
Co-Authorship Statement.....	iii
Acknowledgements.....	iv
Table of Contents.....	vii
List of Acronyms, Abbreviations, and Symbols.....	x
List of Acronyms and Abbreviations.....	x
List of Symbols.....	xi
List of Tables.....	xiv
List of Figures.....	xv
1. Introduction.....	1
1.1 Risks of Galvanic Corrosion in Corrosion-Resistant Metallic Coatings.....	1
1.2 Evolution of Conditions in the DGR.....	3
1.3 Overview of Corrosion at a Through-Coating Defect.....	4
1.4 Functions and Properties of the Bentonite Clay.....	5
1.5 Carbon Steel Corrosion and Carbon Steel as the Anode.....	6
1.6 Copper Corrosion and Copper as the Cathode.....	9
1.7 Gaps in Research and Research Goals.....	11
1.8 References.....	13
2. Methods and Materials.....	16
2.1 Fundamentals of Galvanic Corrosion.....	16
2.2 Electrochemical Techniques.....	21
2.2.1 Galvanic Coupling at the Open Circuit Potential (OCP).....	21
2.2.2 Potentiodynamic Polarization (PDP).....	22
2.2.3 Linear Polarization Resistance (LPR).....	23
2.2.4 Electrochemical Impedance Spectroscopy (EIS).....	24
2.3 Surface Analysis and Imaging Techniques.....	28
2.3.1 Raman Spectroscopy.....	28
2.3.2 Scanning Electron Microscopy (SEM) and Energy Dispersive X-ray (EDX) Analysis.....	31

2.3.3 X-ray Micro-computed Tomography (micro-CT).....	32
2.4 Materials.....	33
2.4.1 A516 grade 70 Carbon Steel.....	33
2.4.2 SKB Wrought Copper	34
2.4.3 Electrodeposited Copper-Coated Steel.....	34
2.4.4 Cold Spray Copper-Coated Steel.....	35
2.5 References	36
3. Galvanic Coupling of Carbon Steel and Copper in Chloride	38
3.1 Introduction	38
3.2 Experimental Methods	39
3.2.1 Sample Preparation.....	39
3.2.2 Experimental Setup.....	40
3.2.3 Surface Analysis.....	41
3.3 Results	41
3.3.1 Galvanic Coupling at Different Copper-to-Steel Area Ratios.....	41
3.3.2 Surface Analysis of Carbon Steel Corroded at Different Copper-to-Steel Area Ratios.....	44
3.3.3 Prediction of Coupled Potential and Galvanic Current by PDP.....	49
3.3.4 Effect of Chloride Concentration and Oxygen Availability	51
3.4 Discussion	56
3.5 Conclusions	59
3.6 References	61
4. Galvanic Coupling of Copper and Carbon Steel in the Presence of Bentonite Clay and Chloride.....	63
4.1 Introduction	63
4.2 Experimental Methods	65
4.2.1 Sample Preparation.....	65
4.2.2 Galvanic Coupling Experiments.....	65
4.2.3 EIS Experiments	66
4.2.4 Surface Analysis	67
4.3 Results	67
4.3.1 Copper-to-Steel Area Ratio Effects in the Presence and Absence of Bentonite	67
4.3.2 Effects of Bentonite Layer Thickness	68
4.3.3 Surface Analysis of Carbon Steel.....	71

4.3.4 EIS of Carbon Steel and Copper in Various Amounts of Bentonite	77
4.4 Discussion	83
4.5 Conclusions	85
4.6 References	86
5. Galvanic Corrosion at a Through-Coating Defect in the Presence of Chloride and Bentonite	89
5.1 Introduction	89
5.2 Experimental Methods	91
5.2.1 Sample Preparation.....	91
5.2.2 Experimental Setup.....	92
5.2.3 X-ray micro-CT	93
5.2.4 Surface Analysis	93
5.3 Results	94
5.3.1 Electrochemistry Results for Electrodeposited Cu-coated Samples.....	94
5.3.2 Corrosion Volume Analysis of Electrodeposited Samples by X-ray Micro-CT	96
5.3.3 Electrochemistry Results for Cold Sprayed Cu-coated Samples.....	100
5.3.4 Corrosion Volume Analysis of Cold-sprayed Samples by X-ray Micro-CT	101
5.3.5 Surface Analysis of Vertical Cross Sections	105
5.4 Discussion	109
5.5 Conclusions	112
5.6 References	115
6. Conclusions and Future Work	117
6.1 Conclusions	117
6.2 Future Work	119
6.3 References	122
Appendix A: Copyright Information	Error! Bookmark not defined.
Curriculum Vitae	124

List of Acronyms, Abbreviations, and Symbols

List of Acronyms and Abbreviations

AC	alternating current
CANDU	Canada Deuterium Uranium
CPE	constant phase element
CS	carbon steel
CT	computed tomography
DC	direct current
EDX	energy dispersive X-ray
EIS	electrochemical impedance spectroscopy
KBS-3	kärnbränslesäkerhet (Swedish, translation: nuclear fuel safety)
LPR	linear polarization resistance
MIC	microbially influenced corrosion
NDE	non-destructive examination
NRC	National Research Council
NWMO	Nuclear Waste Management Organization
OCP	open circuit potential
PDP	potentiodynamic polarization
PTFE	polytetrafluoroethylene
SCE	saturated calomel electrode
SEM	scanning electron microscope
SHE	standard hydrogen electrode
SKB	Svensk Kärnbränslehantering Aktieföretag (Swedish, translation: Swedish Nuclear Fuel Management LLC)
SSD	silicon drift detector
TCE	tetrachloroethylene
UFC	used fuel container
ZRA	zero-resistance ammeter

List of Symbols

A	wetted surface area
A_{CS}	wetted surface area of carbon steel
ads	adsorbed
aq	aqueous
$A_{X\text{-ray}}$	absorbance of X-rays
C	capacitance
C_{dl}	capacitance of the electric double layer
C_{Fe}	weight fraction of Fe in A516 gr. 70 carbon steel
CPE_{bent}	constant phase element associated with bentonite
CPE_{dl}	constant phase element associated with electric double layer
CPE_{film}	constant phase element associated with the oxide film
C_m	concentration of electrolyte “m”
d_{A516}	density of A516 gr. 70 carbon steel
E	potential
e^-	electron
E^0	standard potential
E_{corr}	corrosion potential
E_{corr}^{CS}	corrosion potential of carbon steel
E_{corr}^{Cu}	corrosion potential of copper
E_{eq}	equilibrium potential
E_g	coupled potential
F	Faraday’s constant ($96,485 \text{ J C}^{-1}$)
f	frequency
G	Gibbs free energy
i	current density
I	current
I_0	exchange current
I_a^{CS}	anodic current on carbon steel
I_{corr}	corrosion current

$I_{\text{corr}}^{\text{CS}}$	corrosion current of carbon steel
$I_{\text{corr}}^{\text{Cu}}$	corrosion current of copper
I_g	galvanic current
I_{in}	intensity of incoming X-rays
I_{net}	net current
I_{out}	intensity of outgoing X-rays
K	equilibrium constant
k_m	Setschenow salt parameter for electrolyte “m”
K_{sp}	solubility constant
L	inductance
l	liquid
m	symbol representing an electrolyte (generic)
m_{Fe}	mass of Fe
n	number of moles of electrons
pH	power of hydrogen
R	universal gas constant ($8.314 \text{ C V mol}^{-1} \text{ K}^{-1}$)
R	resistance
R_{bent}	resistance due to bentonite
R_{ct}	charge transfer resistance
R_{film}	resistance due to the oxide film
$R_{\text{interfacial}}$	total resistance due to interfacial reactions
R_L	inductive resistance
R_p	polarization resistance
$R_{p,\text{CS}}$	polarization resistance of carbon steel
$R_{p,\text{Cu}}$	polarization resistance of copper
R_{pore}	resistance due to a pore
R_s	solution resistance
s	solid
S_{O_2}	solubility of oxygen in electrolyte “m”
$S_{\text{O}_2}^0$	solubility of oxygen in pure water

T	temperature
t	sample thickness
V_{corroded}	corroded volume
W	Warburg impedance element
Y	admittance
Z	impedance
Z'	impedance (real)
Z''	impedance (imaginary)
α	transfer coefficient
β	Tafel slope
β_1	Tafel slope of reaction step 1
β_2	Tafel slope of reaction step 2
β_A^{CS}	Tafel slope of the anodic reaction on carbon steel
β_A^{Cu}	Tafel slope of the anodic reaction on copper
β_C^{CS}	Tafel slope of the cathodic reaction on carbon steel
β_C^{CS}	Tafel slope of the cathodic reaction on carbon steel
θ	phase shift
ϑ	surface coverage of an adsorbed intermediate
ϑ_{SS}	steady-state surface coverage of an adsorbed intermediate
μ	linear attenuation coefficient
σ	Warburg coefficient
τ	time constant
φ	Total number of sites on a surface at monolayer coverage
ω	angular frequency

List of Tables

Table 2.1: Impedance functions for AC circuit elements.....	25
Table 2.2: Percent composition of alloying elements in A516 grade 70 carbon steel (Fe balance).....	34
Table 3.1 Tafel slopes for PDP data recorded on CS and Cu in 0.1 M and 3 M Cl^-	50

List of Figures

Figure 1.1 Schematic of the DGR in sedimentary host rock. Image courtesy of NWMO (Toronto, Canada).....	2
Figure 1.2 Schematic diagram depicting the application of the Cu coating on the steel UFC by electrodeposition and cold spray. Image courtesy of Jason Giallonardo of NWMO (Toronto, Canada).....	3
Figure 1.1 Proposed chemical and electrochemical reactions in and around a through-coating defect when exposed to aerated Cl^- media. Image adapted from T. Standish et al. (2016).....	4
Figure 1.4 Structure of montmorillonite, the primary component of bentonite clay. Image obtained from O. Karnland (2010).....	6
Figure 1.5 Pourbaix diagram of the Fe- H_2O system at 25°C	8
Figure 1.6 Pourbaix diagram of the Fe- H_2O system at 25°C	10
Figure 1.7 Pourbaix diagram of the Cu- Cl^- - H_2O system at 25°C with a $[\text{Cl}^-]$ of 1.5 M, adapted from Beverskog et al. (1998).....	11
Figure 2.1 Butler-Volmer (solid) and Wagner-Traud (dashed) curves for a generic corrosion process.....	17
Figure 2.2 Galvanic series for various common materials in seawater (3.5% NaCl).....	18
Figure 2.3 Evans diagrams of the copper/carbon steel galvanic couple in two scenarios: a) polarization of the carbon steel is less significant, resulting in a non-negligible contribution to the anodic current from residual cathodic reactions on the carbon steel ($I_g < I_a$), and b) polarization of the carbon steel is more significant, thus residual cathodic activity on the carbon steel makes a negligible contribution to the anodic current ($I_g = I_a$).	20
Figure 2.4 Schematic of a Wagner-Traud curve, highlighting the range over which the potential is scanned.....	23
Figure 2.5 Schematic of a generic EIS experiment. It depicts the input sinusoidal potential perturbation and the electrochemical cell's output AC current response with phase shift.....	25
Figure 2.6 Simplified Randles circuit that might be used to model EIS data from a corroding system.....	25

Figure 2.7 a) Nyquist plot and b) Bode plots simulated from a simplified Randles circuit. Important features (R_s , R_{ct}) are noted on each plot.....	26
Figure 2.8 Diagram summarizing the possible transitions that can occur when using Raman spectroscopy.....	29
Figure 2.9 Raman spectrum (based on CCl_4) featuring both Stokes and anti-Stokes peaks, symmetrically placed about the Rayleigh peak.....	30
Figure 2.10 Schematic of electron beam interactions with a sample surface and sub-surface.....	31
Figure 2.11 Schematic diagram of an X-ray micro-CT instrument with X-ray source, detector, and sample.....	32
Figure 3.1 Schematic diagram of the three-compartment electrochemical cell used for galvanic coupling experiments.....	40
Figure 3.2 Plots of a) E_g in 3 M NaCl, b) i_g in 3 M NaCl, c) E_g in 0.1 M NaCl, and d) i_g in 0.1 M NaCl, plotted as functions of time at different Cu:CS area ratios, stated on the plot.....	42
Figure 3.3 Steady-state a) E_g , and b) i_g recorded in 0.1 M and 3 M NaCl, plotted as a function of Cu:CS area ratio. Steady-state E_{corr} of CS and Cu in 0.1 M and 3 M NaCl are plotted as horizontal dashed lines for reference.....	43
Figure 3.4 SEM images of corroded CS in 0.1 M NaCl at Cu:CS area ratios of a) 1:1, b) 10:1, c) 100:1, d) 500:1, e) 1000:1, and f) 1866:1.....	45
Figure 3.5 SEM micrograph of CS corroded at a Cu:CS area ratio of 1000:1 in 0.1 M NaCl. Green numbered boxes indicate areas where EDX spectra were taken.....	45
Figure 3.6 a) Electron image of CS corroded at a Cu:CS area ratio of 500:1 in 3 M NaCl and b-d) EDX maps of O, Fe, and Cu, respectively.....	46
Figure 3.7 Optical images of CS corroded at a Cu:CS area ratio of 1:1 in a) 3 M and b) 0.1 M NaCl.....	46
Figure 3.8 Raman spectra recorded on CS corroded at a 1:1 Cu:CS area ratio in 3 M NaCl.....	47
Figure 3.9 Optical images of CS corroded at a Cu:CS area ratio of 100:1 in a) 3 M and b) 0.1 M NaCl.....	47

Figure 3.10 Raman spectra recorded on CS after corrosion at a Cu:CS area ratio of 100:1 in 0.1 M NaCl.....	48
Figure 3.11 Optical image of CS corroded at a Cu:CS area ratio of 1865:1 in 0.1 M NaCl.....	48
Figure 3.12 Raman spectra recorded on CS after corrosion at a Cu:CS area ratio of 1865:1 in 0.1 M NaCl.....	48
Figure 3.13 PDP curves recorded on CS and Cu in solutions with [Cl ⁻] of a) 0.1 M or b) 3 M, where the current measured on the Cu curves was multiplied by the relative area of Cu for given Cu:CS area ratios.....	49
Figure 3.14 a) E_g and b) i_g , determined by PDP and by galvanic coupling experiments, plotted as a function of Cu:CS area ratio in solutions containing [Cl ⁻] of 0.1 M or 3 M.....	51
Figure 3.15 Steady-state a) E_g and b) i_g recorded at different Cu:CS area ratios under air-sparged and Ar-sparged conditions in 3 M NaCl.....	51
Figure 3.16 Coupled potential, E_g , recorded on CS corroded at different Cu:CS area ratios, plotted as a function of [Cl ⁻]. Conductivity of the bulk electrolyte, plotted in grey, is also included as a function of [Cl ⁻].....	52
Figure 3.17 Galvanic current, i_g , recorded on CS corroded at different Cu:CS area ratios, plotted as a function of [Cl ⁻]. Conductivity of the bulk electrolyte, plotted in grey, is also included as a function of [Cl ⁻].....	53
Figure 3.18 Electron images of CS corroded at Cu:CS area ratios of 10:1 (top), 100:1 (middle), and 1000:1 (bottom) in 0.001 M [Cl ⁻] (a, c, e) and 0.01 M [Cl ⁻] (b, d, f).....	54
Figure 3.19 Optical images of CS corroded at Cu:CS area ratios of a) 100:1 and b) 1000:1 in 0.001 M [Cl ⁻].....	55
Figure 3.20 Representative Raman spectra recorded on CS at various Cu:CS area ratios in [Cl ⁻] < 0.1 M.....	56
Figure 3.21 SEM micrograph of CS polarized without Cu, according to the E_g vs. time profile of a Cu:CS area ratio of 2500:1 in 3 M NaCl. Green numbered boxes indicate areas where EDX spectra were taken.....	58
Figure 4.1 Schematic diagram of experimental setup for galvanically coupled experiments in the presence of bentonite.....	66

Figure 4.2 a) E_g and b) i_g on CS plotted as a function of Cu:CS area ratio in 1 M NaCl solution with bentonite absent and with the electrodes occluded by a 5 mm bentonite slurry layer.....	68
Figure 4.3 a) E_g and b) i_g on steel plotted as a function of bentonite slurry layer thickness at Cu:CS area ratios of 10:1, 75:1 and 200:1. Horizontal dashed and dotted lines correspond to steady-state values collected under Ar-sparged conditions at the Cu:CS area ratios indicated by the colour.....	69
Figure 4.4 E_g and i_g plotted as a function of time for the Cu/CS galvanic couple at an area ratio of 10:1 in 1 M NaCl and varying amounts of bentonite clay.....	70
Figure 4.5 a-c) SEM images of CS corroded at a Cu:CS area ratio of 10:1 in 1 M NaCl solution without bentonite slurry, and d) SEM image with numbers 1 to 5 indicating notable locations where EDX spectra were collected.....	71
Figure 4.6 a) SEM image of CS corroded at a Cu:CS area ratio of 10:1 in 1 M NaCl without bentonite and area maps of the b) Fe, and c) Cu signals.....	72
Figure 4.7 Raman a) spectra and b) area map recorded on CS after corroding at a Cu:CS area ratio of 10:1 in 1 M NaCl without bentonite.....	73
Figure 4.8a-e) SEM images of CS corroded at a Cu:CS area ratio of 10:1 in 1 M NaCl under a 1 mm bentonite layer and f) EDX area map of S signals corresponding to electron image (e).....	74
Figure 4.9 Raman spectra recorded on CS after corroding at a Cu:CS area ratio of 10:1 in 1 M NaCl under a thin (1 mm) layer of bentonite.....	75
Figure 4.10 SEM images of CS corroded at a Cu:CS area ratio of 10:1 under a) a 20 mm, and b) a 5 mm bentonite layer with EDX area maps of the c) Al, d) Si, e) O, f) Fe, and g) S signals corresponding to electron image b.....	76
Figure 4.11 Raman a) spectra and b) area map recorded on CS after corroding at a Cu:CS area ratio of 10:1 in 1 M NaCl in the presence of a thick (>5 mm) bentonite layer.....	77
Figure 4.12 Equivalent circuits for a) CS in aerated 1 M NaCl in the absence of bentonite, b-c) CS in aerated 1 M NaCl in the presence of bentonite.....	78

Figure 4.13 a) Nyquist and b) Bode plots of EIS data recorded on Cu from E_g , as obtained from galvanic coupling experiments under the same conditions (1 M NaCl and bentonite layers of various thickness). The solid curves are simulations generated by equivalent circuits and correspond to the experimental points of like colour..... 79

Figure 4.14 Impedance contributions from R_s , R_p , and R_{bent} plotted as a function of bentonite layer thickness for CS samples at E_g in 1 M NaCl and various amounts of bentonite..... 80

Figure 4.15 Equivalent circuit for Cu in 1M NaCl in both the absence and presence of bentonite clay..... 81

Figure 4.16 a) Nyquist and b) Bode plots of EIS data recorded on Cu from E_g , as obtained from galvanic coupling experiments under the same conditions (1 M NaCl and bentonite layers of various thickness). The solid curves are simulations generated by equivalent circuits and correspond to the experimental points of like colour..... 81

Figure 4.17 a) Electron micrograph of Cu after corrosion in aerated 1 M NaCl without bentonite, and corresponding EDX maps of b) O and c) Fe..... 82

Figure 4.18 Impedance contributions from R_s and R_p plotted as a function of bentonite layer thickness for Cu samples at E_g 83

Figure 5.1 Illustration of electrochemical cell setup where the exposure conditions were aerated a) 1 M NaCl and b) 1 M NaCl with 50 g L⁻¹ bentonite clay..... 92

Figure 5.2 E_g and R_p values recorded on electrodeposited samples in 1 M NaCl or 1 M NaCl with 50 g L⁻¹ bentonite and plotted as a function of time..... 94

Figure 5.3 Vertical 2D cross sections through the centre of the drilled hole of an electrodeposited sample corroded in 1 M NaCl, obtained from 3D X-ray micro-CT data collected at indicated time points over the course of a corrosion experiment. The corroded volume below the Cu/CS interface was segmented and represented in turquoise. 97

Figure 5.4 Horizontal 2D cross sections through the Cu/CS interface of an electrodeposited sample, obtained from 3D X-ray micro-CT data collected after 24 hours, 7 days, and 14 days of the sample's exposure to 1 M NaCl..... 98

Figure 5.5 Vertical 2D cross sections through the centre of the drilled hole of an electrodeposited sample corroded in 1 M NaCl with 50 g L ⁻¹ bentonite, obtained from 3D X-ray micro-CT data collected at indicated time points over the course of a corrosion experiment. The corroded volume below the Cu/CS interface was segmented and represented in turquoise.....	99
Figure 5.6 Horizontal 2D cross sections through the Cu/CS interface of an electrodeposited sample, obtained from 3D X-ray micro-CT data collected after 24 hours, 7 days, and 14 days of the sample's exposure to 1 M NaCl and 50 g L ⁻¹ bentonite.	99
Figure 5.7 Corrosion volume (obtained through segmentation of X-ray micro-CT data) plotted as a function of time for electrodeposited samples corroded in the presence and absence of bentonite.....	100
Figure 5.8 E_g and R_p values recorded on cold-sprayed samples in 1 M NaCl or 1 M NaCl with 50 g L ⁻¹ bentonite and plotted as a function of time.....	101
Figure 5.9 Vertical 2D cross sections through the centre of the drilled hole of a cold-sprayed sample corroded in 1 M NaCl, obtained from 3D X-ray micro-CT data collected at indicated time points over the course of a corrosion experiment. The corroded volume below the Cu/CS interface was segmented and represented in pink.....	102
Figure 5.10 Horizontal 2D cross sections through the Cu/CS interface of a cold-sprayed sample, obtained from 3D X-ray micro-CT data collected after 24 hours, 7 days, and 14 days of the sample's exposure to 1 M NaCl.....	103
Figure 5.11 Vertical 2D cross sections through the centre of the drilled hole of a cold-sprayed sample corroded in 1 M NaCl with 50 g L ⁻¹ bentonite, obtained from 3D X-ray micro-CT data collected at indicated time points over the course of a corrosion experiment. The corroded volume below the Cu/CS interface was segmented and represented in pink.....	103
Figure 5.12 Horizontal 2D cross sections through the Cu/CS interface of a cold-sprayed sample, obtained from 3D X-ray micro-CT data collected after 24 hours, 7 days, and 14 days of the sample's exposure to 1 M NaCl and 50 g L ⁻¹ bentonite.....	104
Figure 5.13 Corrosion volume (obtained through segmentation of X-ray micro-CT data) plotted as a function of time for cold-sprayed samples corroded in the presence and absence of bentonite.....	105

Figure 5.14 a-b) Optical micrographs of an electrodeposited sample cross sectioned perpendicular to the Cu/CS interface after corrosion in aerated 1 M NaCl.....	105
Figure 5.15 a) SEM micrograph of an electrodeposited sample cross sectioned perpendicular to the Cu/CS interface, after corrosion in aerated 1 M NaCl and preservation of the corrosion film by injection of epoxy, with associated EDX maps for b) Cu, c) Fe, and d) O signals.....	106
Figure 5.16 a) Optical micrograph of an electrodeposited sample , cross sectioned perpendicular to the Cu/CS interface after corrosion in aerated 1 M NaCl and b) Raman spectra obtained at the points indicated on the optical image.....	107
Figure 5.17 a) Optical micrograph and b) SEM micrograph of an electrodeposited sample cross-sectioned perpendicular to the Cu/CS interface, after corrosion in aerated 1 M NaCl with 50 g L ⁻¹ bentonite, with associated EDX maps for c) Cu, d) Fe, and e) O signals....	107
Figure 5.18 a) Optical micrograph of an electrodeposited sample, cross-sectioned perpendicular to the Cu/CS interface after corrosion in aerated 1 M NaCl with 50 g L ⁻¹ bentonite, and b) Raman spectra acquired at the points indicated on the optical image....	108
Figure 5.19 Average corroded distance across the Cu/CS interface and average corroded depth from the Cu/CS interface to the bottom of the hole, obtained from X-ray micro-CT data on cold sprayed (CSp) and electrodeposited (ED) samples in both the presence and absence of bentonite, and plotted as a function of time.....	110
Figure 5.20 Corrosion rates of electrodeposited and cold-sprayed samples in 1 M NaCl, with and without bentonite.....	112

1. Introduction

1.1 Risks of Galvanic Corrosion in Corrosion-Resistant Metallic Coatings

The practice of using coatings to protect metallic substrates can be traced back hundreds of years [1], and today takes many forms. Some methods include the growth of passive oxide layers (anodization) [2], coating the substrate with a more active material to provide cathodic protection (galvanization), and coating the substrate with a more corrosion-resistant metal [3]. These coating methods effectively protect the underlying metal from corrosion by acting as a barrier to oxidizing species in the environment and/or material lost from the substrate, in addition to providing beneficial galvanic effects resulting from metal dissimilarity [4]. However, metallic coatings which are more corrosion-resistant, or noble, than the substrate have typically been used with trepidation because a defect in the coating would not only expose the substrate to a potentially corrosive environment, but the galvanic influence of the coating would actually accelerate corrosion of the substrate [5-6]. Nevertheless, some applications are served best by noble metal coatings, in jewelry and electronics for example, where inexpensive materials coated with noble metals can retain an outward brilliance or electrical conductivity [7] for much longer.

It is intuitive to assume that the size of a coating defect is an important factor in the degradation of the substrate metal. In the case of a noble metal coating, however, the fact that the most aggressive corrosion of the substrate metal occurs when the defects are minuscule [8] may not be immediately obvious. Corrosion processes are fundamentally electrochemical, where degradation of the metal is related to passage of current. Conservation of charge in a galvanic couple leads to the possibility that a small exposed area of substrate may have to sustain a large current resulting from reactivity on the comparatively vast coating. A large corrosion current density at that point would lead to rapid material loss and possible delamination of the coating. It therefore follows that there is a high standard for continuity and integrity of noble metal coatings, and thus they are often avoided due to the impracticality of ensuring that a coating is completely defect-free.

One modern, high-profile application of metallic coatings where the coating is more noble than the substrate is in metallic used fuel containers (UFCs) that have been proposed for the long-term disposal of Canada's used nuclear fuel in the deep geological repository (DGR), Figure 1.1. The UFC shell is to be made from a carbon steel (CS) pipe with hemispherical endcaps, providing

mechanical strength, and a 3 mm Cu coating over the entire outer surface. A compacted bentonite clay buffer box will house each UFC in the DGR emplacement rooms. The purpose of the Cu coating is to provide corrosion resistance, given that carbon steel alone is quite susceptible to corrosion. Intact, billion-year-old Lake Superior Cu deposits have provided a compelling natural analogue for the integrity of the Cu over the geological time scales of concern for fuel containment [9].

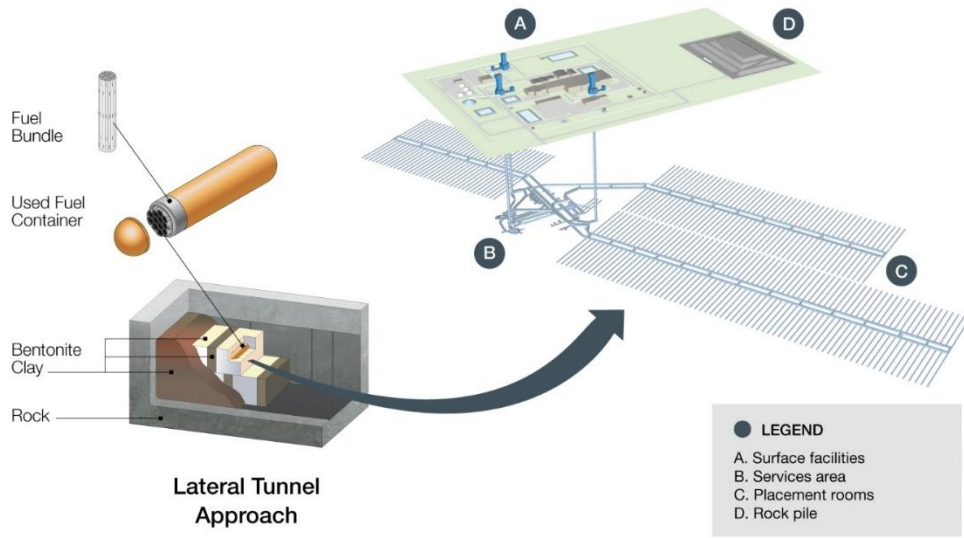


Figure 1.1 Schematic of the DGR in sedimentary host rock. Image courtesy of NWMO (Toronto, Canada) [11].

The Cu coating will be applied by electrodeposition to the lower assembly and the hemispherical end-caps and by cold-spray deposition over the weld region [10] where the UFC is to be sealed after loading of the fuel bundles, Figure 1.2. Upon application of the coatings, multiple rounds of non-destructive examination (NDE), in the form of ultrasonic and eddy current testing [11], will be used to screen for defects in the coating. The coating and inspection methods are being continually refined to ensure that the coatings will be as close to defect-free as possible and provide maximal protection. It is, however, possible that some containers placed in the DGR will have coating defects that were missed during NDE, or that developed during transit or emplacement, and that these defects may lead to premature failure of the container [12]. If a defect penetrates the full thickness of the coating and exposes carbon steel at the base of the defect, then galvanically accelerated corrosion of the steel is theoretically possible. The detection techniques proposed can easily identify surface defects <1 mm across [13], so any discontinuities in the coating that evade

detection would small enough to severely exacerbate the aggressiveness of the galvanic corrosion.

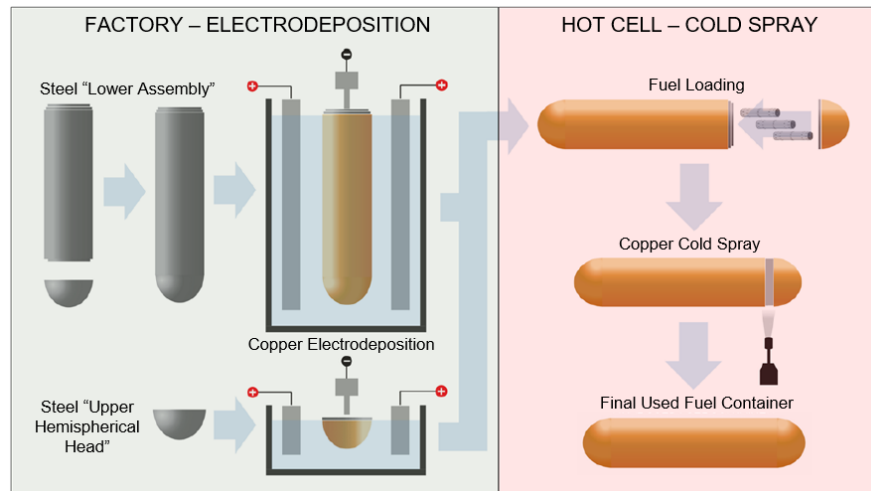


Figure 1.2 Schematic diagram depicting the application of the Cu coating on the steel UFC by electrodeposition and cold spray. Image courtesy of Jason Giallonardo of NWMO (Toronto, Canada).

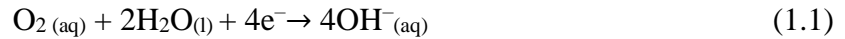
1.2 Evolution of Conditions in the DGR

The chemistry at the container surface in the DGR will dictate the corrosion behaviour of the Cu coating and any exposed substrate steel. Conditions in the DGR are expected to change drastically over time, and the near-field environment was described by King et al. in four chronological stages: i) immediate post-emplacment, ii) drying, iii) re-wetting and saturation of the bentonite clay buffer, and iv) long-term anoxic [14]. Aqueous corrosion is possible in stage one, when moisture at the container surface has not yet been driven away by rising temperature, and stage three and four, when moisture has returned to the container surface upon the temperature falling. Oxidizing conditions may prevail in stages one to three, due to the estimated 13 moles of O_2 per UFC which would be trapped in a full emplacement room upon closure [15], in addition to small concentrations of radiolytically produced oxidants [16]. In stage four, HS^- produced by microbes in the host rock could act as a long-term oxidant to drive corrosion of the container. Also, the bentonite porewater (which differs, in theory, from the host rock groundwater) will contain significant amounts of Cl^- , an anion which encourages both Cu and CS corrosion [14, 17-18]. Stages one and three represent periods of time when aqueous, oxic corrosion of the container could occur, though the duration of each stage is not precisely known because it depends on the nature of the host rock at the selected site for the DGR and the interactions of bentonite clay with the trapped O_2 . During stages one, three, and four, the criteria for galvanic corrosion at a through-coating defect could theoretically

be met; O₂ would initially be the main oxidant, possibly followed in the long-term by HS⁻, once O₂ is consumed.

1.3 Overview of Corrosion at a Through-Coating Defect

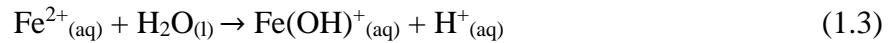
Previous studies of the through-coating defect scenario on Cu-coated steel have indicated the chemical and electrochemical reactions taking place at the substrate steel and the Cu coating [19] when exposed to 3 M NaCl under aerated conditions, Figure 1.3. The more noble Cu coating supports O₂ reduction via Reaction 1.1:



The O₂ reduction on the Cu is electrochemically coupled to oxidation of Fe in the steel substrate, following Reaction 1.2:



Upon dissolution, Fe²⁺ can then undergo hydrolysis, Reaction 1.3, or further oxidation by O₂, Reaction 1.4:



The ferric ion can then undergo hydrolysis by Reaction 1.5 and Reaction 1.6 in sequence [20]:

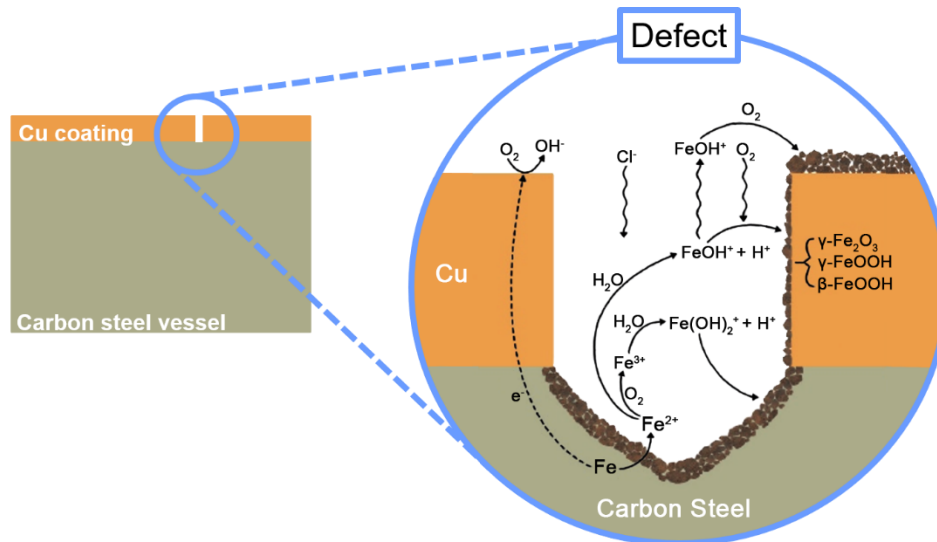
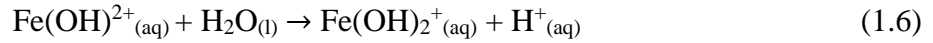
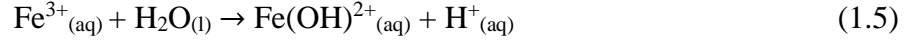


Figure 1.3 Proposed chemical and electrochemical reactions in and around a through-coating defect when exposed to aerated Cl⁻ media. Image adapted from T. Standish et al. (2016) [19].



The hydrated ferrous and ferric species would serve as precursors for a variety of solid Fe oxides and hydroxides which can then be deposited inside and around the defect. The hydrolysis of the aqueous Fe^{2+} and Fe^{3+} produces aqueous H^{+} , decreasing the pH within the defect, while the $\text{OH}^{-}_{(\text{aq})}$ produced at the Cu surface would increase the pH outside the defect. The buildup of cations within the defect causes $\text{Cl}^{-}_{(\text{aq})}$ to migrate into the defect to neutralize the charge. The decrease in pH and increased salinity inside the defect could also create more aggressive conditions for corrosion of the steel substrate.

1.4 Functions and Properties of the Bentonite Clay

The bentonite clay buffer is a vital component of the DGR system, serving as a barrier to the transport of corrosive species toward, and radionuclides and/or corrosion products away from, the UFC, while also decreasing bacterial activity near the container [21]. The naturally occurring bentonite clay proposed for use in the DGR contains approximately 87% montmorillonite, and smaller amounts of calcite, quartz, muscovite, and other minerals [22]. Montmorillonite, Figure 1.4, has a 2:1 layered structure, in which a sheet of octahedrally coordinated Al is bound above and below by O bridges to sheets of tetrahedrally coordinated Si [21]. The chemical formula for such clays is $(\text{Ca}, \text{Na}, \text{H})(\text{Al}, \text{Mg}, \text{Fe}, \text{Zn})_2(\text{Si}, \text{Al})_4\text{O}_{10}(\text{OH})_2 \cdot x\text{H}_2\text{O}$, where Al^{3+} in the octahedral sheet can be substituted for Mg^{2+} , Fe^{2+} , Fe^{3+} , or Zn^{2+} cations and Si^{4+} in the tetrahedral sheet can be substituted for Al^{3+} cations [23]. The isomorphous substitution for cations of a lower oxidation state causes the montmorillonite sheets to take on a slight negative charge, which leads to the retention of hydrated cations in the interlayer space to balance the charge. Because the layer charge is typically not large (at most 1.2 unit charges per $\text{O}_{20}(\text{OH})_4$ layer unit [21]), the montmorillonite readily absorbs water into the interlayer space where it interacts with the interlayer cations and forms hydrogen bonds with the sheets themselves [24-25]. The repulsive forces associated with uptake of water into the interlayer space causes an increase in d-spacing between the layers and expansion of the clay. The sorption and swelling properties of the compacted bentonite make ingress of groundwater towards the UFC extremely slow, as well as allow for some degree of resealing after the initial desiccation of the buffer box at high temperatures and resulting shrinkage and cracking. Due to very low hydraulic conductivity, the transport of oxidizing species towards

the container surface is governed by diffusion as opposed to convection in free groundwater [26].

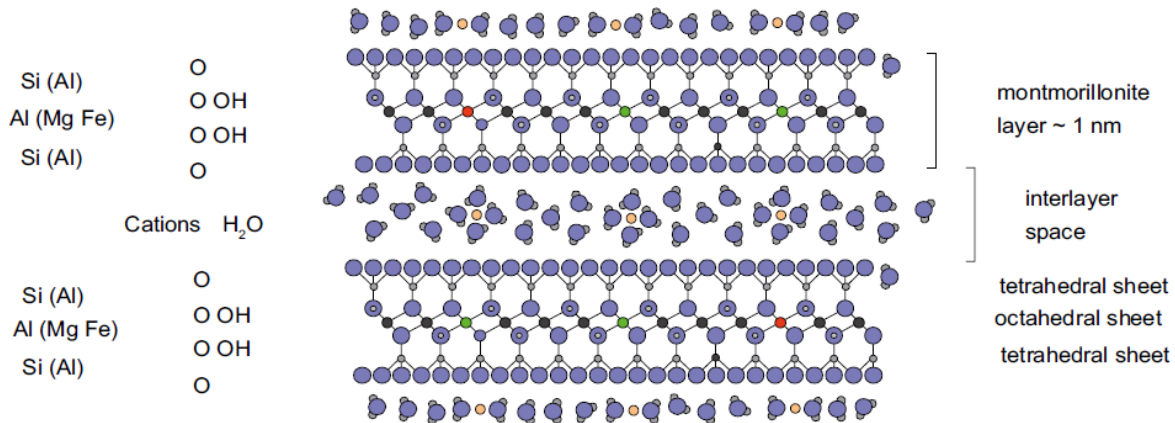


Figure 1.4 Structure of montmorillonite, the primary component of bentonite clay. Image obtained from O. Karnland (2010) [21].

The bentonite clay is often characterized by its primary interlayer cation; two common types being Na-based and Ca-based bentonite. The dominant cation has a profound effect on the swelling properties of the bentonite, particularly due to differences in ionic radius and hydration enthalpy, where Ca^{2+} becomes fully hydrated at a much lower level of interlayer water uptake [24]. Upon exposure to saline groundwater or with the dissolution of some minor mineral components of the clay, the original cations can be exchanged with external soluble cations. The cation inventory of the bentonite is expected to change over time as the clay interacts with groundwater, and similarly, the solution contained in the bentonite pores may have a very different composition than the groundwater which entered the clay. Soluble cations released as a result of corrosion of the Cu coating (or in the case of a defect, the carbon steel), such as H^+ , Cu^{2+} , and Fe^{2+} , can be sorbed into the clay near the container surface [27-28]. Bentonite clay can also effectively act as an adsorbent for cationic radionuclides such as $^{137}\text{Cs}^+$ and $^{90}\text{Sr}^{2+}$, though not for anionic radionuclides such as $^{129}\text{I}^-$ and $^{99}\text{Tc}^-$ [29-30], though the compacted clay would still be a transport barrier for cations and anions both.

1.5 Carbon Steel Corrosion and Carbon Steel as the Anode

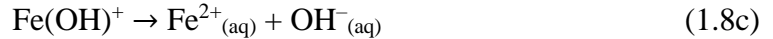
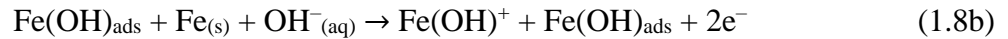
The UFC is to be manufactured from A516 gr. 70 carbon steel. Carbon steels are alloys of primarily Fe and C and are classified based on the C content: low-carbon (or mild) steels contain less than 0.25% C, medium-carbon steels contain between 0.25% and 0.60% C, and high-carbon steels contain 0.61% to 1.25% C by weight [31]. Carbon steels also tend to contain small amounts of

other elements such as Mn, Si, and Cu. Carbon steels are used extensively because of they are inexpensive, tough, and workable, though they tend to be brittle at higher C contents [31].

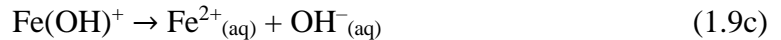
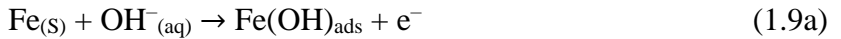
Unfortunately, carbon steels also possess poor corrosion resistance when exposed to the porewater chemistry anticipated in the DGR. The corrosion of carbon steel occurs by the oxidation of the Fe matrix by Reaction 1.7 (equivalent to Reaction 1.2 from section 1.3):



The dissolution of Fe as Fe^{2+} proceeds through the formation of $\text{Fe}(\text{OH})_{\text{ads}}$ intermediates, as shown in both the Heusler mechanism (Reactions 8a-c) [32]:



and the Bockris mechanism (Reactions 9a-c) [32]:



which preferentially apply depending on the roughness and defect density of the surface from which Fe is dissolving; a more imperfect surface will tend to favour the Heusler mechanism [32]. The susceptibility of carbon steel to corrosion can be inferred from the *Pourbaix diagram* for the Fe-H₂O system, Figure 1.5, which represents the most stable phases of Fe as a function of pH and potential [33-34]. Water is stable inside the diagonal dashed lines; above the upper dashed line, H₂O can be oxidized to O₂, and below the lower dashed line, H₂O can be reduced to H₂. At all pH values displayed in Figure 1.5, metallic Fe is stable only at potentials more negative than the potential of H₂O reduction, and thus is not stable in aqueous solutions [33]. The corrosion potential, E_{corr} , which takes a value between the equilibrium potential of the oxidation reaction and the equilibrium potential of the reduction reaction, will lie somewhere above the stability boundary of metallic Fe (oxidation) and below the stability boundary of H₂ (reduction). The pH of the solution

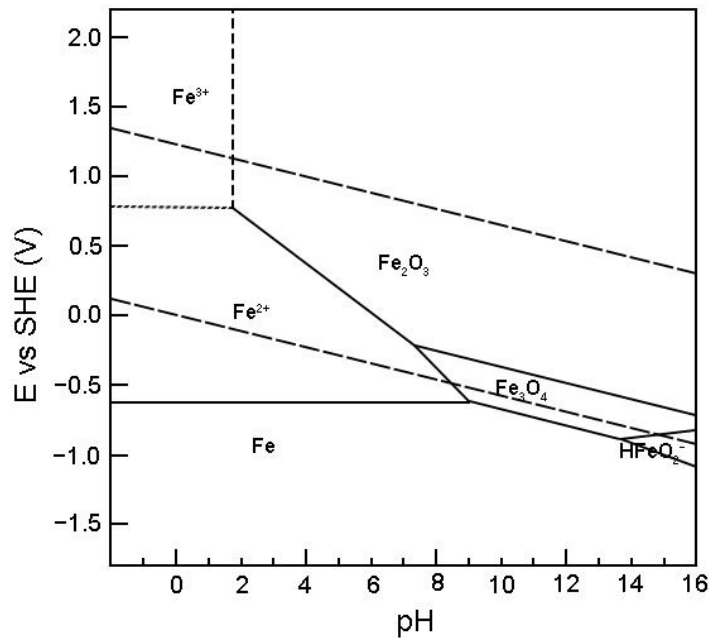
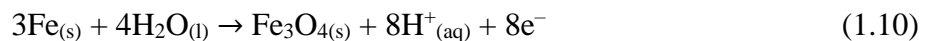


Figure 1.5 Pourbaix diagram of the Fe-H₂O system at 25° C [34].

determines the most stable oxidation product of Fe, where in acidic to near-neutral conditions the Fe can undergo active dissolution by forming aqueous Fe²⁺, and in moderately alkaline conditions the Fe converts to the more stable Fe₃O_{4(s)} by Reaction 1.10 [33]. Surface coverage of Fe₃O₄, magnetite, is known to provide some passive corrosion protection [35].

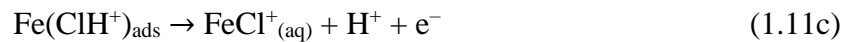
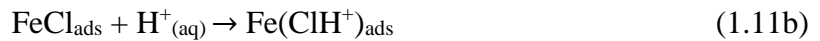


At pH > 13, it is possible for the steel to undergo active dissolution by the formation of HFeO₂⁻. Thus, though some conditions favour the formation of passive Fe oxide films, the thermodynamic instability of Fe in water makes carbon steel extremely vulnerable to aqueous corrosion, particularly in the presence of species which can complex Fe ions and/or compromise the integrity of the film.

When dissolved O₂ is present in solution, it is thermodynamically unstable at all potentials below the upper water stability boundary. The E_{corr} of steel in a solution containing dissolved O₂ will then rest at some point above the boundary for Fe oxidation from Fe metal, and below the boundary of O_{2(aq)} reduction (which is dependent on the prevailing O₂ concentration), and thus can be more positive than the E_{corr} of Fe in anoxic water. In the presence of dissolved O₂, it is possible to oxidize Fe²⁺_(aq) to Fe³⁺_(aq) as well as form aqueous Fe^{III} hydroxides of the form: Fe(OH)_x^{(3-x)+}. Fe^{III} oxides

and hydroxides are highly insoluble, with reported K_{sp} values of $\sim 10^{-40}$ for the most commonly observed varieties [36]. These ferric (oxyhydr)oxide species can form either through oxidation of magnetite (Fe_3O_4) to form maghemite ($\gamma-Fe_2O_3$) and, under hydrothermal conditions, hematite ($\alpha-Fe_2O_3$), or by precipitation and subsequent conversion of $Fe(OH)_x^{(z-x)+}$ ($z = 2$ or 3) species and intermediates, forming lepidocrocite ($\gamma-FeOOH$), goethite ($\alpha-FeOOH$), and akaganéite ($\beta-FeO(OH,Cl)$) [37]. Maghemite can contribute to the passive oxide layer formed on carbon steel surfaces at more positive potentials, endowing some corrosion protection, while $FeOOH$ species tend to form non-protective upper layers [35].

The presence of anions such as Cl^- can affect the corrosion of carbon steel, including by limiting O_2 solubility, changing solution conductivity, complexation to ferrous and ferric ions, and surface adsorption [17]. The effect of the Cl^- ion is typically kinetic as opposed to thermodynamic. The Cl^- ion influences carbon steel corrosion through its direct participation in corrosion reactions, such as through the competitive formation of $Fe-Cl$ complexes as the first step in Fe dissolution [17]. $FeCl_{ads}$ is unstable at neutral to alkaline pH and can be easily converted to $FeOH_{ads}$. However, at high Cl^- concentrations and low pH, the $FeCl_{ads}$ species is stable enough to proceed through the following sequence [32], Reactions 1.11a-c:



The Cl^- ion can also affect the formation pathways of corrosion products and the integrity of the oxide film. Low Cl^- concentrations favour formation of goethite and Fe_2O_3 and also favour more uniform corrosion. High Cl^- concentrations tend to favour the formation of lepidocrocite and akaganéite, in addition to causing localized corrosion via disruption of the oxide film [17, 38]. The Cl^- ion is considered an aggressive anion which increases the tendency of steel to corrode, and its predicted abundance in the bentonite porewater at the UFC surface makes vital the understanding of how Cl^- interacts with the UFC materials.

1.6 Copper Corrosion and Copper as the Cathode

The selection of Cu for the coating of the carbon steel UFC was due in part to the thermodynamic stability of metallic Cu in anoxic water, making it very resistant to corrosion under the conditions

expected in the DGR [39]. Under such conditions, Cu behaves essentially like a noble metal, while being far less expensive than noble metals like Ag and Pt. Due to its relative nobility compared to carbon steel, Cu acts as the preferential cathode in the Cu/CS galvanic couple which may arise in the case of a through-coating defect.

As demonstrated by the Pourbaix diagram for the Cu-H₂O system [34], Figure 1.6, metallic Cu is stable below the boundary for H₂ evolution, and thus will not corrode in anoxic pure water. In the presence of O₂, corrosion of the Cu can be driven by O₂ reduction and can take the form of active dissolution through Cu²⁺_(aq), as well as formation of protective species such as Cu₂O_(s) and Cu(OH)_{2(s)}. In the presence of Cl⁻_(aq), as shown in Figure 1.7 [40], Cu remains stable in anoxic water in pH > 3, though at very low pH, corrosion could be driven by H⁺_(aq) reduction. In the presence of dissolved O₂, the dissolution of Cu is readily facilitated by Cl⁻ through the formation of CuCl_x^{(x-1)-}_(aq) species.

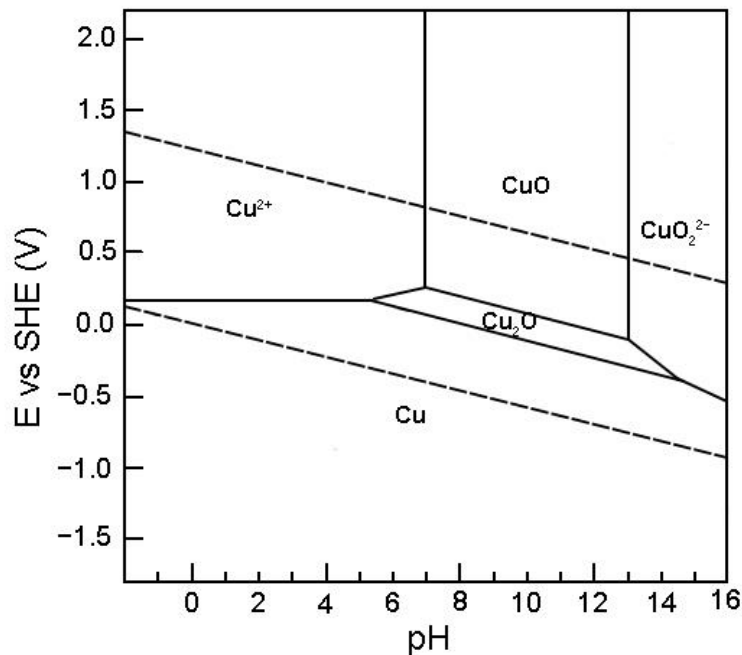


Figure 1.6 Pourbaix diagram of the Fe-H₂O system at 25° C [34].

In the Cu/CS galvanic couple, Cu, as the more noble metal, will be preferentially supporting reduction reactions and corroding more slowly than when in isolation. The possible reduction reactions occurring on the Cu are dependent on the shared potential of the couple. In aerated solution, O₂ reduction is a significant contributor to the cathodic activity on the Cu. The rate of O₂ reduction becomes limited by the rate of diffusion of O₂ to the Cu surface, a phenomenon known

as *mass-transport control*. The Cu oxidation reaction will also depend on the shared potential of the couple. At potentials more negative than the stability boundary for metallic Cu, the Cu should not corrode.

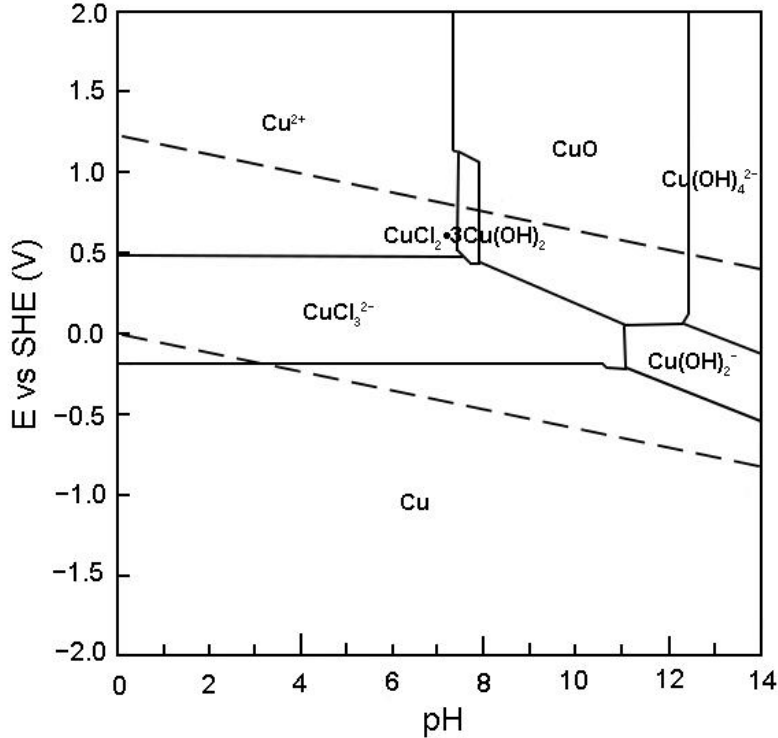


Figure 1.7 Pourbaix diagram of the Cu-Cl-H₂O system at 25° C with a [Cl⁻] of 1.5 M, adapted from Beverskog et al. (1998) [40].

1.7 Gaps in Research and Research Goals

This work seeks to fill several gaps in the body of work studying galvanic corrosion in defective metallic coatings. Galvanic corrosion has been extensively studied in a variety of metal couples under many different conditions. The Cu/steel galvanic couple has been studied mostly in the context of the UFC used in the Canadian repository [19, 41-42] and the Swedish repository [43], both of which feature Cu and steel in their design. There is, however, no work in this context which has carefully studied the Cu-to-steel area ratio considerations in a defective coating, and particularly how that affects the magnitude of the current passing between the Cu and steel. Some other work has been done on Cu/steel or brass/steel galvanic corrosion under stagnant [44] or various flow conditions [45-46]. Other studies used Cu-Ni alloys coupled to mild steel to study effects of cathode-to-anode area ratios, though only up to a ratio of 600:1 [47]. Studies of corrosion of Cu/steel couples in the presence of bentonite are rarer still, though some computational

modelling on that system has been done by Stoulil et al. [48] for Czech nuclear waste disposal.

This work uses corrosion test methods, electrochemical methods, advanced imaging techniques, and surface analysis to determine how the Cu/CS system behaves under DGR-relevant conditions, focusing on the following:

- The corrosion behaviour and galvanic corrosion rate of the Cu/CS couple over a wide range of Cu-to-CS area ratios, achieved through a unique experimental setup ensuring radial symmetry.
- The effects of Cl^- concentration and O_2 availability on corrosion of the Cu/CS galvanic couple, and how those effects may be intertwined.
- The corrosion behaviour of the Cu/CS couple across a wide range of Cu-to-CS area ratios when the electrode surfaces are obstructed by bentonite clay, as well as the effect of the thickness of that obstruction.
- The corrosion behaviour at the Cu/CS interface in a simulated coating defect. Over several weeks, X-ray imaging was used to monitor the progression of corrosion within the defect, noting the morphology and preferred direction of corrosion.

1.8 References

1. History of galvanizing. <https://www.galvanizing.org.uk/hot-dip-galvanizing/history-of-galvanizing/> (accessed May 13, 2020).
2. H. Ackerman, et al., *Corrosion*. ASM International: USA, 1992; Vol. 13.
3. *Surface Engineering for Corrosion and Wear Resistance*. ASM International: Novelty, USA, 2001.
4. How Metallic Coatings Protect Steel. https://www.astm.org/SNEWS/APRIL_2006/dallynside_apr06.html (accessed May 13, 2020).
5. R. G. Kelly, J. R. Scully, D. W. Shoesmith, R. Buchheit, *Electrochemical Techniques in Corrosion Science and Engineering*. Marcel Dekker, Inc.: New York, USA, 2003.
6. J. Yahalom, Corrosion Protection Methods: 4.2 Metallic Coatings. In *Encyclopedia of Materials: Science and Technology*, Elsevier: 2001; pp 1710-1713.
7. W. Giurlani, P. Marcantelli, F. Benelli, D. Bottacci, F. Gambinossi, M. Passaponti, A. De Luca, E. Salvietti, et al., *Coatings* **2019**, *9*, 405-415.
8. K. B. Oldham, F. Mansfeld, *J. of Appl. Electrochem.* **1972**, *2*.
9. D. Moser, J. Noël, A. Dobkowska, D. Zagidulin, J. Perritt, P. Keech, M. Behazin, J. Binns, et al. In *Learning from 1 billion year old copper*, EGU General Assembly, Online, Online, 2020.
10. *Postclosure Safety Assessment of a Used Fuel Repository in Crystalline Rock*; TR-2017-02; NWMO: Toronto, Canada, 2017.
11. J. Chen, M. Behazin, J. Binns, K. Birch, A. Blyth, S. Briggs, J. Freire-Canosa, G. Cheema, et al. *Technical Program for Long-Term Management of Canada's Used Nuclear Fuel – Annual Report 2018*; TR-2019-01; NWMO: Toronto, Canada, 2019.
12. F. Garisto *Seventh Case Study: Features, Events and Processes*; TR-2018-05; NWMO: Toronto, Canada, 2018.
13. T. Liyanage, J.-F. Martel, O. Marcotte, D. Doyle In *Non-destructive examination (NDE) development for the inspection of copper coatings on used fuel containers*, CNS: Canadian conference on nuclear waste management, decommissioning and environmental restoration, Ottawa, Canada, Ottawa, Canada, 2016.
14. F. King, D. S. Hall, P.G. Keech, *Corros. Eng. Sci. Techn.* **2017**, *52*, 25-30.
15. D. S. Hall, T. Standish, M. Behazin, P. G. Keech, *Corros. Eng. Sci. Techn.* **2018**, 1-7.
16. M. E. Dzaugis, A. J. Spivack, S. D'Hondt, *Radiat. Phys. Chem.* **2015**, *115*, 127-134.

17. R. T. Foley, *Corrosion* **1970**, *6*, 58-70.
18. G. Kear, B. D. Barker, F. C. Walsh, *Corros. Sci.* **2004**, *46*, 109-135.
19. T. Standish, J. Chen, R. Jacklin, P. Jakupi, S. Ramamurthy, D. Zagidulin, P. Keech, D. Shoesmith, *Electrochim. Acta* **2016**, *211*, 12.
20. R. L. Martin, P. Jeffrey Hay, L. R. Pratt, *J. Phys. Chem. A* **1998**, *102*, 3565-3573.
21. O. Karnland *Chemical and mineralogical characterization of the bentonite buffer for the acceptance control procedure in a KBS-3 repository*; TR-10-60; SKB: Stockholm, Sweden, 2010.
22. D. Dixon, A. Man, S. Rimal, J. Stone, G. Siemens *Bentonite Seal Properties in Saline Water*; TR-2018-20; NWMO: Toronto, Canada, 2018.
23. F. Uddin, *Metall. Mater. Trans. A* **2008**, *39A*, 2804-2814.
24. S. L. Teich-McGoldrick, J. A. Greathouse, C. F. Jové-Colón, R. T. Cygan, *J. Phys. Chem. C* **2015**, *119*, 20880–20891.
25. S. Karaborni, B. Smit, W. Heidug, J. Urai, E. van Oort, *Science* **1996**, *271*, 1102-1104.
26. S. Briggs, J. McKelvie, B. Sleep, M. Krol, *Sci. Total Environ.* **2017**, *599-600*, 348-354.
27. S. Ding, Y. Sun, C. Yang, B. Xu, *Mining Science and Technology* **2009**, *19*, 489-492.
28. A. Muurinen, C. Tournassat, J. Hadi, J. Greneche *Sorption and diffusion of Fe(II) in bentonite*; Working Report 2014-04; Posiva: Eurajoki, Finland, 2014.
29. D. W. Oscarson, H. B. Hume, F. King, *Clays Clay Miner.* **1994**, *42*, 731-736.
30. J. Bors, S. Dultz, B. Riebe, *Appl. Clay Sci.* **2000**, *16*, 1-13.
31. Carbon Steel: Properties, Production, Examples and Applications.
<https://matmatch.com/learn/material/carbon-steel> (accessed May 28, 2020).
32. T. Tsuru, *Mater. Sci. Eng.* **1991**, *A146*, 1-14.
33. M. Pourbaix, *Atlas of Electrochemical Equilibria in Aqueous Solutions*. NACE International, Celebcor: Houston USA; Brussels, Belgium, 1974.
34. E. McCafferty, *Introduction to Corrosion Science*. Springer: New York, USA, 2010.
35. L. Freire, X.R. Nóvoa, M.F. Montemor, M.J. Carmezim, *Mater. Chem. Phys.* **2009**, *114*, 962-972.
36. A. Stefánsson, *Environ. Sci. Technol.* **2007**, *41*, 6117-6123.

37. R. M. Cornell, U. Schwertmann, *The Iron Oxides: Structure, Properties, Reactions, Occurrences and Uses*. 2nd ed.; WILEY-VCH Verlag GmbH & Co. KGaA: Weinheim, Germany, 2003.
38. Y. Song, G. Jiang, Y. Chen, P. Zhao, Y. Tian, *Sci. Rep.* **2017**, *7*, 1-13.
39. J. R. Scully, D. Feron, H. Hanninen *Review of the NWMO Copper Corrosion Program*; NWMO-TR-2016-11; Nuclear Waste Management Organization: Toronto, Canada, August 2016, 2016; p 31.
40. B. Beverskog, I. Puigdomenech *Pourbaix diagrams for the system copper-chlorine at 5-100 °C*; 98:19; Swedish Nuclear Power Inspectorate (SKI): 1998.
41. T. Standish, D. Zagidulin, S. Ramamurthy, P. Keech, D. Shoesmith, J. Noël, *Geosciences* **2018**, *8*, 1-14.
42. T. E. Standish, D. Zagidulin, S. Ramamurthy, P. G. Keech, J. J. Noël, D. W. Shoesmith, *Corros. Eng. Sci. Techn.* **2017**, *52*, 65-69.
43. A. P. Rance N. R. Smart, P. A. H. Fennell *Galvanic corrosion of copper-cast iron couples*; TR-05-06; SKB: Stockholm, Sweden, January 2005, 2005; p 78.
44. B. Tsujino, S. Miyase, *Corrosion* **1982**, *38*.
45. J. M. Ali, Q. M. Abbas, *Al-Khwarizmi Engineering Journal* **2009**, *5*, 60-71.
46. B. O. Hasan, *J. Petrol Sci. Eng.* **2014**, *124*, 137-145.
47. Z. Wang, Y. Wang, C. Wang, *IOP Conf. Ser.: Mater. Sci. Eng.* **2018**, *322*.
48. J. Stoulil, M. Kouřil, L. Pavlova, D. Dobrev, J. Gondolli, *Mater. Corros.* **2018**, *1-7*.

2. Methods and Materials

2.1 Fundamentals of Galvanic Corrosion

Corrosion is fundamentally an electrochemical process, and galvanic corrosion is one of several common types of corrosion processes. In its simplest form, corrosion is the degradation of a metal (or conductive material) due to oxidation and subsequent dissolution as a result of exposure to an electrolyte containing oxidizing species. The reduction of the oxidant at a cathodic site is coupled to the oxidation of the metal elsewhere on the surface, at an anodic site [1]. Electron current flows between the sites through the conductive matrix of the metal and balanced by movement of charge carriers in solution. The cathodic and anodic half-reactions each have a unique equilibrium (reversible) potential, E_{eq} , given by the Nernst equation, Equation 2.1:

$$E_{eq} = E^0 - \frac{RT}{nF} \ln K \quad (2.1)$$

where E^0 is the standard potential in V, K the equilibrium constant, R is the universal gas constant with a value of $8.314 \text{ C V mol}^{-1} \text{ K}^{-1}$, T is the temperature in K, n is the number of electrons transferred, and F is the Faraday constant with a value of $96\,485 \text{ C mol}^{-1}$. The potential is a thermodynamic property, and is related to the Gibb's free energy by Equation 2.2:

$$\Delta G = -nFE \quad (2.2)$$

where ΔG is the Gibb's free energy change in J.

In redox couple where the two half-reactions have different equilibrium potentials, the resulting electrochemical reaction will produce a net current because one half-reaction will favour reduction and the other will favour oxidation. Therefore, under these circumstances, neither half-reaction can be at equilibrium. The rate of electron transfer, or *current*, is proportional to the rate of reaction [2], and therefore is the source of kinetic information. The current-potential relationship for each half reaction can be described by the Butler-Volmer equation [2], Equation 2.3:

$$I = I_0 \left[e^{-\alpha \frac{F}{RT} (E - E_{eq})} - e^{[1-\alpha] \frac{F}{RT} (E - E_{eq})} \right] \quad (2.3)$$

in which I is the current in A, I_0 is the exchange current in A, α is the symmetry coefficient, and E is the potential in V. Oxidation half-reactions supply the anodic current, while the reduction half-

reactions supply the cathodic current, which in this work will be considered positive and negative, respectively. In a corroding system, conservation of charge requires the sum of anodic currents and sum of cathodic currents to be equal in magnitude. The point at which the sum of the anodic currents and the cathodic currents is zero, given by their Butler-Volmer curves (Equation 2.3), corresponds to the corrosion potential, E_{corr} , as shown in Figure 2.1. The electrochemical kinetics of corrosion, a mixed potential process, can be described by the superposition of the kinetics of the anodic and cathodic half-reactions via the Wagner-Traud equation, Equation 2.4, which relates the total current to the deviation of the potential of the system from the E_{corr} of the system [3]:

$$I_{\text{net}} = I_{\text{corr}} \left[e^{\frac{2.3(E-E_{\text{corr}})}{\beta_A}} - e^{\frac{-2.3(E-E_{\text{corr}})}{\beta_C}} \right] \quad (2.4)$$

where I_{net} is the total current in A, I_{corr} is the corrosion current in A, and β_A and β_C are the Tafel slopes (the slope of the E vs. $\log I$ curves) for the anodic and cathodic reactions, respectively, in V dec^{-1} of current. At E_{corr} , the exponential terms in Equation 2.4 each evaluate to unity so the right-hand side evaluates to zero, resulting in zero net current. When a potential is applied, i.e. when E is forced to deviate from E_{corr} by use of a potentiostat, for example, the net current deviates from zero; polarization in the positive direction results in net positive current and polarization in the negative direction results in net negative current.

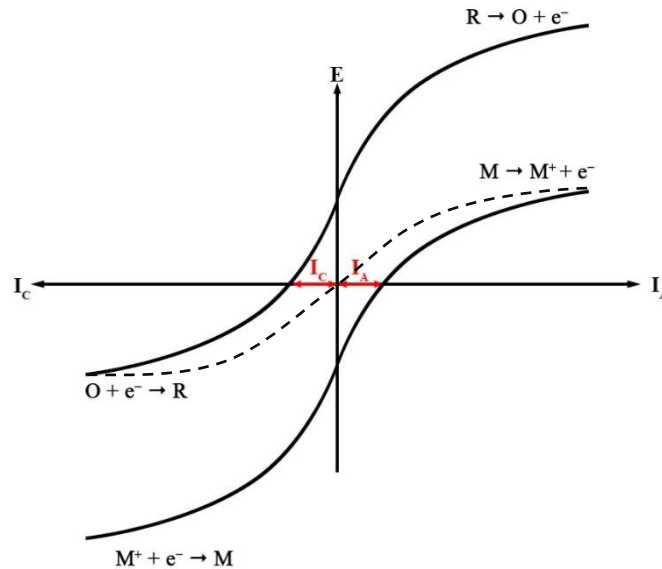


Figure 2.1 Butler-Volmer (solid) and Wagner-Traud (dashed) curves for a generic corrosion process.

Metals will adopt different E_{corr} values in different environments, depending on which oxidants are available to drive corrosion, as well as the composition of the electrolyte and temperature. Galvanic corrosion occurs when two dissimilar metals are electrically connected and are both exposed to the same corrosive medium. Just as total charge is conserved in the case of a single corroding metal, total charge in a galvanic couple is conserved, and just as the potential difference between two half-reactions results in the flow of current (I_{corr}) on a single metal, the potential difference between the two metals in a galvanic couple drives the flow of current from one metal to the other. Therefore, despite a net zero current on the galvanic couple as a whole, each individual metal acts either as a net anode or a net cathode.

The comparison of E_{corr} values for different materials in the same environment, as in an experimentally determined galvanic series (Figure 2.2) [4], gives some indication of which materials are more noble (resistant to oxidation) and which are more active (easily oxidized) in

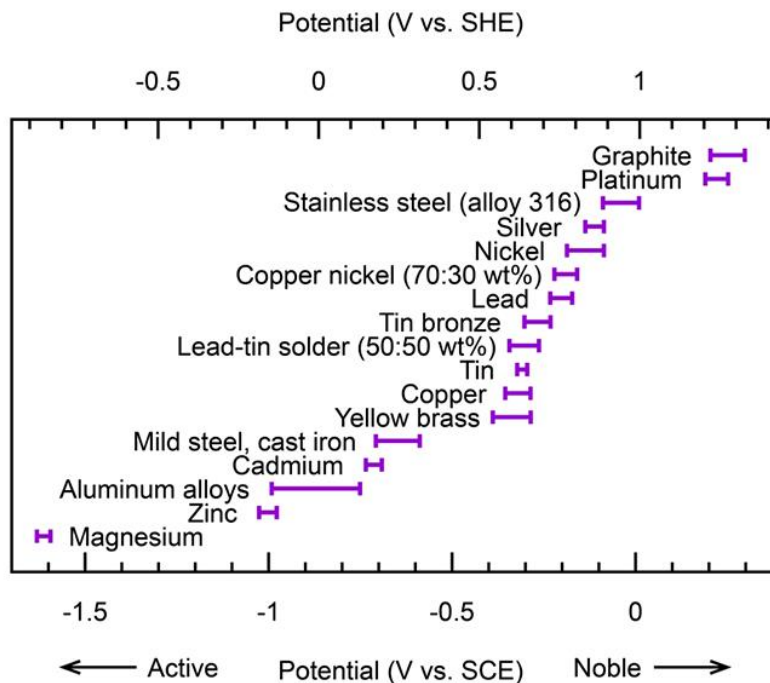


Figure 2.2 Galvanic series for various common materials in seawater (3.5% NaCl) [4].

that environment, and therefore the expected direction of current flow between the metals, though the potential difference (if there is one), is not a reliable predictor of rate [1]. The galvanic current, I_g , which flows from the net anode to the net cathode, is described in equation 2.5 using a variation of the Wagner-Traud equation for each metal [5], with a CS/Cu galvanic couple as an example:

$$I_g = I_{\text{corr}}^{\text{CS}} \left[e^{\frac{2.3(E_g - E_{\text{corr}}^{\text{CS}})}{\beta_A^{\text{CS}}}} - e^{\frac{-2.3(E_g - E_{\text{corr}}^{\text{CS}})}{\beta_C^{\text{CS}}}} \right] = -I_{\text{corr}}^{\text{Cu}} \left[e^{\frac{2.3(E_g - E_{\text{corr}}^{\text{Cu}})}{\beta_A^{\text{Cu}}}} - e^{\frac{-2.3(E_g - E_{\text{corr}}^{\text{Cu}})}{\beta_C^{\text{Cu}}}} \right] \quad (2.5)$$

given that E_g is the coupled potential in V, shared across both metals of the galvanic couple, and I_{corr} and E_{corr} refer to the corrosion current in A and corrosion potential in V, respectively, of either the noble metal (Cu) or the active metal (CS). On an E vs. $\log I$ plot, or *Evans diagram* (Figure 2.3), I_g can be found at the intersection of the cathodic branch of the more noble metal and the anodic branch of the more active metal. The coupled potential, E_g , always resides in between the E_{corr} values of the two metals. The more active metal is thus polarized in the positive direction, often resulting in accelerated corrosion, while the more noble metal is polarized in the negative direction, often resulting in cathodic protection. It is important to note that I_g does not account for residual anodic activity on the more noble metal and residual cathodic activity on the more active metal, which may contribute a significant current depending on the magnitude of the anodic and cathodic polarizations. For example, when considering the total anodic current (I_a^{CS}) on CS in the Cu/CS galvanic couple, the following relationship can be used (Equation 2.6):

$$I_a^{\text{CS}} = I_g + I_{\text{corr}}^{\text{CS}} \left[e^{\frac{-2.3(E_g - E_{\text{corr}}^{\text{CS}})}{\beta_C^{\text{CS}}}} \right] \quad (2.6)$$

If E_g is very close to E_{corr} of CS, then the exponential term will evaluate to close to unity, and the anodic current can be estimated by Equation 2.7 and visualized by Figure 2.3a:

$$I_a^{\text{CS}} \approx I_g + I_{\text{corr}}^{\text{CS}} \quad (2.7)$$

If E_g is very distant from E_{corr} of CS, then the exponential term will decay to near zero, resulting in Equation 2.8 and Figure 2.3b:

$$I_a^{\text{CS}} \approx I_g \quad (2.8)$$

Residual cathodic activity on the more active metal is accounted for in I_{corr} , which cannot be measured directly. Any measured I_g would underestimate the total anodic current on the active metal and by extension, the corrosion rate, though the degree to which it is underestimated depends on the extent of polarization from E_{corr} . When the active metal is subjected to a large polarization

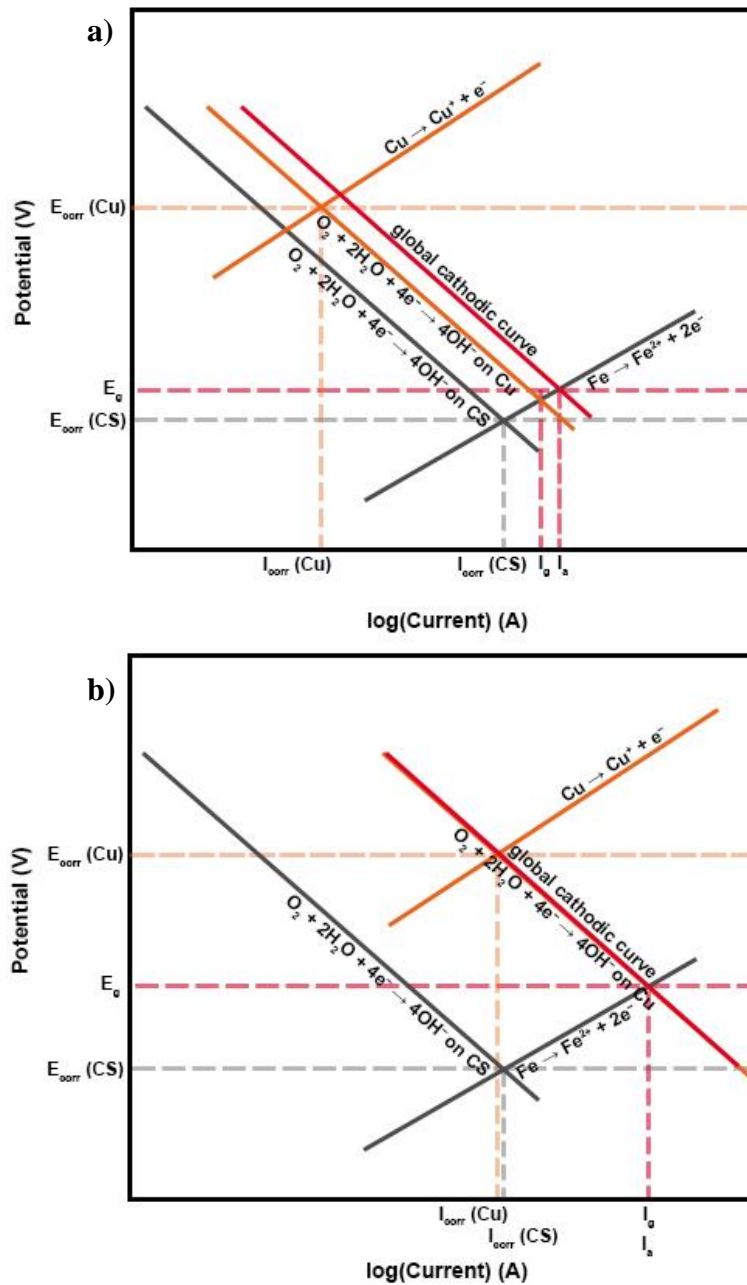


Figure 2.3 Evans diagrams of the Cu/CS galvanic couple in two scenarios: a) polarization of the CS is less significant, resulting in a non-negligible contribution to the anodic current from residual cathodic reactions on the CS ($I_g < I_a$), and b) polarization of the CS is more significant, thus residual cathodic activity on the CS makes a negligible contribution to the anodic current ($I_g = I_a$).

as a result of galvanic coupling, the magnitude of I_g should give an accurate measure of the corrosion rate [5].

In calculating electrochemical reaction rates, current density is often more meaningful than current [2], given by Equation 2.9:

$$\text{Rate} = \frac{I}{nFA} = \frac{i}{nF} \quad (2.9)$$

where in this work, i is current density in A cm^{-2} , and A is the wetted surface area in cm^2 . In classical corrosion, where only one metal surface is considered, when the total anodic current is equal to the total cathodic current, the anodic current density is equal to the cathodic current density. The same is not necessarily true in galvanic corrosion, where the redox processes are segregated onto two different surfaces, potentially with different surface areas. The passage of I_g between an anode and cathode with different surface areas results in different galvanic current density, or i_g , on each metal [6]. A large cathode, e.g. a defective noble metal coating, coupled to a small anode, e.g. the substrate exposed at the base of a through-coating defect, could result in large current densities at the anode.

2.2 Electrochemical Techniques

2.2.1 Galvanic Coupling at the Open Circuit Potential (OCP)

When two metals in a galvanic couple are naturally corroding while in intimate contact in the same electrolyte, charge is conserved in the system such that the net current is zero. As a result, the I_g of such a system cannot be measured by an external device. In order to measure the I_g of a galvanic couple, the metals can be coupled through a zero-resistance ammeter (ZRA) connected in series between them. The electron current flows out of the preferential anode, through the ZRA, across which the voltage drop is zero, and into the preferential cathode, bringing the two metals to a uniform coupled potential. I_g may then be measured and, if appropriate, interpreted as a proxy for the rate of galvanically induced corrosion. Additionally, while the two metals are externally coupled and at a shared potential, a voltmeter may be used to monitor that potential with respect to a stable reference electrode. The I_g may then be converted to i_g values for each metal by dividing by the wetted surface area of that metal.

2.2.2 Potentiodynamic Polarization (PDP)

E_g and I_g of a galvanic couple can be recorded under natural conditions by monitoring the system at open circuit, however, doing so yields no information about the kinetics of the individual half-reaction(s) occurring on each surface. In order to obtain such information, a technique called potentiodynamic polarization is often used in corrosion studies. PDP involves the application of a current to polarize the working electrode from an initial potential and sweep the potential at a predetermined rate over a predetermined range until it reaches a final value. A PDP can provide an estimate of the E_{corr} of the working electrode based on the point where the current crosses zero and changes sign, but more importantly, it can give insights into electrochemical behaviour far from the E_{corr} . When the electrode is polarized at least 50-100 mV distant from its E_{corr} , the rate of one half-reaction becomes negligible while the rate of the other half-reaction accounts for essentially the entire current response [7]. In this potential regime, the E vs. $\log I$ plot is linear if the dominant half-reaction is under activation control; the linear region is referred to as the Tafel region and its slope is referred to as the Tafel slope. If the rate of the dominant half-reaction is partially controlled by the rate at which reacting species diffuse to or from the surface, then the slope of the E vs. $\log I$ plot is large, and if it is entirely controlled by diffusion the slope is essentially infinite.

Potentiodynamic polarization is particularly useful in galvanic corrosion studies because the E_g and I_g can theoretically be found at the intersection of the PDP curves of the individual metals, obtained in identical environments. This intersection necessarily occurs between the cathodic branch of the more noble metal and the anodic branch of the more active metal, at a potential between the E_{corr} values of the metals. Comparing PDP curves for different metals can be a convenient way to study many combinations of galvanic couples without needing to construct cells with each combination.

However, values obtained from PDP data should be interpreted with some caution, as the dynamic nature of the technique precludes establishment of a perfectly steady state at the working electrode surface, the assumption of which provides the theoretical basis for the practice. PDP has been used successfully to predict E_g and i_g values for a variety of galvanic couples, though sufficiently accurate results were obtained only after lengthy pre-exposure periods [8]. This work uses PDP data primarily to confirm the trends observed in E_g and i_g rather than the exact values, as well as

elucidate the kinetics of each of the primary half-reactions.

2.2.3 Linear Polarization Resistance (LPR)

At the E_{corr} of a single corroding metal, the net current is zero, and thus the corrosion current density, i_{corr} , cannot be measured directly, but rather, other techniques must be employed to determine the corrosion rate. LPR is a commonly used electrochemical technique which provides a proxy value for instantaneous corrosion rate. LPR is a form of cyclic voltammetry, in which the potential is scanned from an initial value until it reaches the switching potential, then is scanned in the reverse direction. The LPR scan typically covers a maximum range of only 20 mV, symmetric about the E_{corr} , a range over which the E vs. i plot of the Wagner-Traud curve is effectively linear, as shown in Figure 2.4, and thus a relationship similar to Ohm's Law (Equation 2.10) applies.

$$R_p \propto \frac{\Delta E}{\Delta i} \quad (2.10)$$

ΔE is the change in potential in V, Δi is the change in current density in A cm^{-2} , and R_p is the polarization resistance in $\Omega \text{ cm}^2$. Additionally, such a small potential perturbation does not irreversibly change the working electrode surface, and thus it can be assumed the system remains at steady-state throughout the LPR scan.

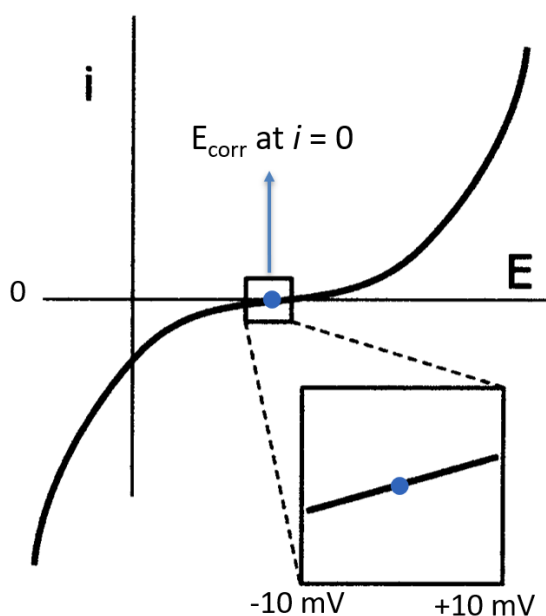


Figure 2.4 Schematic of a Wagner-Traud curve, highlighting the range over which the potential is scanned.

Because Wagner-Traud curves represent the superposition of contributions from two half-reactions, the Ohm's Law-type relationship cannot be directly used to calculate the i_{corr} , but rather it can be said that R is inversely proportional to i_{corr} . Thus, the LPR technique provides a way of comparing instantaneous corrosion rates over time, on different materials, and under different conditions. If sufficient information about the system is known, for example, the Tafel slopes for each half-reaction, the LPR technique can provide absolute corrosion rates.

2.2.4 Electrochemical Impedance Spectroscopy (EIS)

EIS is an electrochemical technique used to deconvolute signals given by a corroding surface and provide exceptional insight into corrosion mechanisms. In general, impedance describes the frequency-dependent relationships between potential and current (Equation 2.11) for elements in AC circuits; elements which, in a corroding system, are analogous to physical processes [9]:

$$Z(\omega) = \frac{\Delta E(\omega)}{\Delta i(\omega)} \quad (2.11)$$

where Z is the impedance in $\Omega \text{ cm}^2$. In EIS, the corroding system is perturbed by a small-amplitude ($\pm 10 \text{ mV}$ vs. DC potential) sinusoidal potential signal which generates a sinusoidal current response, Equation 2.12:

$$Z(\omega) = \frac{E_0 \sin(\omega t)}{i_0 \sin(\omega t + \theta)} \quad (2.1)$$

The input signal is applied over a broad range of frequencies, f , typically in the range of 10^{-3} to 10^6 Hz , where the angular frequency $\omega = 2\pi f$. Certain features of the system can cause the current response to be phase-shifted by angle θ with respect to the input signal of the same frequency, Figure 2.5. The impedance can be expressed as a complex number with a real and imaginary component, Equation 2.13 and 2.14:

$$Z(\omega) = |Z(\omega)| \cos \theta + j|Z(\omega)| \sin \theta \quad (2.13)$$

$$Z(\omega) = Z'(\omega) + jZ''(\omega) \quad (2.14)$$

where j is the imaginary unit value ($j^2 = -1$). Physical processes in the electrochemical cell can be represented by a mathematically equivalent circuit constructed from a combination of resistors, capacitors, inductors, and other elements (some of them just mathematical constructs). Each linear circuit element has a unique mathematical relationship to impedance, summarized in Table 2.1.

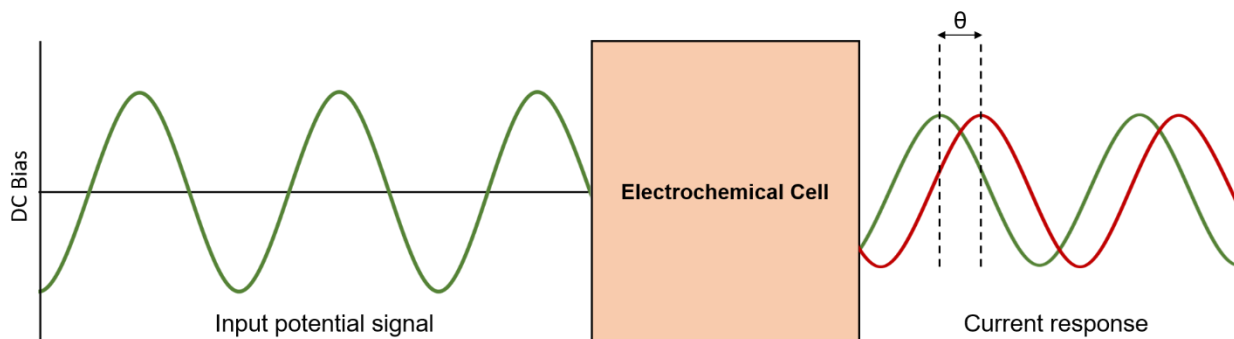


Figure 2.5 Schematic of a generic EIS experiment. It depicts the input sinusoidal potential perturbation and the electrochemical cell's output AC current response (red) with phase shift.

Table 2.1: Impedance functions for AC circuit elements.

Linear Circuit Element	Impedance
Resistor	R
Capacitor	$-\frac{1}{j\omega C}$
Inductor	$j\omega L$

A simple example of an equivalent circuit which can represent a corroding system is the modified Randles circuit, Figure 2.6, composed of a resistor R_s , in series with a parallel combination of a resistor R_{ct} , and a capacitor C_{dl} to represent solution resistance, charge transfer at the metal/solution interface, and the electric double layer, respectively. The solution resistance is associated with the resistance to charge transport through the electrolyte between the working and reference electrode, the electric double layer capacitance arises from charge storage in the arrangement of ions in the

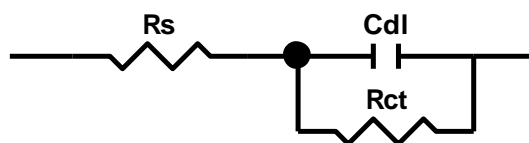


Figure 2.6 Simplified Randles circuit that might be used to model EIS data from a corroding system.

interfacial region, and the charge transfer resistance is related to the transfer of electrons and ions at the metal/solution interface. A key property of a circuit with R and C connected in parallel is the time constant $\tau = R \times C$, which is characteristic of how fast the natural response of the circuit is to potential perturbation.

An EIS experiment yields data which are most commonly plotted on Nyquist or Bode plots. The Nyquist plot is a plot of Z'' vs. Z' , or the imaginary part of the impedance vs. the real part of the impedance. The Bode plots are plots of $\log|Z|$ and θ vs. $\log(f)$, which can be used to identify the number of time constants and the frequency ranges which exhibit resistive (0° phase shift and horizontal in $|Z|$) or capacitive (90° phase shift and sloping in $|Z|$) responses. The Nyquist and Bode plots produced from the Randles circuit, Figure 2.7a-b, are characteristic of a circuit with a single time constant.

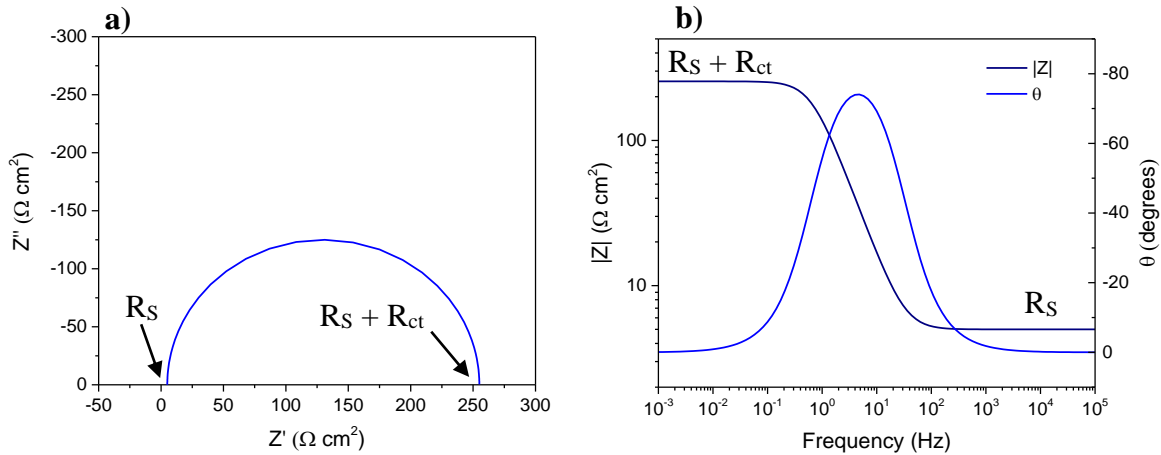


Figure 2.7 a) Nyquist plot and b) Bode plots simulated from a simplified Randles circuit. Important features (R_s , R_{ct}) are noted on each plot.

At the surface of a real corroding electrode, the electric double layer will often exhibit non-ideal capacitance which is highly dependent on the condition of the metal surface. The dispersion of capacitance across the surface results primarily from roughness, non-uniform oxide thickness, anion adsorption, particularly in Cl^- -containing solutions [10], and edge effects arising from finite electrode size. This non-ideal capacitance can be represented by the constant phase element (CPE), whose impedance can be described by Equation 2.15:

$$Z(\omega) = \frac{1}{C(j\omega)^p} \quad (2.15)$$

where the parameter P is related to deviation from ideal behaviour and approaches 1 for a true capacitor.

The constant phase element with $P = 0.5$ can be used to represent the Warburg impedance (W), which arises in cases where the current response may be limited by diffusion of reacting species. The finite Warburg applies to diffusion through a bounded diffusion layer, while the infinite Warburg represents the diffusion of species to or from bulk solution (from/to an effectively infinite distance), which is applicable under stagnant corrosion conditions. Equation 2.16 describes the impedance of an infinite Warburg element [11]:

$$Z(\omega) = \sigma \left(\omega^{-\frac{1}{2}} \right) (1 - j) \quad (2.16)$$

where σ is a function related to the diffusion and surface concentrations of reacting species. In theory, the Warburg element manifests as a 45° phase angle in the θ Bode plot and a line with a slope equal to 1 on the Nyquist plot, though in practice, the angle will be less than 45° due to variation in phase angle brought about by other circuit elements.

In electronics, an inductor is a device which can store energy in a magnetic field and disperse it by producing current; a key property of inductors is their ability to resist rapid changes in current. In EIS studies, a corroding system may exhibit pseudo-inductance, which manifests through processes which respond sluggishly to the potential perturbation. Such behaviour is often associated with adsorbed species, as in the dissolution of generic metal M, Reaction 2.1:



where k_1 and k_2 are rate constants. When the system is perturbed from steady state, the current associated with this mechanism is given by Equation 2.17:

$$i = Fk_1(1 - \vartheta) \quad (2.17)$$

where ϑ , in this context, represents the fractional surface coverage of the adsorbed intermediate. The admittance, Y (reciprocal of impedance), of this mechanism is given Equation 2.18:

$$\frac{di}{dE} = Y = F\beta_1 k_2 \vartheta_{SS} - Fk_1 \frac{d\vartheta}{dE} \quad (2.18)$$

with

$$\frac{d\theta}{dE} = \frac{(\beta_1 - \beta_2)k_2\theta_{SS}}{k_1 + k_2 + j\omega\phi} \quad (2.19)$$

and where β_1 and β_2 are the Tafel slopes for the 1st and 2nd steps in the mechanism, respectively, θ_{SS} is the steady-state surface coverage of the adsorbed intermediate, and ϕ is the number of sites at monolayer coverage [12]. When β_1 is equal to β_2 , then pseudo-inductive behaviour is not observed because there is no buildup of surface coverage of the adsorbed intermediate. If the release of the adsorbed intermediate has a larger Tafel slope than its formation, then surface coverage, and therefore current, will change sluggishly with potential perturbation and pseudo-inductive behaviour may be observed.

The interpretation of inductor elements in the modelling of corroding systems must be done carefully. Large values of inductance (L) are often required to fit corrosion data – inductances which would be impossible to achieve in physical solenoid inductors [12]. Rather, the formation and consumption of adsorbed intermediates in corrosion can be said to be analogous to an inductor because of the slothful response to the potential perturbation.

EIS is a powerful technique for corrosion studies, though there is inherent ambiguity regarding the physical source of the current response. Multiple equivalent circuits could theoretically fit the same set of data, and so determining the circuit that represents the true physical processes always requires complementary information.

2.3 Surface Analysis and Imaging Techniques

2.3.1 Raman Spectroscopy

Raman spectroscopy is a powerful technique for the *in situ* or *ex situ* evaluation of corrosion through identification of the various phases which form due to oxidation of the base metal. Raman spectroscopy is uniquely beneficial for corrosion studies because it is non-destructive and compatible with nearly any sample geometry [13].

Raman spectroscopy is based on the inelastic scattering of light by molecules and/or crystal phases on a sample. The sample is irradiated with a high-intensity monochromatic laser, the wavelength of which is dependent on the excitation source and typically falls in the visible range. The incoming

light excites the molecule or crystal phase to an unstable virtual state, followed by a de-excitation and release of a photon through several possible transitions, shown in Figure 2.8 [14].

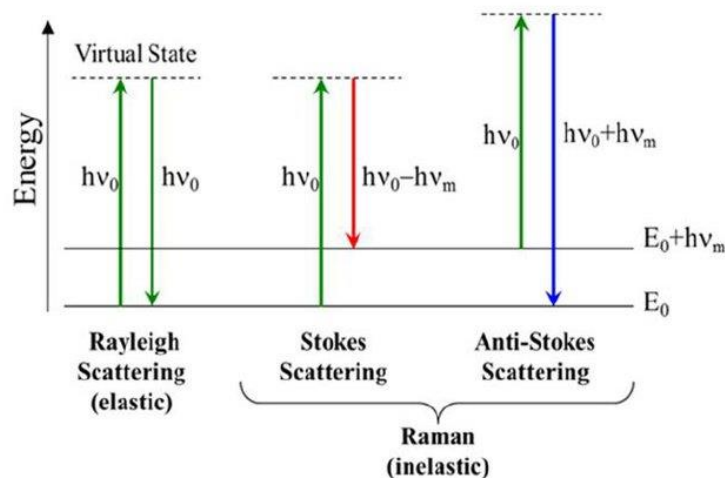


Figure 2.8 Diagram summarizing the possible transitions that can occur when using Raman spectroscopy [14].

A great majority of the photons undergo elastic, or Rayleigh scattering, and leave the sample at the exact same energy, however, a very small fraction of photons is inelastically scattered due to vibrational excitation of the chemical bonds [15]. Inelastically scattered outgoing photons may be less energetic than the incoming light (Stokes scattering), or more energetic than the incoming light (anti-Stokes scattering). Because the Stokes transition is initiated from the ground state, it is a much more probable and thus stronger process than the anti-Stokes transition, which is initiated from a vibrationally excited state [16]. Vibrational modes of the molecules/crystal phases present give rise to discrete energy transitions which are unique to the bond of origin. Raman spectra, Figure 2.9 [15], plot the intensity of the transitions as a function of the energy difference between the Stokes photons and the incident light. The spectra may feature several characteristic peaks which can be used to identify the molecule or crystal phase from which they originate.

Raman spectroscopy and IR spectroscopy share many similarities, both probing relatively low-energy vibrational transitions. They are, in fact, complementary techniques. Some vibrational modes are associated with a change in the dipole moment of the bond, and such modes can be said to be IR-active. To be Raman active, the vibration must induce a change in the polarizability of the bond. The polarizability of a bond is a tensor value which has contributions in three dimensions, represented by a *polarizability ellipsoid* around the bond. Raman-active vibrations induce changes

in shape, size, or orientation of the polarizability ellipsoid [15]. In symmetric molecules, no vibrational mode can be both IR- and Raman active, known as the *mutual exclusion rule*, though this does not necessarily apply to asymmetric molecules.

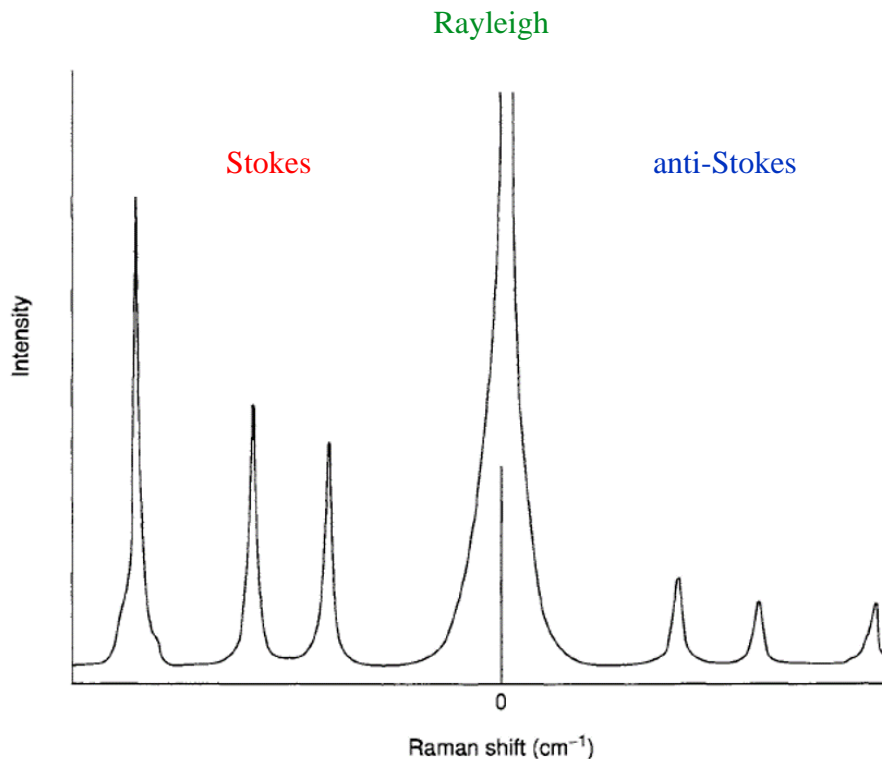


Figure 2.9 Raman spectrum (based on CCl₄) featuring both Stokes and anti-Stokes peaks, symmetrically placed about the Rayleigh peak [15].

In corrosion studies, the oxides and oxyhydroxides formed as a result of oxidation of the base metal often contain Raman-active modes. Raman spectroscopy of a corroded surface can give insight into the order in which corrosion products formed (e.g. evidence of a layered structure), where they preferentially formed (e.g. in pits or cracks), or the conditions under which they formed, as formation pathways are greatly affected by the environment. Raman spectroscopy can also be used to compare the crystallinity of solid phases, as more highly crystalline structures scatter light more cohesively and produce a stronger signal. One drawback of unenhanced Raman spectroscopy is the inherent weakness of the signals, which leads to poor signal-to-noise ratios. Another is the relatively low spatial resolution, at $\sim 1 \mu\text{m}$, which is adequate for abundant or larger-scale corrosion products, but falls short for some smaller-scale corrosion studies [17].

2.3.2 Scanning Electron Microscopy (SEM) and Energy Dispersive X-ray (EDX) Analysis

Scanning electron microscopy uses a focused electron beam to achieve much higher resolution than optical light-based microscopy, in the range of 50-100 nm [18]. Under vacuum, the electrons are accelerated towards the specimen surface while being focused by a series of ring magnets and scanned across the sample by deflector coils. The primary electron beam interacts with the sample in several different ways, producing analytically valuable emissions [19]. These interactions, summarized in Figure 2.10, are not strictly surface sensitive and some emissions may originate from a significant depth, which must be noted when interpreting data [20].

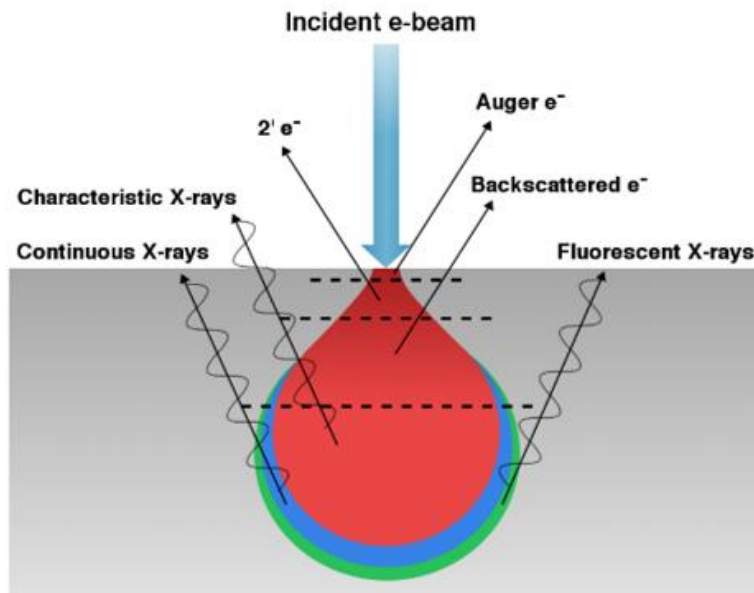


Figure 2.10 Schematic of electron beam interactions with a sample surface and sub-surface [20].

The high-resolution images are produced when secondary or backscattered electrons leaving the sample reach the detector. Secondary electrons originate from the atoms in the sample and are ejected from core shells when energy is imparted on them by the primary electron beam. Secondary electrons effectively reveal surface morphology because the intensity of secondary electrons reaching the detector is related to the topography of the sample, where valleys result in a lower electron intensity at the detector and a darker image, and hills result in a higher intensity and brighter image. Atoms in the sample can also elastically scatter primary beam electrons, producing backscattered electrons. Backscattered electrons can reveal information about the atomic weight of the atom which induced the scattering, as heavy atoms scatter electrons more effectively,

producing a brighter image than lighter atoms.

The emission of a secondary electrons leaves vacancies in the orbitals of the atom from which the electrons were emitted. An upper shell electron can then fall to the core shell to fill the vacancy, releasing energy in the form of X-rays which can be analyzed by EDX. The basis for EDX analysis is that these X-ray emissions are characteristic of the energy difference between the upper and core shells involved in the transitions, and thus, characteristic of the atoms of origin [21]. EDX is a powerful tool for elemental analysis and mapping with high spatial resolution, which, in corrosion studies, is vital for understanding the composition of films, deposits, and other features.

2.3.3 X-ray Micro-computed Tomography (micro-CT)

X-ray micro-computed tomography is based on the same technology as the medical CT scan, using the passage of X-rays through a sample to a detector to create 3D reconstructions of that sample. X-rays do not strongly interact with matter, and thus are very useful for imaging the interior of solid samples [22]. The sample is irradiated with X-rays which pass through the sample and form a projection on a detector opposite the source. These projections are collected as the sample is rotated slowly through either 360° or 180° to account for the entire structure, as depicted in Figure 2.11 [23]. The sample rotation is one of the main ways laboratory micro-CT instruments differ

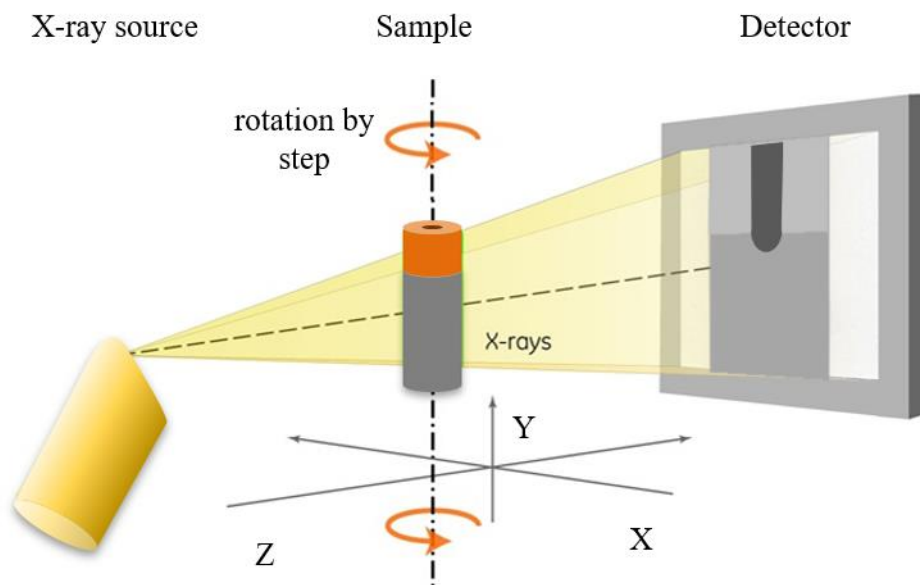


Figure 2.11 Schematic diagram of an X-ray micro-CT instrument with X-ray source, detector, and sample [23].

from medical CT scanners, where the sample (human) is stationary while the X-ray source and detector rotate.

The degree to which X-rays interact with a material can be described by the *linear attenuation coefficient* (μ), which is related to the absorption of X-rays by Equation 2.19:

$$A_{X\text{-ray}} = \frac{I_{\text{out}}}{I_{\text{in}}} = e^{-\mu t} \quad (2.19)$$

where $A_{X\text{-ray}}$ is the absorbance, I_{out} is the intensity of the X-ray leaving the material, I_{in} is the intensity of the incident X-ray, and t is the thickness of the sample [22]. Different phases in a material will attenuate X-rays differently, producing greyscale contrast in the X-ray projections. Denser materials will tend to absorb X-rays more effectively and appear brighter in the image, while void space appears black. Lab source X-rays used in micro-CT are polychromatic and of moderate intensity, so they require somewhat longer exposure times or more projections to produce high quality results. Synchrotron X-rays, however, can be monochromatic and extremely intense, thus producing excellent contrast images in a fraction of the exposure time.

The projections are reconstructed by computer software to form a complete volume which can then be viewed and analyzed as a whole or as image slices. For corrosion studies, X-ray micro-CT is extremely useful for the observation of corrosion in obscured or confined spaces, as well as below-surface damage. This technique allows for non-destructive imaging of corrosion within a through-coating defect, where other techniques would require destruction of the sample to see the coating/substrate interface inside the defect. The corrosion volumes can be used to calculate corrosion rate, based on volume and density of the material lost. The morphology and preferential direction of corrosion can also give valuable insight into the mode of eventual failure for the substrate, i.e. coating delamination or substrate penetration.

2.4 Materials

2.4.1 A516 grade 70 Carbon Steel

The UFC is to be shaped from A516 gr. 70 carbon steel, a readily available and commonly used material, whose composition is summarized in Table 2.2. This variety of carbon steel is extremely strong and is often used for high-pressure vessels, which makes it ideal for withstanding the pressures expected at the depth of the DGR. For this work, A516 gr. 70 steel was provided by the

Nuclear Waste Management Organization (NWMO) (Toronto, Canada), originally sourced from Integran Technologies, Inc. (Mississauga, Canada). A516 gr. 70 steel consists of microstructural grains of ferrite (α -Fe) as well as pearlite, which itself consists of alternating lamellae of ferrite and cementite (Fe_3C) [24].

Table 2.2: Percent composition of alloying elements in A516 grade 70 carbon steel (Fe balance).

Element	Weight Percent
C	0.31
Si	0.15-0.4
Mn	0.85-1.20
P	0.035
S	0.04

2.4.2 SKB Wrought Copper

The wrought Cu used in ZRA galvanic coupling experiments was supplied by the Swedish Nuclear Fuel and Waste Management Company (SKB) (Stockholm, Sweden). This particular type of Cu was O-free and doped with 30-100 ppm P, which improves its physical properties [25].

2.4.3 Electrodeposited Copper-Coated Steel

Over the majority of the UFC outer surface, the Cu coating is to be applied by electrodeposition. In this technique, a high purity Cu anode is dissolved under the application of a large current. The Cu ions then plate onto the steel, which acts as a cathode, by reducing back to Cu metal. The rate of Cu plating depends on the current density, which is typically applied by pulsed potentiometry [25]. In order to minimize O and C contamination in the coating, the electrodeposition process is conducted in a pyrophosphate bath [26]. The thickness of electrodeposited coatings can be tuned by the parameters such as current density and immersion time. On the UFC, the 3 mm thickness of the coating was decided based on a conservative corrosion allowance of 1.3 mm over 1 million years, which was calculated from expected corrosion rates under DGR conditions [27].

In this work, samples consisting of a 3 mm electrodeposited layer of Cu plated on A516 gr. 70 steel were cut from blocks provided by Integran Technologies, Inc. (Mississauga, Canada). Before the coating was applied, the CS surface was prepared by electrocleaning and acid pickling, then

de-rusted in alkaline cyanide solution immediately before immersion in the Cu strike tank (where the coating was applied).

2.4.4 Cold Spray Copper-Coated Steel

After the UFC is filled with fuel bundles, the hemispherical end cap must be welded onto the container body, leaving an uncoated strip of steel. Due to the complication of radiation shielding and high temperature, a dynamic cold spray method will be used to apply the Cu coating to the weld zone.

The application of the cold spray Cu coating involves the acceleration of small (10-100 μm) spherical particles of Cu powder towards the steel using a supersonic jet [28]. The particles undergo plastic deformation and mechanically bond to the substrate, forming a uniform coating. A key aspect of this technique is that the temperature of the particles stays far below the melting point of Cu (1085 $^{\circ}\text{C}$) so they remain solid throughout the entire process, thus limiting oxidation and changes to the physical properties of the Cu [26]. The Cu particles are accelerated in an inert carrier gas; first, lighter He gas is used to maximize the velocity of the Cu particles and adhesion of the initial coating layer, called the *strike layer* [26, 28]. The rest of the coating is then built up using N_2 as the carrier gas. The coating is then annealed to relieve residual stresses, which encourages recrystallization and improves the bonding of the particles to the substrate and the coating ductility [29].

Cold spray Cu-coated steel samples used in this work were cut from blocks provided by the National Research Council (NRC) Canada Industrial Materials Institute (Boucherville, Canada). The A516 gr. 70 steel substrate was first abraded with 24-grit alumina (Al_2O_3), then the coating was applied from high purity Cu feedstock with particle diameters averaging $\sim 40 \mu\text{m}$, carried by He gas to lay the strike layer and N_2 gas to build the coating. The coating was then annealed at 350°C for 1 hour under Ar atmosphere to prevent oxidation.

2.5 References

1. *Corrosion Vol. 1: Metal/Environment Reactions*. Butterworth Heinemann: Oxford, United Kingdom, 1994.
2. L. R. Faulkner A. J. Bard, *Electrochemical Methods, Fundamentals and Applications*, 2nd ed. John Wiley & Sons, Inc.: New York, USA, 2001.
3. G. S. Frankel, R. P. Frankenthal, *Corrosion Science: A Retrospective and Current Status in Honor of Robert P. Frankenthal*. Electrochemical Society: Pennington, USA, 2002.
4. L. Selwyn, Government of Canada, Canadian Conservation Institute:
<https://www.canada.ca/en/conservation-institute/services/workshops-conferences/regional-workshops-conservation/galvanic-corrosion.html>.
5. F. Mansfeld, *Corrosion* **1973**, 29, 403-405.
6. H. P. Hack, *Galvanic Corrosion Test Methods*. NACE International: Houston, USA, 1993.
7. R. G. Kelly, J. R. Scully, D. W. Shoesmith, R. Buchheit, *Electrochemical Techniques in Corrosion Science and Engineering*. Marcel Dekker, Inc.: New York, USA, 2003.
8. H. P. Hack, J. R. Scully, *Corrosion* **1986**, 42, 79-90.
9. J. R. Scully, *Corrosion* **2000**, 59, 199-218.
10. *Impedance Spectroscopy Theory, Experiment, and Applications*. 2nd ed.; John Wiley & Sons: Hoboken, USA, 2005.
11. Basics of Electrochemical Impedance Spectroscopy. Gamry Instruments, I., Ed. Gamry Instruments, Inc.: Warminster, USA, 2016.
12. S. Ramanathan, *ECS Trans.* **2011**, 33, 21-35.
13. D. Larroumet. Evaluation of the Raman spectroscopy technique for in situ corrosion studies. Sheffield Hallam University, Sheffield, United Kingdom, 2005.
14. K. Ismail. Fabrication and characterisation of SERS substrates through photo-deposition of Gold Nanoparticles. The Abdus Salam International Center for Theoretical Physics, Trieste, Italy, 2015.
15. J. R. Ferraro, K. Nakamoto, C. W. Brown, *Introductory Raman Spectroscopy*. 2nd ed.; Elsevier: Amsterdam, Netherlands, 2003.
16. G. S. Bumbrah, R. M. Sharma, *Egypt. J. Forensic Sci.* **2015**, 6, 209-215.
17. F. Adar, S. Mamedov, A. Whitely, *Microsc. Microanal.* **2005**, 11, 728-729.

18. S. Swapp Scanning Electron Microscopy (SEM).
https://serc.carleton.edu/research_education/geochemsheets/techniques/SEM.html (accessed June 22, 2020).
19. W. C. Nixon, *Philos. Trans. R. Soc. London, Ser. B* **1971**, 261, 6.
20. P. J. D. Whiteside, J. A. Chininis, H. K. Hunt, *Coatings* **2016**, 6, 1-26.
21. J. Goodge Energy Dispersive X-ray Spectroscopy (EDS).
https://serc.carleton.edu/research_education/geochemsheets/eds.html (accessed August 6, 2019).
22. R. Molteni, *Micro-computed Tomography (micro-CT) in Medicine and Engineering*. Springer Nature Switzerland AG: Cham, Switzerland, 2020.
23. Stellenbosch University, Central Analytical Facilities: Stellenbosch, South Africa.
24. S. Hill. The Corrosion of Carbon Steel under Deep Geologic Nuclear Waste Disposal Conditions. The University of Western Ontario, London, Ontario, 2016.
25. P. G. Keech, P. Vo, S. Ramamurthy, J. Chen, R. Jacklin, D. W. Shoesmith, *Corros. Eng. Sci. Techn.* **2014**, 49, 425-430.
26. C. H. Boyle, S. A. Meguid, *Nucl. Eng. Des.* **2015**, 293, 403-412.
27. J. R. Scully, D. Feron, H. Hanninen *Review of the NWMO Copper Corrosion Program*; NWMO-TR-2016-11; Nuclear Waste Management Organization: Toronto, Canada, August 2016, 2016; p 31.
28. P. Jakupi, P. G. Keech, I. Barker, S. Ramamurthy, R. L. Jacklin, D. W. Shoesmith, D. E. Moser, *J. Nucl. Mater.* **2015**, 466, 1-11.
29. W. Li, C. Li, H. Liao, *J. Therm. Spray. Technol.* **2006**, 15, 206-211.

3. Galvanic Coupling of Carbon Steel and Copper in Chloride

3.1 Introduction

In Canada's plan for the disposal of used nuclear fuel, the fuel bundles will be housed within Cu-coated CS containers which will be placed >500 m underground in a DGR. The main purpose of the Cu coating is to provide corrosion resistance and protect the underlying steel, so the coating will be inspected thoroughly before container placement. If a container is placed in the DGR with an undetected defect penetrating the thickness of the coating, galvanic coupling of the Cu and CS would be theoretically possible. The galvanically accelerated corrosion of the substrate steel is considered a possible failure mode of the container, potentially leading to the release of harmful radionuclides. The possibility of galvanic corrosion must be assessed over the range of conditions expected in the DGR, which are expected to evolve from hot and dry to cool and moist, while also transitioning from oxic to anoxic [1]. The environment at the container surface is expected to be abundant in Cl^- , which has complex, interconnected effects on corrosion. Cl^- not only encourages metal dissolution, but also affects key environmental factors such as oxidant availability and solution conductivity. O_2 solubility in saline solutions decreases with increasing salt concentration [2]; a high $[\text{Cl}^-]$ environment can thereby limit availability of the main oxidant while simultaneously contributing to high electrolyte conductivity, which is conducive to corrosion. This work investigates the Cu/CS galvanic couple under aerated and de-aerated conditions in the presence of various concentrations of Cl^- in order to better understand these effects.

In noble metal coatings, the size of the defect is a key factor in the severity of the galvanic corrosion, where the most egregious damage would occur when a minuscule area of exposed substrate is coupled to a comparatively vast coating area, because the current density at the substrate would be very high. Studies of galvanic corrosion at the large cathode-to-anode area ratios relevant to a defective coating are rare, and exceedingly so for the Cu/CS couple specifically. This work uses a unique experimental setup which allows for the achievement of Cu:CS area ratios of up to ~2500:1 with a high degree of radial symmetry, as would likely be the case in a defective coating. Assuming infinite electrolyte conductivity, the entire area of the coating would be available to participate in the galvanic couple. In practice, the distance over which the metals can couple, called galvanic "throwing power", is limited by the finite conductivity of the electrolyte.

The galvanic effect diminishes with distance from the bimetallic junction due to iR drop through the solution [3]. Therefore, one of the goals of this study was to determine how the effective Cu:CS area ratio may be constricted as a function of solution conductivity.

Previous work [4-6] has studied the galvanic corrosion of Cu-coated CS at a drilled hole (simulated defect) through the coating. In these experiments, the potential of the couple, E_g , could be measured but because the metals were in intimate contact in the electrolyte, the galvanic current, I_g , passed directly from one metal to the other making it impossible to measure externally. The I_g is a vital piece of information in galvanic corrosion studies because it gives insight into electrochemical kinetics and therefore the rate of galvanic corrosion. The I_g , when converted to galvanic current density on CS, i_g , provides insight into the CS degradation, specifically. In order to extract this valuable information, this study makes use of a zero-resistance ammeter (ZRA) to galvanically couple Cu and CS externally while they are insulated from each other in solution. Therefore, we were able to measure E_g and I_g simultaneously, revealing both the thermodynamic and kinetic nature of the galvanic corrosion process.

In the DGR, the possible galvanic corrosion processes at a through coating defect will be controlled by a number of factors arising from the combination the Cl^- concentration near the container, whether the system is oxic or anoxic, and the Cu:CS area ratio. These factors were investigated using OCP measurements and PDP to determine E_g and i_g , complemented by surface analysis techniques including Raman spectroscopy and SEM/EDX.

3.2 Experimental Methods

3.2.1 Sample Preparation

Galvanic corrosion experiments were performed using A516 gr. 70 carbon steel provided by NWMO and made into cylindrical electrodes of varying diameters, as well as P-doped, O-free Cu provided by the Swedish Nuclear Fuel and Waste Management Co. (SKB) and made into ring electrodes with varying outer and inner diameters. The working surface areas of the CS electrodes ranged from 0.004 cm^2 to 1.0 cm^2 while the surface areas of the Cu rings were 1.0 cm^2 and 10.0 cm^2 . By combining CS and Cu electrodes, we achieved area ratios from 1:1 to ~2500:1. The electrodes were first ground to a P1200 finish using SiC paper, then a wire was soldered, with a Pb/Sn solder formula, onto the back face and the electrodes were sonicated in methanol. A length

of PTFE heat-shrink tubing was placed over the wire for insulation before 3 layers of Amercoat 240 epoxy paint (PPG Protective & Marine Coatings) were applied so as to leave only the top face of the electrode exposed. The epoxy was cured for 24 hours at 60 °C after each coat was applied. Before each experiment, the exposed surfaces of the electrodes were ground to a p2500 finish with SiC paper and sonicated in methanol.

3.2.2 Experimental Setup

In the experimental setup that was used, shown in Figure 3.1, the CS electrode was situated at the centre of the Cu ring with the surfaces flush with each other [7]. The electrodes were immersed together in the main compartment of a three-compartment electrochemical cell with compartments separated by dense glass frits. Experiments were conducted in solutions of reagent grade NaCl (Fisher Scientific) made to concentrations ranging from 0.001 M to 3 M with ultrapure water (resistivity of 18.2 MΩ cm) from a Thermo Scientific Barnstead Nanopure water purification system. The NaCl solution was sparged with medical grade air (PRAXAIR) for 30 minutes or with high-purity Ar (PRAXAIR) for 60 minutes prior to the start of and throughout each experiment.

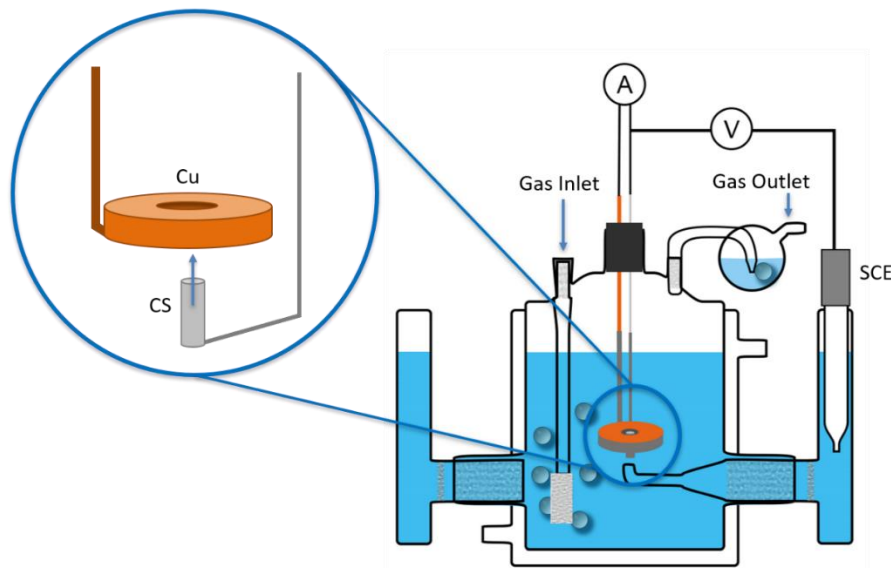


Figure 3.1 Schematic diagram of the three-compartment electrochemical cell used for galvanic coupling experiments.

The CS and Cu were externally coupled through a Keithley 6514 system electrometer acting as a ZRA, and I_g was recorded with National Instruments Lab-view software written in-house. E_g was monitored by connecting a potentiostat (Solartron 1480 Multistat and Solartron 1287) to the CS as

the working electrode and a saturated calomel electrode (SCE, +0.241 V vs. SHE) as the reference electrode and recording the measurements using CorrWare software. The reference electrode was housed in an arm of the cell, equipped with a Luggin capillary to minimize iR drop between the working and reference electrodes. After the corrosion experiment, the CS electrode was removed from the cell, rinsed with ultrapure water, dried in a stream of Ar, and stored in an anaerobic chamber until surface analysis was performed. The galvanic current density (i_g) sustained on the CS was determined by normalizing the total galvanic current (I_g) to the CS surface area (A_{CS}) by Equation 3.1:

$$i_g = \frac{I_g}{A_{CS}} \quad (3.1)$$

PDP scans were conducted in a three-compartment cell sparged with medical grade air, with either CS or Cu as the working electrode in the main cell compartment, an SCE reference electrode in the cell side arm featuring the Luggin capillary, and a Pt flag as the counter electrode in the other cell side arm. Electrolyte compositions mirrored those used in galvanic corrosion experiments. All PDP scans were initiated once the CS or Cu came to a steady-state E_{corr} , and the CS was then gradually polarized +550 mV vs open circuit potential (OCP) and Cu was polarized to -550 mV vs OCP at a scan rate of 10 mV min⁻¹.

3.2.3 Surface Analysis

Surface analysis was performed at Surface Science Western (London, Canada) using a Renishaw InVia Reflex Raman Spectrometer with a HeNe 633 nm wavelength laser at an 1800 l mm⁻¹ grating for Raman spectroscopy and a Hitachi SU3500 Variable Pressure SEM with an Oxford AZtec X-Max50 SSD X-ray analyzer or a Hitachi SU3900 Large Chamber Variable Pressure SEM equipped with an Oxford ULTIM MAX 65 SDD X-ray analyzer for SEM/EDX.

3.3 Results

3.3.1 Galvanic Coupling at Different Copper-to-Steel Area Ratios

Galvanic corrosion experiments were conducted until steady state was achieved in 0.1 M and 3 M NaCl solutions at Cu:CS area ratios ranging from 1:1 to ~2500:1. The E_g and i_g data were plotted as a function of time in Figure 3.2. The i_g remained relatively stable without long-prevailing upward or downward trends over the duration of the whole experiment, with the exception of a

very shallow decline at 1:1 Cu:CS and some instability at 100:1 Cu:CS, both in 0.1 M NaCl. Thus, the achievement of steady-state E_g typically defined the termination of the experiments. At low

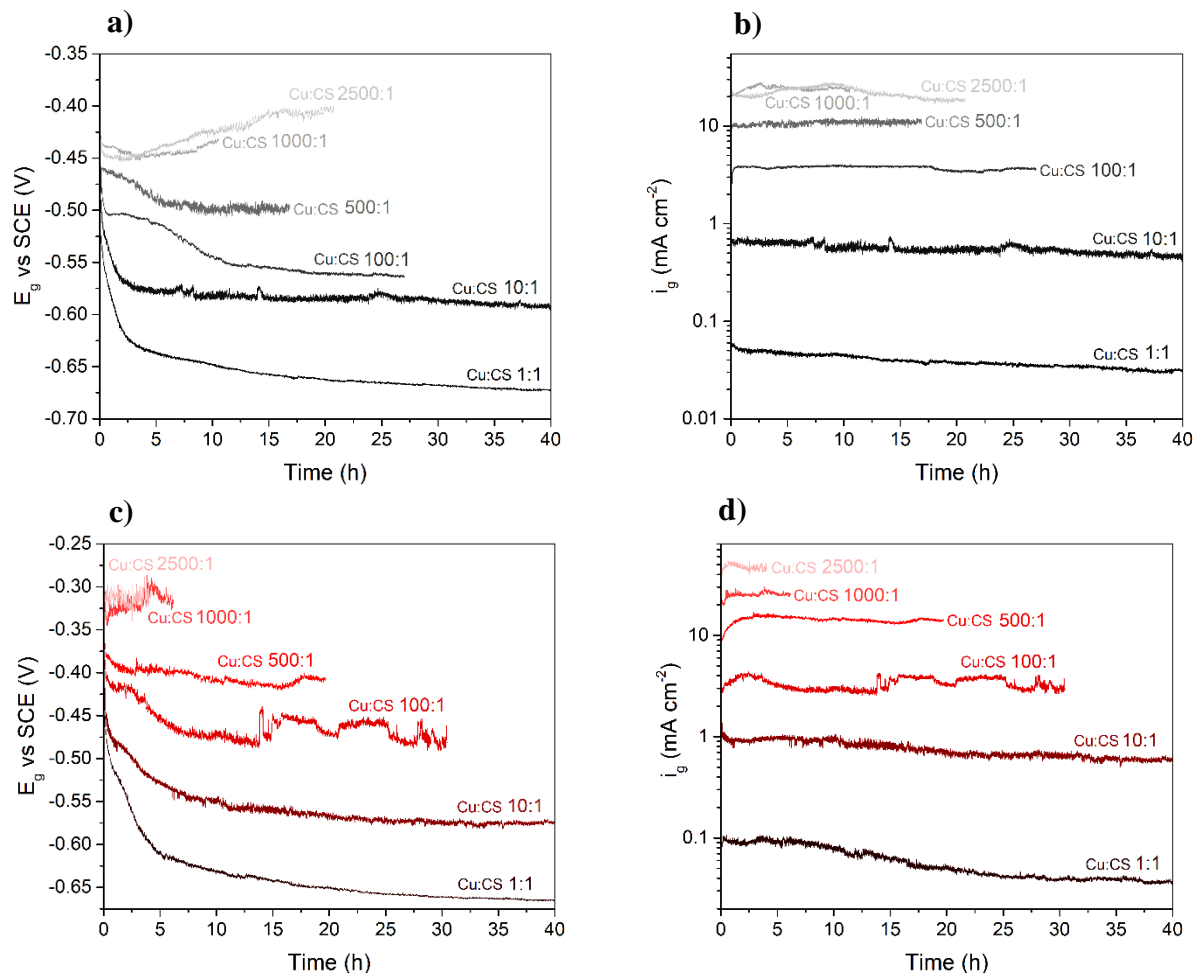


Figure 3.2 Plots of a) E_g in 3 M NaCl, b) i_g in 3 M NaCl, c) E_g in 0.1 M NaCl, and d) i_g in 0.1 M NaCl, plotted as functions of time at different Cu:CS area ratios, stated on the plot.

and intermediate Cu:CS area ratios, the E_g tended to exhibit a steep initial downward trend with time, followed by a continued shallow decline, the duration of which was generally shorter as the Cu:CS area ratio increased. As a result, it took significantly longer for the Cu/CS couples at lower Cu:CS area ratios to come to a steady state. This behaviour was indicative of the gradual buildup of a corrosion film on the CS, which may impede the corrosion process. However, at area ratios of 1000:1 and ~2500:1 in both 0.1 M and 3 M NaCl, the E_g actually became more positive over time, which would suggest that the conditions at the CS became increasingly oxidizing and these samples did not experience the same film formation process as at lower area ratios.

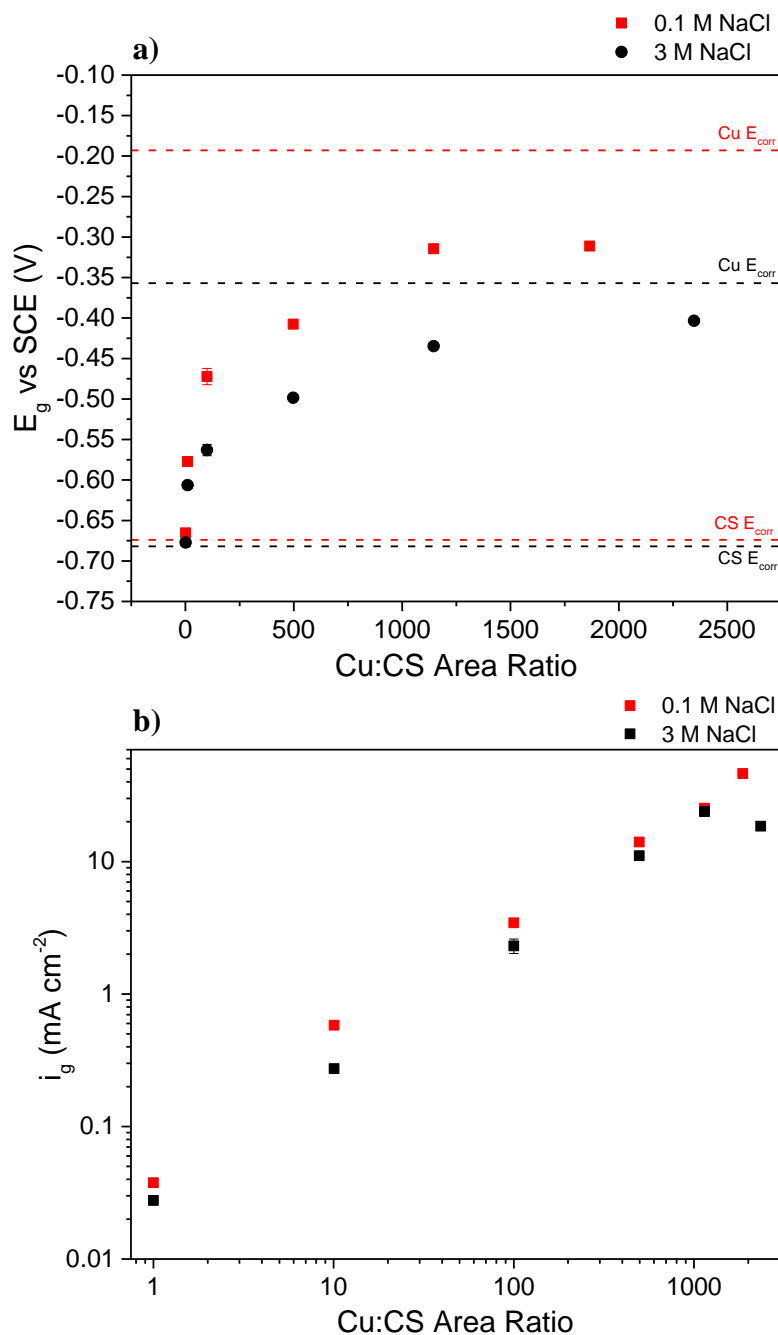


Figure 3.3 Steady-state a) E_g , and b) i_g recorded in 0.1 M and 3 M NaCl, plotted as a function of Cu:CS area ratio. Steady-state E_{corr} of CS and Cu in 0.1 M and 3 M NaCl are plotted as horizontal dashed lines for reference.

The steady-state E_g and i_g values were obtained by taking the average of the last hour of data and were plotted as a function of Cu:CS area ratio in Figure 3.3. As expected, E_g settled in between the respective E_{corr} values of the Cu and CS, at all area ratios. At a Cu:CS area ratio of 1:1 in both 0.1 and 3 M NaCl, the E_g was only 5-9 mV more positive than the E_{corr} of CS. In the case of such minor polarization, there would be significant cathodic activity occurring on the CS surface [8].

By contrast, the Cu was polarized negatively by >400 mV from its E_{corr} . Such unequal polarization suggests that the anodic reaction on CS was much faster than the cathodic reactions on the Cu, because mixed potentials settle closer to the reversible potential of the faster half-reaction. As the Cu:CS area ratio increased, the E_g increased in a logarithmic manner. When the Cu:CS area ratio increased beyond 100:1, the E_g was greater than 100 mV more positive than the E_{corr} of CS, at which point there would be negligible cathodic activity on the CS surface [9-10].

The steady-state i_g increased proportionately with Cu:CS area ratio in both 0.1 M and 3 M NaCl, with the exception of the measurement at 2347:1 in 3 M NaCl, which deviated downward from the linear trend. The scaling of i_g with the surface area of the more noble metal suggests that O₂ reduction on the Cu was rate-limiting, consistent with other work [11-12]. At high ($\geq 100:1$) Cu:CS area ratios, the i_g values exceeded 1 mA cm⁻², and the test solution rapidly took on a vivid orange hue and filled with dark orange corrosion products which settled to the bottom of the cell or atop the Cu and CS electrodes. The linearity of the i_g vs. Cu:CS area ratio plot and the magnitude of the currents were consistent with the behaviour of smaller area ratio Cu/mild steel couples exposed to aerated NaCl solution [13].

3.3.2 Surface Analysis of Carbon Steel Corroded at Different Copper-to-Steel Area Ratios

SEM images of the CS surface obtained after the immersion experiments, Figure 3.4, reveal a significant increase in damage to the electrodes as the Cu:CS area ratio increased. As suggested in the E_g vs. time profiles, the CS corroded at 1:1 Cu:CS area ratio had gradually formed a compact oxide film covering the surface. Dome-like structures and large flowery clusters were positioned atop the compact film, though these features were weakly adhered and their distribution on the surface would be at least partially dependent on the post-experimental sample treatment. The morphology of the CS corroded at a 10:1 area ratio was similar to that at a 1:1 area ratio, and the film was observed to have a nest-like structure. At intermediate Cu:CS area ratios (100:1 and 500:1), some areas of the surfaces had nodule-like features, and though they did feature flowery deposits similar to those at lower Cu:CS area ratios, these deposits were smaller and far less abundant. At high Cu:CS area ratios, the oxide film formed much more rapidly and was observed to be fractured and collapsed, likely induced by exposure to vacuum during post-mortem sample preservation, indicated by its thin, brittle structure. Additionally, due to the swift achievement of steady-state, oxide crystals atop the film were extremely small and sparse.

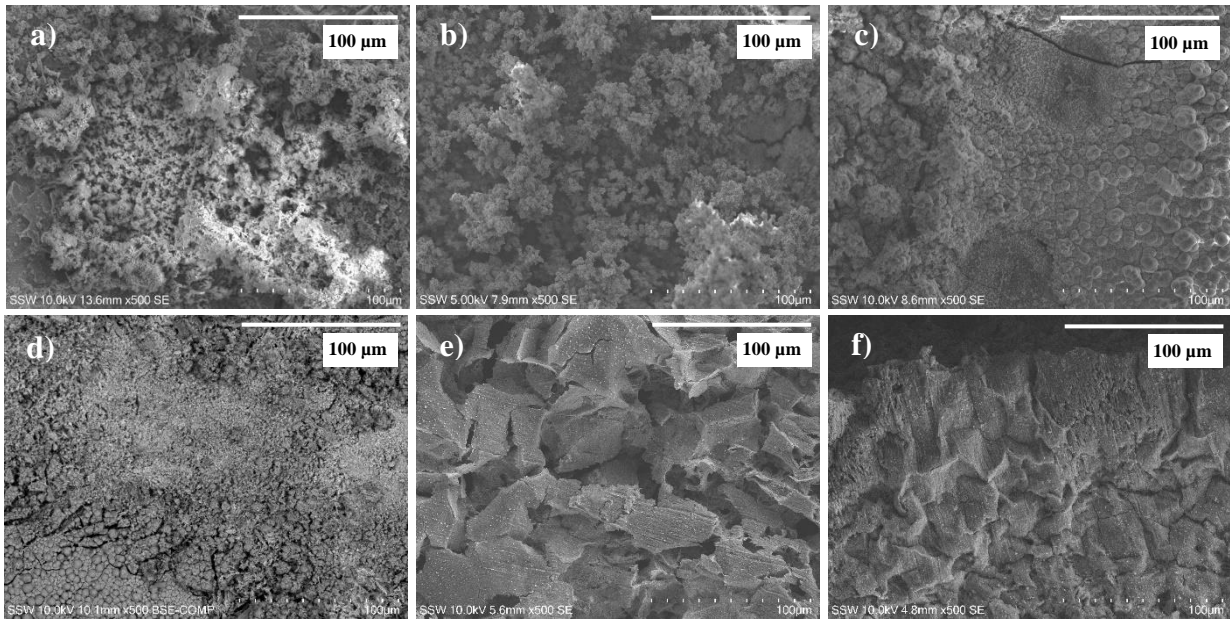


Figure 3.4 SEM images of corroded CS in 0.1 M NaCl at Cu:CS area ratios of a) 1:1, b) 10:1, c) 100:1, d) 500:1, e) 1000:1, and f) 1866:1.

EDX spectra collected on the CS surface after corrosion at a 1000:1 Cu:CS area ratio, Figure 3.5, revealed a cracked, thin oxide film (areas 1, 2, 3, and 4) composed of between 41.6% and 60.1% Fe by weight, and between 18.0% and 26.3% O by weight. Some areas (5 and 6) were bare, corroded steel, possibly exposed by cracking and shrinkage of the oxide; these regions also exhibited a very high Cu content, at ~19% by weight, compared to 1-3% Cu in areas 1-4. Other samples corroded at a large Cu:CS area ratio exhibited similar behaviour, where EDX mapping, Figure 3.6, revealed Cu enrichment collocated with enriched Fe and depleted O (bare steel), where

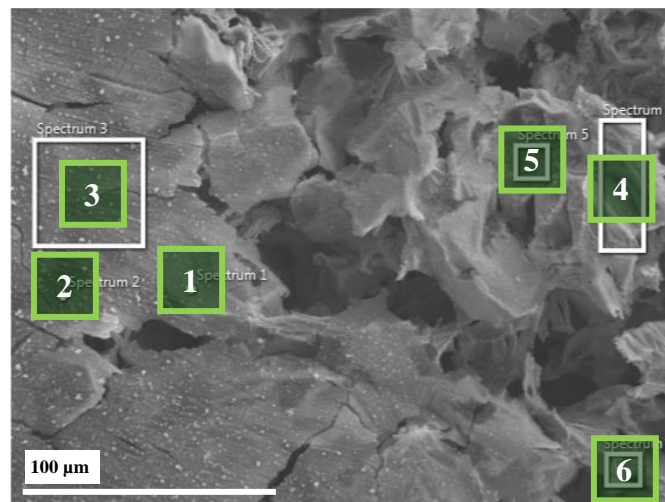


Figure 3.5 SEM micrograph of CS corroded at a Cu:CS area ratio of 1000:1 in 0.1 M NaCl. Green numbered boxes indicate areas where EDX spectra were taken.

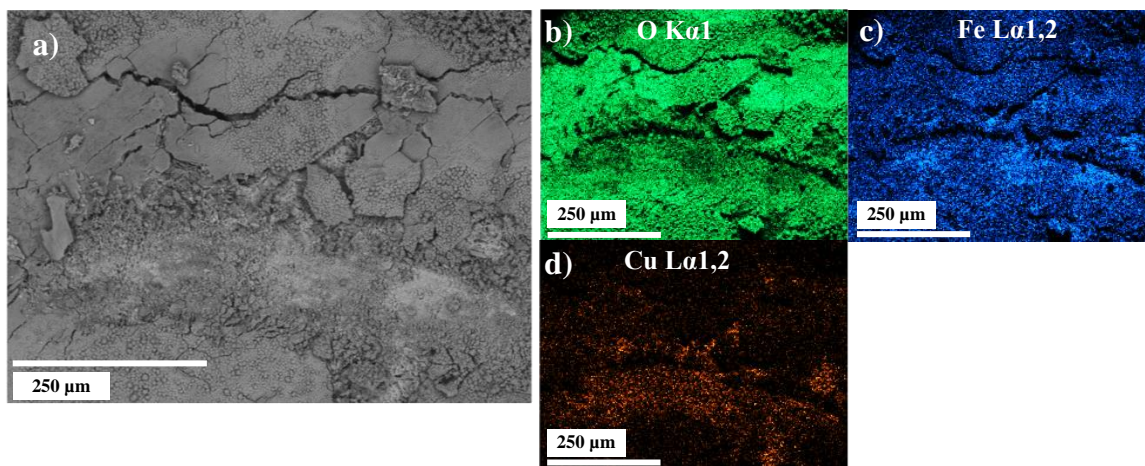


Figure 3.6 a) Electron image of CS corroded at a Cu:CS area ratio of 500:1 in 3 M NaCl and b-d) EDX maps of O, Fe, and Cu, respectively.

oxide had flaked off. Generally, the amount of Cu found on the CS surface increased with increasing Cu:CS area ratio.

Raman spectra were collected at multiple points on the CS surfaces after the samples' extraction from the electrochemical cell. Representative areas of CS samples corroded at a Cu:CS area ratio of 1:1 are shown in Figure 3.7, though spectra were taken across the entire surface and at various depths, Figure 3.8. The compact lower layer of the corrosion film on the 1:1 sample showed a strong peak at 680 cm^{-1} and a small peak at 540 cm^{-1} , characteristic of magnetite [14-15]. Goethite, characterized by a strong peak at 390 cm^{-1} , was found throughout the corrosion film as well, often as part of a mixed signal with other oxides [14, 16]. Atop the compact film, the surface showed significant coverage by large, yellow-orange formations, which gave strong peaks at 250 cm^{-1} and



Figure 3.7 Optical images of CS corroded at a Cu:CS area ratio of 1:1 in a) 3 M and b) 0.1 M NaCl.

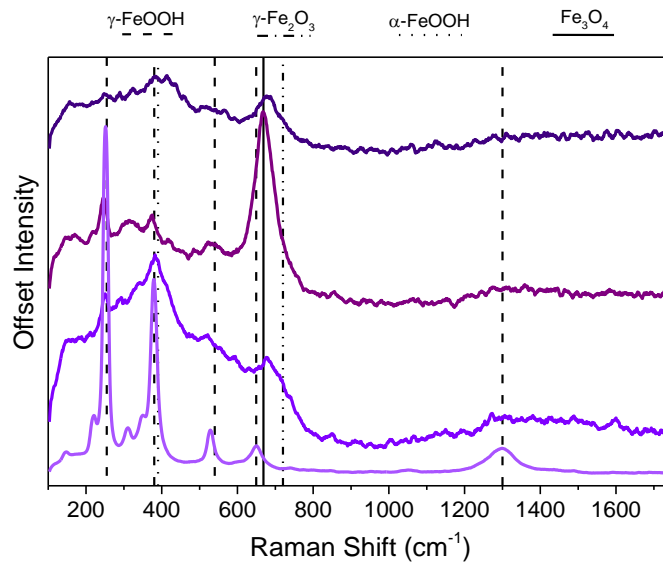


Figure 3.8 Raman spectra recorded on CS corroded at a 1:1 Cu:CS area ratio in 3 M NaCl.

380 cm^{-1} and smaller peaks at 528 cm^{-1} and 1300 cm^{-1} , all characteristic of lepidocrocite [14, 16-17]. The slow formation of the corrosion film at low (1:1 and 10:1) Cu:CS area ratios resulted in highly crystalline corrosion products which gave sharp Raman peaks.

CS corroded at a Cu:CS area ratio of 100:1, optical images of which are shown in Figure 3.9, showed a dark lower layer with nodule-like features, corresponding to the compact film, and some orange clusters scattered atop the film. Raman spectra, Figure 3.10, of the lower film layer featured a strong peak spanning 670 cm^{-1} to 720 cm^{-1} , indicative of maghemite [18]. The orange crystals,

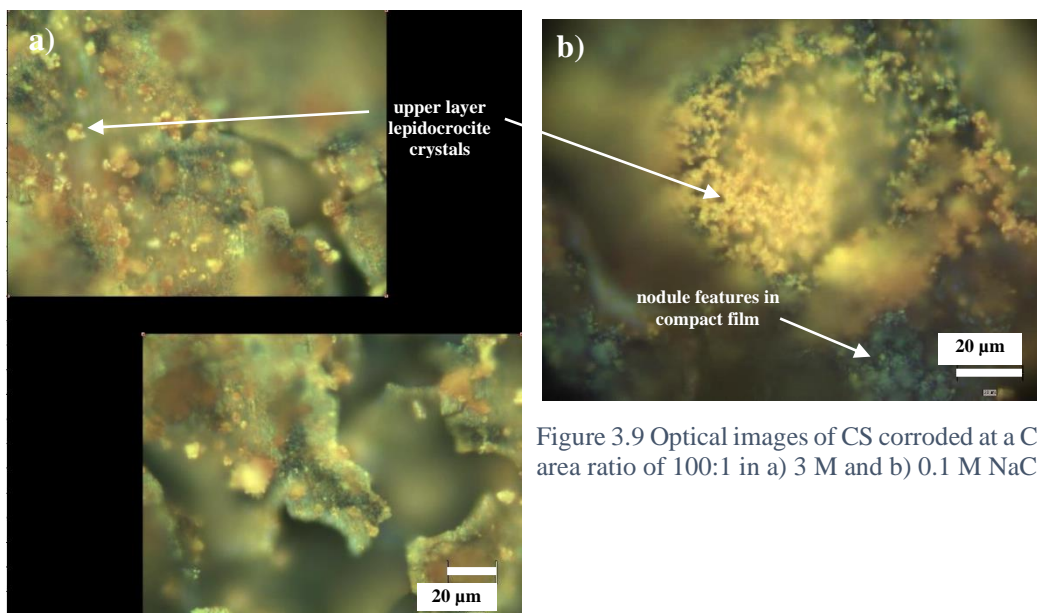


Figure 3.9 Optical images of CS corroded at a Cu:CS area ratio of 100:1 in a) 3 M and b) 0.1 M NaCl.

identified as lepidocrocite by the main peaks at 250 cm^{-1} and 380 cm^{-1} , were smaller and thus gave a weaker signal than similar clusters on samples with 10:1 or 1:1 Cu:CS area ratios .

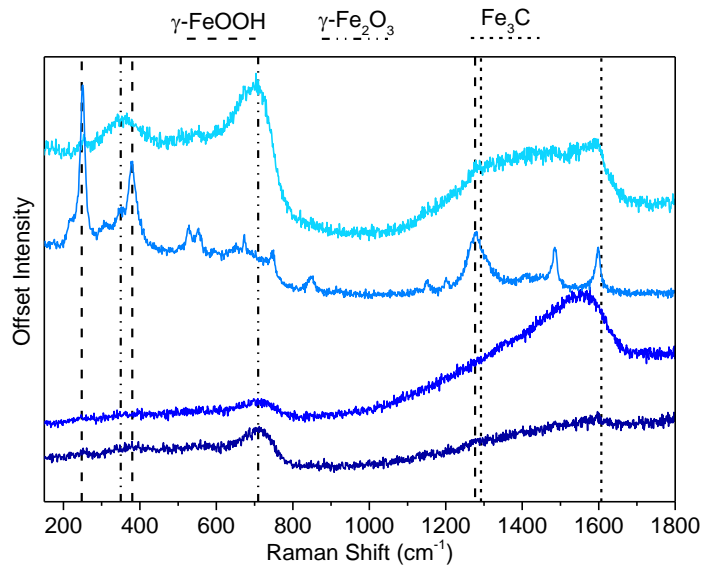


Figure 3.10 Raman spectra recorded on CS after corrosion at a Cu:CS area ratio of 100:1 in 0.1 M NaCl.

When the Cu:CS area ratio increased to 1865:1, an optical image of the surface, Figure 3.11, showed coverage by a dark film and extensive damage. Raman spectra, Figure 3.12, recorded on the surface showed weak signals at 668 cm^{-1} and 540 cm^{-1} , suggesting that the thin oxide film was primarily composed of magnetite [18]. The broad asymmetric peak between 1400 cm^{-1} and 1600 cm^{-1} was characteristic of the cementite (Fe_3C) phase in lamellar pearlite grains of the carbon

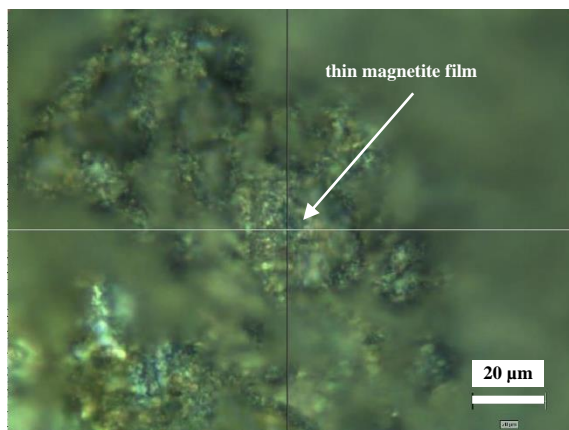


Figure 3.11 Optical image of CS corroded at a Cu:CS area ratio of 1865:1 in 0.1 M NaCl.

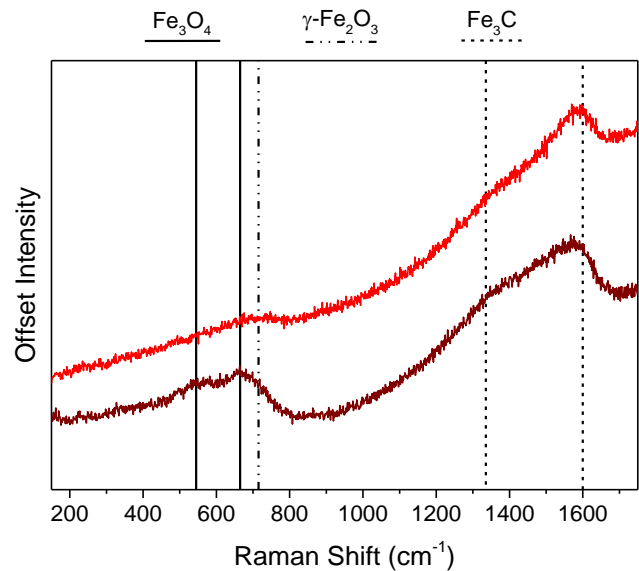


Figure 3.12 Raman spectra recorded on CS after corrosion at a Cu:CS area ratio of 1865:1 in 0.1 M NaCl.

steel, where the α -Fe bands were preferentially dissolved [19-20].

3.3.3 Prediction of Coupled Potential and Galvanic Current by PDP

Polarization curves recorded on CS and Cu in aerated 3 M and 0.1 M NaCl are shown in Figure 3.13, and the intersection of E_g and i_g at each concentration is highlighted. E_g and i_g were found at each intersection of the anodic branch of the polarization curve on CS and the cathodic branch of the polarization curve on Cu. The current response on CS was normalized to 1 cm² while the current response on Cu was multiplied by the Cu ratio: 1, 10.07, 100.7, 497.3, 1145.5, 1865.7, or 2347.4 as needed.

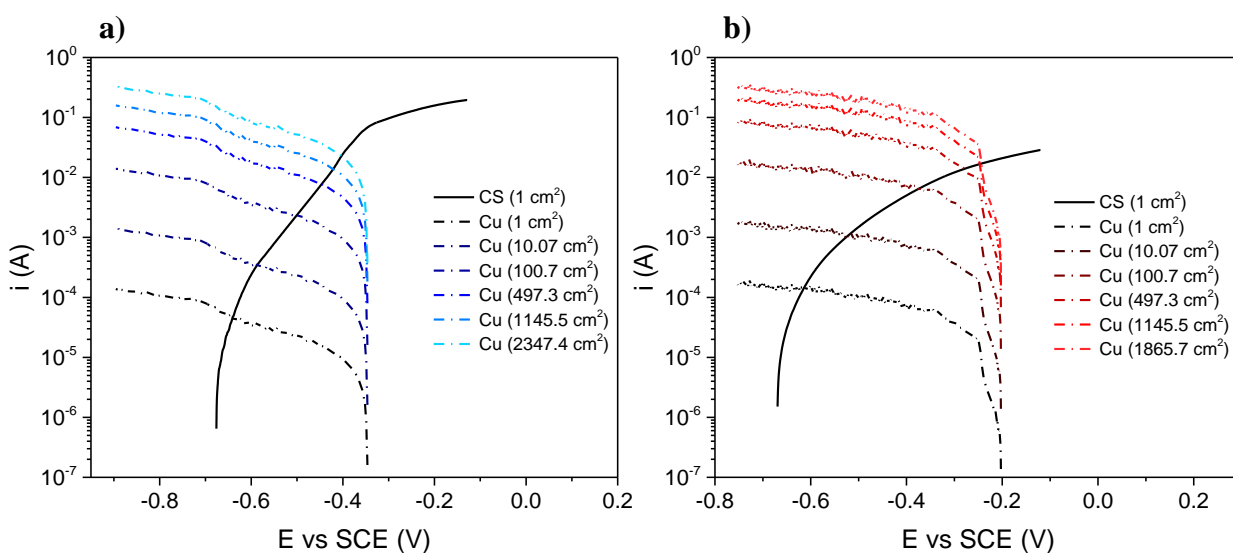


Figure 3.13 PDP curves recorded on CS and Cu in solutions with $[Cl^-]$ of a) 0.1 M or b) 3 M, where the current measured on the Cu curves was multiplied by the relative area of Cu for given Cu:CS area ratios.

The anodic branch of the polarization curve on CS was recorded, corresponding to oxidation of $Fe_{(s)}$ to Fe^{2+} , and the cathodic branch of the polarization curve on Cu was recorded, corresponding to reduction of O_2 to OH^- . Tafel (or E -log I) slopes of the CS PDP curves were determined by applying a linear fit to the data, starting from ~ 100 mV removed from the E_{corr} over a range spanning at least 100 mV or at least 1 order of magnitude change in current; the Tafel slope is reported Table 3.1 using the units mV per decade change in current density.

Table 3.1 E - $\log I$ slopes for PDP data recorded on CS and Cu in 0.1 M and 3 M Cl^- .

$[\text{Cl}^-]$ (mol L^{-1})	CS E - $\log I$ slope (mV decade $^{-1}$)	Cu E - $\log I$ slope (mV decade $^{-1}$)
3	105	423
0.1	182	674

The anodic branch of the polarization curve on CS did not show any active-to-passive transition, appearing to remain actively dissolving across the entire potential range, consistent with other work on CS corrosion in Cl^- -containing solutions [21-23]. In 3 M Cl^- , the Tafel slope of 105 mV decade $^{-1}$ suggests that the rate of Fe oxidation was controlled by charge-transfer. The Tafel slope increased when $[\text{Cl}^-]$ fell to 0.1 M, indicating some blockage of the CS surface by a protective oxide. The cathodic branch of the polarization curve on Cu displayed similar behaviour at both $[\text{Cl}^-]$. The large E - $\log I$ slopes resulting from the sluggish increase in current density over the wide potential range indicated that the rate of the cathodic reaction was controlled by the rate of O_2 diffusion to the Cu surface.

The location where the Cu cathodic branch intersected the CS anodic branch became further removed from the CS E_{corr} as the Cu area increased. At Cu areas at or beyond 100.7 cm^2 , the intersections occurred in the linear Tafel region of the CS anodic branch and were greater than 100 mV distant from E_{corr} . In the linear Tafel region, cathodic reactions on the CS would have a negligible contribution to the net current on CS. Thus, at Cu:CS area ratios greater than or equal to 100:1, the i_g would have been effectively equal to the total anodic current on CS, and therefore would have accounted for the total CS loss [10]. At lower area ratios where the intersections occur before the linear Tafel region, cathodic activity on the CS may be a significant contributor to the net current on CS, and this residual cathodic activity could drive dissolution of the CS which was unaccounted for in i_g .

The E_g and i_g values determined from the intersection of the anodic branch of the polarization curve on CS and the cathodic branch of the polarization curve on Cu were compared to the values obtained through galvanically coupled experiments, Figure 3.14. The E_g and i_g values predicted by the intersections of the polarization curves followed similar trends to those measured from Cu/CS couples. However, the E_g values determined from the PDP curves tended to be more positive, at an average of +33 mV in 3 M NaCl and +78 mV in 0.1 M NaCl. The PDP curves also tended to

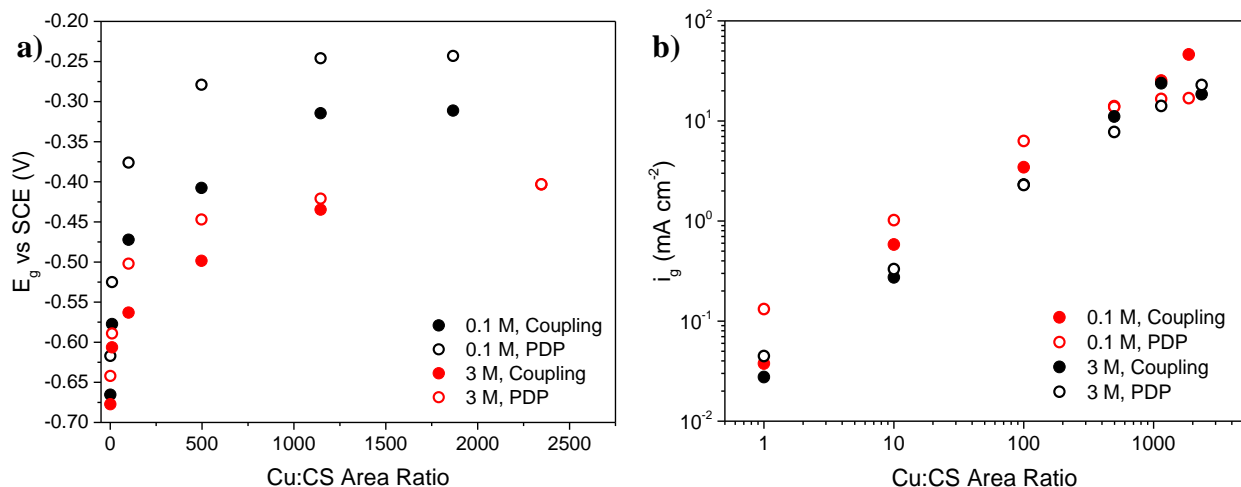


Figure 3.14 a) E_g and b) i_g , determined by PDP and by galvanic coupling experiments, plotted as a function of Cu:CS area ratio in solutions containing $[Cl^-]$ of 0.1 M or 3 M.

slightly overestimate the i_g values at low Cu:CS area ratios and underestimate them at high Cu:CS area ratios. This general overestimation has been found in other work attempting to estimate E_g and i_g using PDP [24].

3.3.4 Effect of Chloride Concentration and Oxygen Availability

Steady state E_g and i_g obtained under air- and Ar-sparged conditions in 3 M NaCl were compared in Figure 3.15. At a 1:1 Cu:CS area ratio, the E_g was 81 mV more negative under Ar-sparged conditions than under air-sparged conditions and similarly on a couple with an area ratio of 100:1,

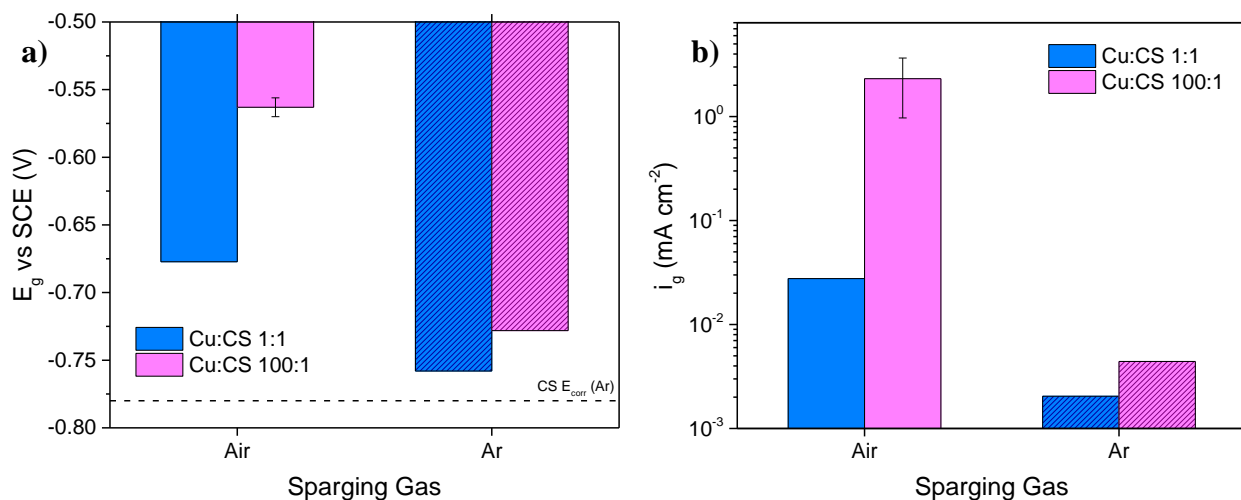


Figure 3.15 Steady-state a) E_g and b) i_g recorded at different Cu:CS area ratios under air-sparged and Ar-sparged conditions in 3 M NaCl.

the E_g was 165 mV more negative. The i_g at both 1:1 and 100:1 Cu:CS area ratios decreased significantly when the experiment was conducted under Ar-sparged conditions, though this decrease was far more significant when the area ratio was 100:1 (by factors of 13.5 and 525 at 1:1 and 100:1 Cu:CS area ratios, respectively). The steady-state i_g values recorded after ~ 40 hours were consistent with very low i_g ($< 0.1 \mu\text{A cm}^{-2}$) recorded on Cu/CS couples over ~ 1500 hours [25]. The non-zero i_g values, and E_g values more positive than the E_{corr} of isolated CS under the same conditions, indicated that the galvanic couple had not been entirely suppressed. Benchtop Ar-sparged experiments typically contain trace O_2 which could be reduced on Cu to drive some small degree of galvanic coupling.

Galvanic coupling experiments were conducted in NaCl solutions with concentrations ranging from 0.001 M to 3 M in order to gain understanding of the effects of Cl^- as they related to O_2 availability and galvanic throwing power. In Figure 3.16, E_g was plotted as a function of $[\text{Cl}^-]$ at several different Cu:CS area ratios, along with the corresponding solution conductivity at each

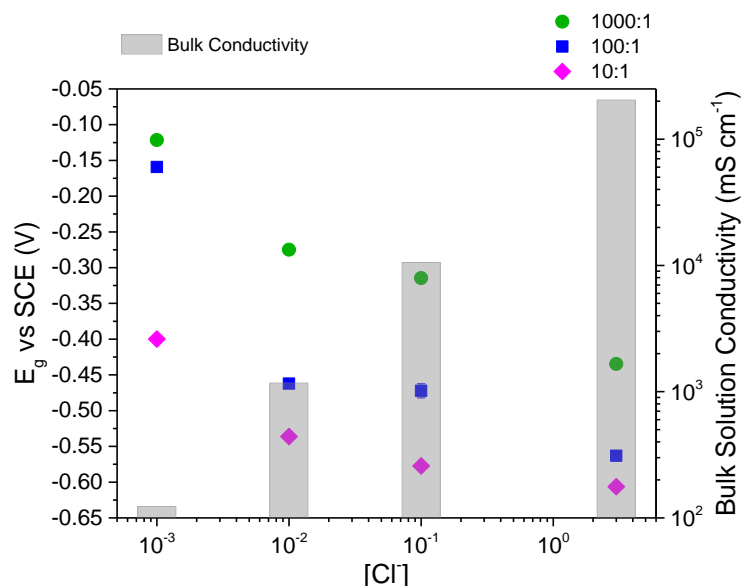


Figure 3.16 Coupled potential, E_g , recorded on CS corroded at different Cu:CS area ratios, plotted as a function of $[\text{Cl}^-]$. Conductivity of the bulk electrolyte, plotted in grey, is also included as a function of $[\text{Cl}^-]$.

concentration, which was calculated from external data [26]. At each Cu:CS area ratio, E_g decreased with increasing $[\text{Cl}^-]$. Across all $[\text{Cl}^-]$, the E_g was most positive at a Cu:CS area ratio of 1000:1 and became more negative as the Cu:CS area ratio decreased.

In Figure 3.17, i_g was plotted as a function of $[\text{Cl}^-]$ along with solution conductivity at each

concentration. At 10:1, 100:1, and 1000:1 Cu:CS area ratios, the i_g initially increased with $[\text{Cl}^-]$ and solution conductivity before decreasing slightly when the $[\text{Cl}^-]$ increased from 0.1 M to 3 M. Notably, the i_g values recorded in 0.001 M $[\text{Cl}^-]$ were comparable across experiments at all Cu:CS area ratios, at 0.30 mA cm⁻², 0.35 mA cm⁻², and 0.91 mA cm⁻² at area ratios of 10:1, 100:1, and 1000:1, respectively. As the $[\text{Cl}^-]$ increased, the i_g values began to diverge as the rate of i_g increase was dependent on the Cu:CS area ratio, with a couple having a 1000:1 Cu:CS area ratio seeing the most rapid escalation of i_g .

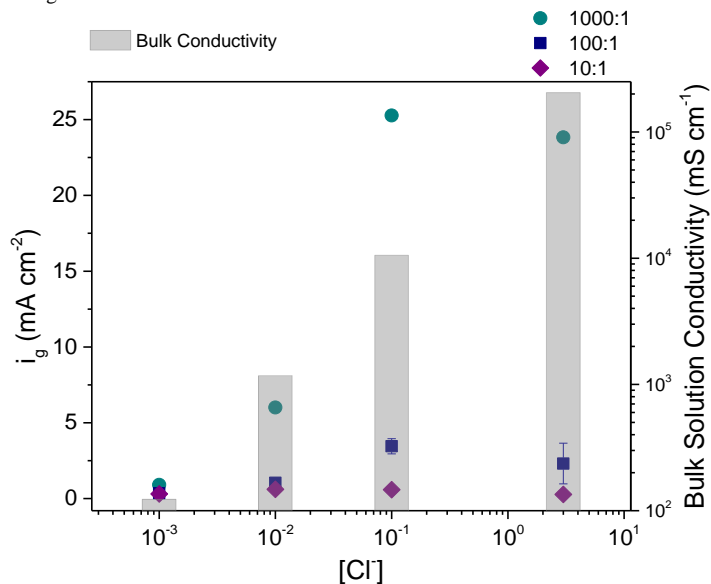


Figure 3.17 Galvanic current, i_g , recorded on CS corroded at different Cu:CS area ratios, plotted as a function of $[\text{Cl}^-]$. Conductivity of the bulk electrolyte, plotted in grey, is also included as a function of $[\text{Cl}^-]$.

SEM micrographs of the CS surface after corrosion in 0.001 M and 0.01 M Cl^- are shown in Figure 3.18. At a Cu:CS area ratio of 10:1, the CS had similar characteristics in both $[\text{Cl}^-]$, where the underlying compact film was non-homogeneously covered by large nodule structures, and finer clusters were distributed atop the other corrosion products. At a Cu:CS area ratio of 100:1, the morphologies of the CS samples at each $[\text{Cl}^-]$ were more distinct from each other, which was consistent with the larger increase in i_g and drop in E_g between 0.001 M and 0.01 M Cl^- . In 0.001 M Cl^- , the underlying film was exposed by ovoid gaps in the upper corrosion layer, which was composed of dense spinous clusters. Small nodule features were found near and below these clusters. In 0.01 M Cl^- , the film was severely cracked and perforated, which could suggest that the film structure was thinner and more brittle than those formed at lower Cu:CS area ratios and in lower $[\text{Cl}^-]$. Some round nodules and clusters were non-homogeneously distributed atop the lower film structure. The compromised structure of the film could have been caused in part by the

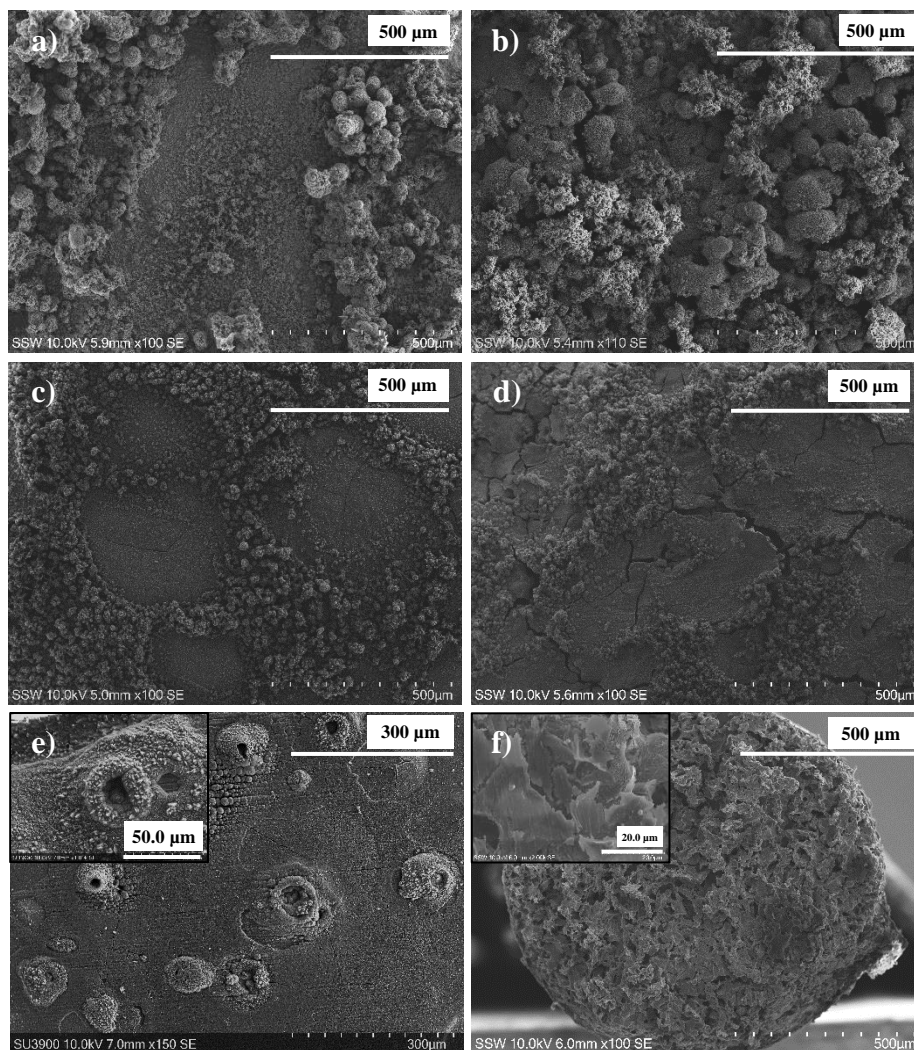


Figure 3.18 Electron images of CS corroded at Cu:CS area ratios of 10:1 (top), 100:1 (middle), and 1000:1 (bottom) in 0.001 M $[\text{Cl}^-]$ (a, c, e) and 0.01 M $[\text{Cl}^-]$ (b, d, f).

increase in Cl^- , which is known to penetrate the otherwise protective film and induce film fracture [27], as well as the decrease in E_g , lowering the favourability of maghemite formation. At a Cu:CS area ratio of 1000:1, the morphology of the CS was vastly different between 0.001 M and 0.01 M Cl^- . In 0.001 M Cl^- , the surface was covered by a thick bilayer film composed of a lower layer whose morphology matched the polished CS surface. The lower film layer was revealed in a small gap in the upper layer (shown in the inset image in Figure 3.16e), which by EDX was found to have an O content of 29.7% by weight, compared to the O content of the surrounding upper film layer being 36.9% by weight. In several areas across the surface, the growth of the film induced sufficient stress to cause fracture and possible delamination of the film in that area. These areas were distinct from cracking caused by exposure to vacuum because they did not exhibit any

shrinkage, but rather cresting and formation of cracked ridges. Additionally, this sample featured several large pits, some of which were surrounded by tall mounds of corrosion product, while others were completely capped by corrosion product. When the $[\text{Cl}^-]$ increased to 0.01 M, the CS surface exhibited extensive damage, consistent with the increased i_g , and only scant evidence of formation of an oxide film, shown in the inset image. The damage on the surface was quite uniform, indicating that the higher conductivity solution allowed for anode mobility on the surface.

An optical image of CS corroded in 0.001 M NaCl coupled to Cu at an area ratio of 100:1, Figure 3.19a, showed a dark film with round nodules underlying dense patches of orange crystals.

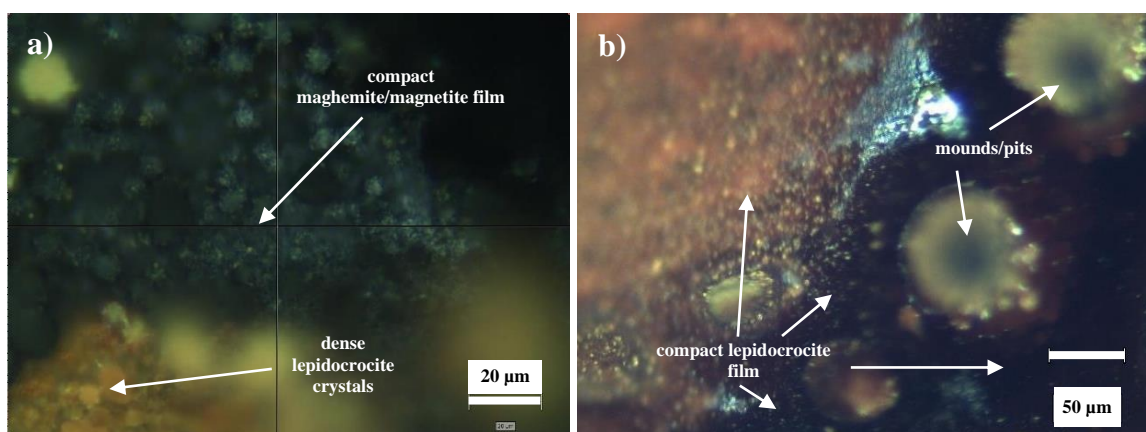


Figure 3.19 Optical images of CS corroded at Cu:CS area ratios of a) 100:1 and b) 1000:1 in 0.001 M $[\text{Cl}^-]$.

Representative Raman spectra, Figure 3.20, collected on CS corroded in low $[\text{Cl}^-]$ showed peaks corresponding to both magnetite and maghemite. Maghemite can be formed from the oxidation of magnetite, but at the high potentials achieved in 0.001 M NaCl, maghemite could have formed directly from Fe on the CS as well [28]. Lepidocrocite was also found on the surface, in the form of both orange clustered crystals and dark maroon films. Trace evidence of green rust was found at pit-like features on the surface, as identified by Raman peaks at 220 cm^{-1} , 433 cm^{-1} , and 510 cm^{-1} , which were characteristic of green rust with Cl^- incorporated into the structure $(\text{Fe}^{\text{II}}_3\text{Fe}^{\text{III}}(\text{OH})_8\text{Cl}\cdot n\text{H}_2\text{O})$ [29-31]. The Raman spectra obtained at low $[\text{Cl}^-]$ tended to have very sharp peaks, suggesting that the corrosion products formed on CS in those experiments were highly crystalline. On CS corroded at a Cu:CS area ratio of 1000:1 (Figure 3.17b), Raman spectra revealed a thick film composed entirely of highly crystalline lepidocrocite. Peaks at 720 cm^{-1} in spectra collected within the pit structures indicated the presence of maghemite, though these signals never indicated pure maghemite, but rather mixed with lepidocrocite signals as well.

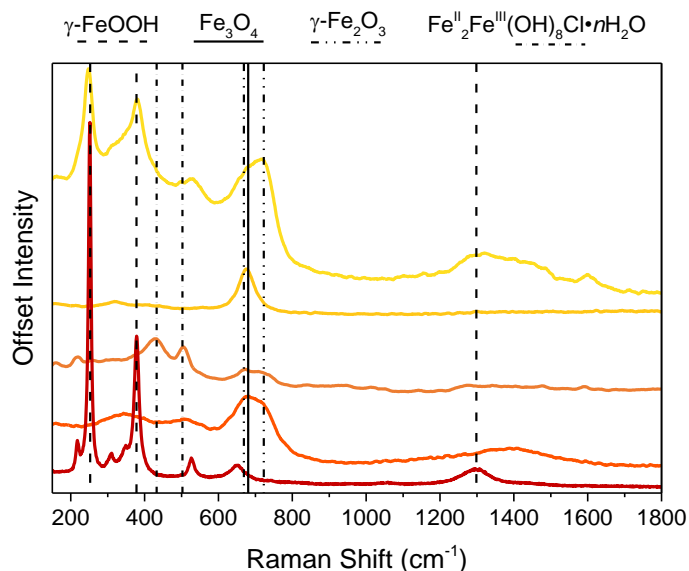
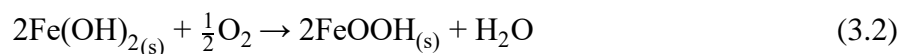
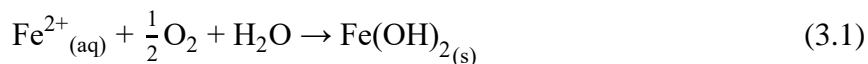


Figure 3.20 Representative Raman spectra recorded on CS at various Cu:CS area ratios in $[\text{Cl}^-] < 0.1 \text{ M}$.

3.4 Discussion

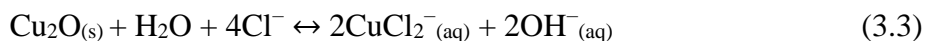
The rate of galvanic corrosion of CS in the Cu/CS galvanic couple was controlled by the rate of O_2 reduction on the Cu surface, as evident in the linear increase in i_g and logarithmic increase in E_g with increasing Cu:CS area ratio [8]. Also, the speed at which the Cu/CS couple established a steady state was entirely dependent on the rate of growth of the oxide layer on the CS. At low Cu:CS area ratio, this oxide grew more slowly and was revealed to have an inner compact layer composed partially of magnetite, an Fe^{III} -deficient species. The porous outer layer was composed largely of lepidocrocite, which would have formed through the conversion of $\text{Fe}(\text{OH})_2$ to the more oxidized, partially dehydrated FeOOH by the following reactions [32]:



The very negative potentials at low Cu:CS area ratios were consistent with the preference for magnetite in the inner layer. As the Cu:CS area ratio increased, so did the E_g , inducing the conversion of magnetite to its more highly oxidized analogue, maghemite. At the highest Cu:CS area ratios, the large i_g led to rapid formation of small-crystal magnetite, which, at the

corresponding E_g values, could be quickly converted to maghemite [33-34] to form a thin mixed-oxide film.

The rate of O_2 reduction on the Cu did not markedly change throughout the duration of the experiments, suggesting that the Cu did not form any insulating film which might block electrochemical reactivity. The freshly polished Cu surface would have had a thin air-formed film of Cu_2O before measurements began, though exposure to Cl^- would have encouraged the dissolution of the Cu_2O through the formation of complexes, as in Reaction 3.3 [35]:



The conversion of Cu_2O to $CuCl_2^-$ is highly dependent on the $[Cl^-]$ and pH, where higher $[Cl^-]$ and lower pH should encourage $CuCl_2^-$ formation. The reduction of O_2 on the Cu surface produced $OH^-_{(aq)}$, but the production of $H^+_{(aq)}$ by the hydrolysis of $Fe^{2+}_{(aq)}$ and $Fe^{3+}_{(aq)}$ prevented an overall increase in pH. This buffering behaviour would have assisted in maintaining the activity of the Cu surface towards O_2 reduction.

In determining the source of Cu observed post-mortem on the CS surface, several pathways were considered: the dissolution of the air-formed Cu_2O film, as stated above, the active corrosion of Cu in the brief period after electrode immersion and before galvanic coupling, the slow corrosion of Cu during the galvanically coupled phase, and enrichment of Cu as an alloying element in the CS itself. Given that the Cu was more plentiful at high Cu:CS area ratios, where the potential at the CS surface (E_g) was very positive, it is unlikely that the reduction of aqueous cuprous or cupric ions originating from corrosion of the Cu electrode was the main source of the Cu observed on CS.

The alloyed Cu present in the CS, which is more noble than the Fe matrix and thus would be selectively retained and enriched at the surface, can account for most, if not all, of the Cu observed on CS. Such enrichment has been reported in other studies [36-38]. This process occurred to a greater extent at higher Cu:CS area ratios, when dissolution of the Fe matrix was most rapid. In order to investigate the contribution of Cu in the CS, a CS sample was polarized according to the E_g vs. time profile previously recorded under aggressive conditions (high Cu:CS, high $[Cl^-]$), Figure 3.21. Areas 1 and 2 in Figure 3.21 have Cu contents of 12.3% and 17.0% by weight, respectively. Areas 3, 4, and 5 have slightly less Cu, at 5.3%, 2.6%, and 3.8% by weight,

respectively. This is consistent with the Cu contents found at the surfaces of the most aggressively corroded CS samples, which tended to range from 1% to 19% Cu by weight. Additionally, the Cu was always observed under the oxide, collocated with bare steel, further indicating the enrichment of Cu in the CS itself.

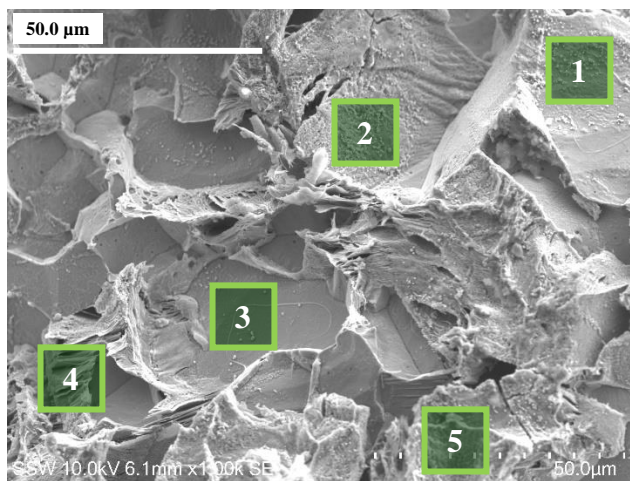


Figure 3.21 SEM micrograph of CS polarized without Cu, according to the E_g vs. time profile of a Cu:CS area ratio of 2500:1 in 3 M NaCl. Green numbered boxes indicate areas where EDX spectra were taken.

Trends in PDP data were generally consistent with galvanic coupling experiments, but the PDP estimated the i_g and E_g poorly, typically by overestimation. Previous efforts to use potentiodynamic techniques to predict E_g and i_g have brought about similar results and recommended increased exposure time before polarization and slower scan rate to better approximate a steady state surface [24].

The total anodic current, i_A , on the CS reflects the CS corrosion rate. At Cu:CS area ratios greater than 100:1, the E_g was sufficiently far-removed from the E_{corr} of CS to reasonably assume that the i_g was approximately equal to the total i_A on CS and could therefore be used to estimate the corrosion rate [10]. At lower Cu:CS area ratios, there was likely appreciable dissolution of the CS that was not accounted for in the i_g due to residual cathodic activity on the surface. Thus, the i_g would represent an underestimate of the corrosion rate of the CS. The E_g , however, cannot necessarily predict whether i_g can approximate i_A , particularly in the case of low-conductivity solutions. The E_g of the system was not only sensitive to the Cu:CS area ratio, but also the O_2 availability, as demonstrated in the very low E_g in Ar-sparged solutions and the downward trend in E_g with increasing $[Cl^-]$. The solubility of O_2 increased with decreasing salt concentration in

accordance with the Setschenow equation [2, 39], which is shown in its linear form in Equation 3.1:

$$\log S_{O_2} = -k_m C_m + \log S_{O_2}^0 \quad (3.2)$$

where S_{O_2} is the O_2 solubility in electrolyte “ m ” with a salt concentration of C_m in M, k_m is the Setschenow salt parameter [2], and $S_{O_2}^0$ is the solubility of O_2 in pure water. In this work, the O_2 solubility was calculated to increase from 1.0×10^{-4} M to 2.7×10^{-4} M as the $[Cl^-]$ ranged from 3 M to 0.001 M. The increased availability of O_2 in lower $[Cl^-]$ solutions, where the surface O_2 concentration was proportional to the higher bulk O_2 concentration [28], caused the positive shift in E_g . While more positive E_g was associated with larger i_g in 0.1 M and 3 M NaCl, the further positive shift in E_g at 0.01 M and 0.001 M Cl^- was associated with marked decreases in i_g . The presence of open and capped pits on the CS surface after corrosion in 0.001 M Cl^- at a Cu:CS area ratio of 1000:1 was indicative of passivation of the CS surface by the oxide film [40], which was possible at the highly oxidizing potentials observed in low $[Cl^-]$. This passivity likely contributed to the observed decrease in i_g from 0.01 M Cl^- to 0.001 M Cl^- . However, such passivity was not achieved on CS in 0.01 M Cl^- , as evident the fractured film, lack of distinct pitting, and more negative E_g observed at all Cu:CS area ratios tested. This suggests that the decrease in i_g from 0.1 M to 0.01 M Cl^- was caused primarily by the constriction of galvanic throwing power and that the effective Cu:CS area ratio was less than the geometric Cu:CS area ratio. The galvanic throwing power would necessarily be reduced further in the 0.001 M Cl^- solution, though the relative effects of passivation and galvanic throwing power constriction in 0.001 M Cl^- have not yet been deconvoluted. True quantification of the effective area ratio, and thus separation of the effects of passivation, would be well-served by mapping potential and current profiles across the CS and Cu, which was not attempted in this work.

3.5 Conclusions

This work investigated the Cu/CS galvanic couple over a wide range of Cu:CS area ratios and $[Cl^-]$ for the use of Cu-coated CS in the disposal of used nuclear fuel. It was determined that:

- The logarithmic increase in E_g and linear increase in i_g over the range of Cu:CS area ratios suggests that O_2 reduction on Cu was rate-limiting, though at small Cu:CS area ratios, some share of the O_2 reduction was occurring on the CS as well.

- PDP curves for Cu and CS suggest that at E_g , CS was actively dissolving and O_2 reduction on Cu was limited by mass transport, such that i_g was equal to the limiting current for O_2 reduction. At high Cu:CS area ratios ($>100:1$), E_g and i_g were found in the CS Tafel region.
- PDP can provide only a rough approximation of E_g and i_g values due to error inherent in the very popular technique, i.e. lack of a steady-state surface and possible issues with iR drop through solution. The trends of E_g and i_g , however were reasonably well predicted by the PDP data.
- The CS surface developed a corrosion film whose composition and morphology were dependent on Cu:CS area ratio. As the area ratio increased, more maghemite was incorporated in the compact film and lepidocrocite deposits became smaller and sparser. The change in composition and morphology was associated with more positive E_g and more rapid establishment of the steady state.
- In low conductivity solution, galvanic throwing power was constricted, such that the effective Cu:CS area ratio was smaller than the geometric area ratio of the Cu and CS electrodes, even though the E_g was significantly polarized in the positive direction due to greater O_2 availability.
- In addition to the constriction of galvanic throwing power in 0.001 M Cl^- , passivation of the CS surface may have contributed to a drop in i_g . The relative strength of each effect is yet unknown.

In the scenario of a through-coating defect in the Cu-coated CS used nuclear fuel container, predicting the extent of galvanic corrosion of the CS vessel requires knowledge of the O_2 availability, which will be finite in the DGR, and electrolyte conductivity, because that will define the effective Cu:CS area ratio. In the DGR, the container will be surrounded by a bentonite clay buffer box, which would act as a barrier for transport of O_2 and may introduce a resistance which could impede the coupling of Cu and CS.

3.6 References

1. F. King, D. S. Hall, P.G. Keech, *Corros. Eng. Sci. Techn.* **2017**, *52*, 25-30.
2. S. L. Clegg, P. Brimblecombe, *Geochim. Cosmochim. Acta* **1990**, *54*, 14.
3. H. Ackerman, et al., *Corrosion*. ASM International: USA, 1992; Vol. 13.
4. T. Standish, J. Chen, R. Jacklin, P. Jakupi, S. Ramamurthy, D. Zagidulin, P. Keech, D. Shoesmith, *Electrochim. Acta* **2016**, *211*, 12.
5. T. Standish, D. Zagidulin, S. Ramamurthy, P. Keech, D. Shoesmith, J. Noël, *Geosciences* **2018**, *8*, 1-14.
6. T. E. Standish, D. Zagidulin, S. Ramamurthy, P. G. Keech, J. J. Noël, D. W. Shoesmith, *Corros. Eng. Sci. Techn.* **2017**, *52*, 65-69.
7. T. E. Standish, L. J. Braithwaite, D. W. Shoesmith, J. J. Noël, *J. Electrochem. Soc.* **2019**, *166*, C1-C8.
8. F. Mansfeld, *Corrosion* **1971**, *27*, 436-442.
9. M. Stern, A. L. Geary, *J. Electrochem. Soc.* **1957**, *104*, 56-63.
10. F. Mansfeld, *Corrosion* **1973**, *29*, 403-405.
11. J. M. Ali, Q. M. Abbas, *Al-Khwarizmi Engineering Journal* **2009**, *5*, 60-71.
12. Z. Wang, Y. Wang, C. Wang, *IOP Conf. Ser.: Mater. Sci. Eng.* **2018**, *322*.
13. B. Tsujino, S. Miyase, *Corrosion* **1982**, *38*.
14. D. L. A. de Faria, S. Venancio Silva, M. T. de Oliveira, *J. Raman Spectrosc.* **1997**, *28*, 873-878.
15. I. Chamritski, G. Burns, *J. Phys. Chem. B* **2004**, *109*, 4965-4968.
16. M. K. Niewoudt, J. D. Comins, I. Cukrowski, *J. Raman Spectrosc.* **2011**, *42*, 1335-1339.
17. A. Liu, J. Liu, B. Pan, W. Zhang, *RSC Adv.* **2014**, *4* (101), 57377-57382.
18. M. Hanesch, *Geophys. J. Int.* **2009**, *177* (3), 941-948.
19. X. Bi, B. Ganguly, G. P. Huffman, F. E. Huggins, M. Endo, P. C. Eklund, *J. Mater. Res. Technol.* **1993**, *8*, 1666-1674.
20. C. T. Lee, Z. Qin, M. Odziemkowski, D. W. Shoesmith, *J. Electrochem. Soc.* **2006**, *153*, B33-B41.
21. A. Pepe, P. Galliano, M. Aparicio, A. Durán, S. Ceré, *Surf. Coat. Technol.* **2006**, *200* (11), 3486-3491.
22. S. Li, L. Hihara, *J. of the Electrochem. Soc.* **2012**, *159*, C461-C468.

23. L. Li, Q. Qu, W. Bai, Y. Chen, S. Zhang, G. Gao, Z. Ding, *Int. J. Electrochem. Sci.* **2012**, *7*, 3773-3786.
24. H. P. Hack, J. R. Scully, *Corrosion* **1986**, *42*, 79-90.
25. N. R. Smart, B. Reddy, A. P. Rance, D. J. Nixon, N. Diomidis, *Corros. Eng. Sci. Techn.* **2017**, *52*, 113-126.
26. Conductivity Ordering Guide. EcoStruxure Process Instrumentation (formerly Foxboro): Massachusetts, USA, 1999.
27. Y. Xia, F. Cao, W. Liu, L. Chang, J. Zhang, *Int. J. Electrochem. Sci.* **2013**, *8*, 3057-3073.
28. E. McCafferty, *Introduction to Corrosion Science*. Springer: New York, USA, 2010.
29. S. Simard, M. Odziemkowski, D. E. Irish, L. Brossard, H. Ménard, *J. of Appl. Electrochem.* **2001**, *31*, 913-920.
30. N. Boucherit, A. Hugot-Le Goff, S. Joiret, *Corros. Sci.* **1991**, *32* (5), 497-507.
31. Ph. Refait, M. Abdelmoula, J.-M. R. Génin, *Corros. Sci.* **1998**, *40*, 1547-1560.
32. K. Xiao, C. Dong, X. Li, F. Wang, *J. Iron. Steel Res. Int.* **2008**, *15*, 42-48.
33. K. Daub, X. Zhang, L. Wang, Z. Qin, J. J. Noël, J. C. Wren, *Electrochim. Acta* **2011**, *56*, 6661-6672.
34. R. M. Cornell, U. Schwertmann, *The Iron Oxides: Structure, Properties, Reactions, Occurrences and Uses*. 2nd ed.; WILEY-VCH Verlag GmbH & Co. KGaA: Weinheim, Germany, 2003.
35. G. Kear, B. D. Barker, F. C. Walsh, *Corros. Sci.* **2004**, *46*, 109-135.
36. W-H. Huang, H-W. Yen, Y-L. Lee, *J. Mater. Res. Technol.* **2019**, *8*, 1476-1485.
37. J. H. Hong, S. H. Lee, J. G. Kim, J. B. Yoon, *Corros. Sci.* **2012**, *54*, 174-182.
38. J-K. Kim, A. Nishikata, T. Tsuru, *Mater. Trans.* **2003**, *44*, 396-400.
39. M. Randall, C. F. Failey, *Chem. Rev.* **1927**, *4* (3), 271-284.
40. L. Cáceres, T. Vargas, L. Herrera, *Corros. Sci.* **2009**, *51*, 971-978.

4. Galvanic Coupling of Copper and Carbon Steel in the Presence of Bentonite Clay and Chloride

4.1 Introduction

The Canadian design of a DGR for long-term containment of used nuclear fuel consists of multiple barriers to isolate harmful radionuclides from the environment. The used CANDU (Canada Deuterium Uranium) fuel bundles will be housed in Cu-coated CS containers where the steel provides the necessary structural integrity for the container while the 3 mm Cu coating provides corrosion protection. Each container will be surrounded by a compacted bentonite clay buffer box and stored in an emplacement room in the host rock, with all gaps to be filled with bentonite clay backfill material [1]. The compacted bentonite clay provides immediate protection during emplacement of the container and, along with the gap-fill, long-term protection by limiting transport of groundwater and corrosive species to and transport of radionuclides from the container surface [2]. Previous work has summarized the expected evolution of conditions within the DGR up to 10^6 years after closure [3]. Moisture will initially be driven from the container surface by heat, as temperatures are expected to climb to 83 °C after 45 years and remain around 80 °C until 1,550 years after placement [4]. As the repository temperature decreases, liquid groundwater will be reintroduced and slowly saturate the bentonite clay. The O₂ available to sustain corrosion of the container will be limited to the inventory trapped in the DGR upon closure, and will be consumed over time by microbial activity, oxidation processes in the bentonite clay, and slow corrosion of the Cu coating. The composition of the groundwater will be dependent on the host rock and is expected to contain between 0.1 M and 5 M Cl⁻, with higher Cl⁻ concentrations expected in sedimentary host rock.

In order to predict the long-term corrosion performance of the UFC under DGR conditions, it is vital to assess all scenarios which could represent failure pathways of the UFC. In this work, we have investigated the possible consequences of a container being placed in the DGR with a defect through the Cu coating, exposing some steel at the base of the defect. Given the thorough non-destructive examination of the coating before placement in the repository, such a scenario is unlikely, however, if a defect is sufficiently small to evade detection, or if a defect is introduced in the coating after the final inspection and before placement, then it is important to understand

how such a defect may affect the lifetime of the container. In such a case, galvanic coupling of the Cu coating and steel vessel could be possible. Due to the large available Cu surface area to act as a preferential cathode and comparatively minuscule area of exposed carbon steel acting as a preferential anode, corrosion of the steel vessel could be rapid, leading to local penetration of the container and/or delamination of the coating. Previous work has investigated the galvanic corrosion of carbon steel coupled to Cu at defects in cold spray and electrodeposited Cu coatings on carbon steel under O₂-sparged [5-6] and de-aerated conditions [7] in NaCl solutions. Additionally, the importance of defect size as it related to Cu-to-CS area ratio was investigated in aerated and de-aerated NaCl solution [8]. These studies established that the Cu/CS galvanic couple was highly sensitive to O₂ availability and Cl⁻ concentration, and that large Cu-to-CS area ratios (>100:1), abundant Cl⁻, and abundant O₂ resulted in aggressive corrosion of the CS. Some work has been done to investigate the effect of bentonite on the galvanic coupling of several materials relevant to the Swiss [9] and Czech [10] used fuel disposal designs. There remains, however, limited research on the effect of bentonite clay on the galvanic corrosion of CS coupled to Cu.

The swelling properties of bentonite clay, which originate from its layered montmorillonite structure, not only serve to cushion and stabilize the UFC but also dramatically slow the ingress of groundwater by the uptake of H₂O molecules into the interlayer space [2]. The extremely low hydraulic conductivity of compacted bentonite clay limits the transport of corrosive species such as O₂ to the container surface, in addition to slowing the transport of species away from the container [11]. The chemistry at the bentonite-UFC interface would also be profoundly affected by the exchange of cations into and out of the interlayer space and the ionization of surface -OH groups [12]. Exposure of compacted bentonite to ionizing radiation has been shown to affect its redox conditions, sedimentation behaviour, and radionuclide sorption ability [13], all of which affect the clay environment near the container surface, though effects of radiation are outside the scope of this work. Corrosion of various test coupons in slurries of bentonite clay has been reported in previous work [9, 14-15], and those studies have shown that the bentonite clay can have a profound impact on corrosion even when hydraulic conductivity remains high.

In the present work, we have investigated the corrosion behaviour of CS that was galvanically coupled to Cu in the absence and presence of Na-based bentonite clay saturated with 1M NaCl solution under naturally aerated and de-aerated conditions. Layers of bentonite slurry tuned to

various thickness were made to obstruct galvanically coupled Cu and CS specimens in order to determine how, and the degree to which, clay suppresses galvanic corrosion, separate from its swelling pressure and low hydraulic conductivity.

4.2 Experimental Methods

4.2.1 Sample Preparation

The cylindrical CS samples were cut from a block of A516 gr. 70 carbon steel, provided by NWMO (Toronto, Canada) and the Cu ring samples were cut from P-doped O-free wrought Cu provided by SKB (Stockholm, Sweden). The samples were ground with SiC paper up to a p1200 finish and sonicated in methanol. Steel and Cu wires were fitted with PTFE heat-shrink tubing and, with a Pb/Sn solder formula, soldered by one end to the CS and Cu samples, respectively, leaving the opposite ends of the wires exposed for electrical connection; these electrodes were then sonicated in methanol. The Cu electrodes were mounted in Hysol epoxy resin (Henkel AG & Co., Düsseldorf, Germany) so that the epoxy extended at least 0.9 cm from the outer edge and ~0.08 cm inwards from the inner edge of the Cu ring. The CS electrodes were also mounted in epoxy resin so that the outer diameter of the epoxy fit tightly into the inner void of the mounted Cu ring. The epoxy was purged of air bubbles under vacuum and set to cure at room temperature for 24 hours. Once mounted, the areas of the exposed faces of the CS electrodes ranged from 0.01 cm² to 0.12 cm² and the faces of the Cu electrodes ranged from 1.26 cm² to 9.50 cm². Before each experiment, the top faces of the electrodes were ground to a p2500 finish, sonicated in methanol, and rinsed with ultrapure water (resistivity of 18.2 MΩ cm) from a Thermo Scientific Barnstead Nanopure water purification system.

4.2.2 Galvanic Coupling Experiments

Naturally aerated experiments were conducted in a single compartment cell with a volume of 1 L, Figure 4.1. The Cu and CS electrodes were fit together so that they formed a flush surface and were situated at the centre of the cell at a known depth, facing upwards. The Cu:CS area ratios ranged from 10:1 to 1000:1. The CS and Cu were electrically insulated from each other in solution but externally coupled through a Keithley 6514 Electrometer acting as a ZRA so that I_g could be recorded. E_g was recorded in reference to an SCE, which was housed in a glass sheath with a dense glass frit. Experiments were conducted in 800 mL solutions of 1 M reagent grade NaCl (Fisher

Scientific) in ultrapure water. The Na-based bentonite clay, MX-80 Wyoming bentonite, supplied by American Colloid Co., had an initial moisture content of 20% and was added to the cell in the amounts of 10 g L^{-1} , 50 g L^{-1} , 100 g L^{-1} , 150 g L^{-1} , or 250 g L^{-1} . Upon addition of the bentonite to the cell, the mixture was briefly stirred to produce a homogeneous suspension, then the bentonite was allowed to passively settle atop the electrode surfaces, producing layers of slurry measuring 1 mm, 5 mm, 9 mm, 12 mm, or 20 mm thick, respectively. E_g and I_g were recorded until both reached steady state – about 24 hours.

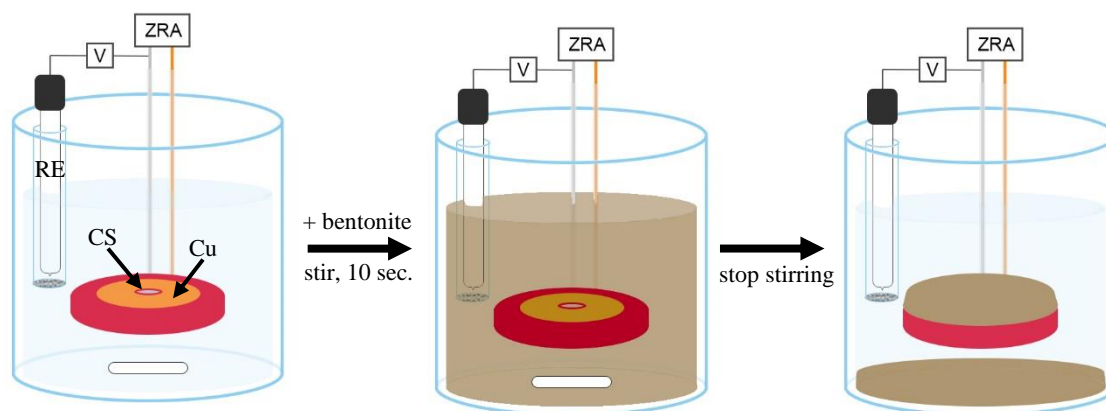


Figure 4.1 Schematic diagram of experimental setup for galvanically coupled experiments in the presence of bentonite.

De-aerated experiments in the absence of bentonite were performed in a three-compartment electrochemical cell which was constantly sparged with Ar gas (PRAXAIR). De-aerated experiments in the presence of bentonite were also sparged continuously with Ar-gas and were performed in the same cell as the naturally aerated experiments; great care was taken to seal the cell with laboratory film to minimize ingress of O_2 while still allowing for Ar outgassing.

4.2.3 EIS Experiments

In order to perform EIS measurements on the Cu and CS individually, in-lab software (built by Dmitriy Zagidulin) interfacing with a Keithley 2450 Sourcemeter was used to dynamically polarize the working electrode (either CS or Cu) according to E_g vs. time data obtained from previous galvanic coupling experiments in 0 g L^{-1} , 10 g L^{-1} , 50 g L^{-1} , 100 g L^{-1} , 150 g L^{-1} , and 250 g L^{-1} bentonite-containing 1 M NaCl solutions. Following the dynamic polarization, the working electrode was held at the experimentally determined steady-state E_g for 15 minutes using a 1287 Solartron potentiostat before performing EIS measurements using a Solartron 1255E Frequency

Response Analyzer. EIS measurements were performed from a DC voltage equal to the steady state E_g , with a signal frequency ranging from 10^5 Hz to 5×10^{-3} Hz or 10^{-3} Hz for CS or Cu, respectively, and an amplitude of 10 mV, taking 11 data points per decade of frequency change.

4.2.4 Surface Analysis

Raman spectra and optical micrographs were collected on CS samples after corrosion using a Renishaw inVia Reflex Raman Spectrometer. Raman data were collected with a 633 nm HeNe laser and an 1800 l mm^{-1} grating for point spectra or a 1200 l mm^{-1} grating for maps. SEM/EDX was performed following Raman spectroscopy using a Hitachi SU3500 Variable Pressure SEM with Oxford AZtec X-Max50 SSD X-ray analyzer or a Hitachi SU3900 Variable Pressure Large Chamber SEM with an Oxford ULTIM MAX 65 SSD X-ray analyzer. All surface analysis was conducted at Surface Science Western (London, Canada).

4.3 Results

4.3.1 Copper-to-Steel Area Ratio Effects in the Presence and Absence of Bentonite

Steady-state E_g and i_g were established in all experiments after between 18 and 26 hours of immersion. The measured I_g , the galvanic current, was converted to galvanic current density on CS, i_g , by division of I_g by the exposed CS surface area. The reported E_g and i_g values were obtained by taking an average of the data over the final hour of each experiment. Figure 4.2a shows that E_g recorded both in the absence of bentonite and in the presence of a 5 mm layer of bentonite slurry exhibited the same upward trend with increasing Cu:CS area ratio. Under both conditions, the increase in E_g was initially rapid, but became more gradual as the Cu:CS area ratio increased. In the absence of bentonite, between Cu:CS area ratios of 10:1 and 200:1, the E_g increased by ~ 80 mV, and increased only a further ~ 110 mV between area ratios of 200:1 and 1000:1. When the electrodes were occluded by a 5 mm layer of bentonite, the increase in E_g between area ratios of 10:1 and 200:1 was slightly less pronounced at ~ 63 mV, and the increase between area ratios of 200:1 and 1000:1 was also smaller at ~ 66 mV than under bentonite-free conditions. This suggests that the sensitivity of E_g to the Cu:CS area ratio was somewhat diminished in the presence of bentonite slurry. Notably, in the presence of a 5 mm layer of bentonite slurry the E_g values were shifted negatively by at least ~ 68 mV, up to ~ 129 mV at the highest Cu:CS area ratio of 1000:1. The i_g values, Figure 4.2b, increased linearly with increasing Cu:CS area ratio in the presence and

absence of bentonite. The linear dependence of i_g on relative Cu area is consistent with O_2 reduction on Cu being rate-controlling with respect to the galvanic current. At most Cu:CS area ratios, the i_g was over $10\times$ greater in the absence of bentonite, except for 200:1 Cu:CS, which showed an i_g that was $5\times$ greater when no bentonite was present.

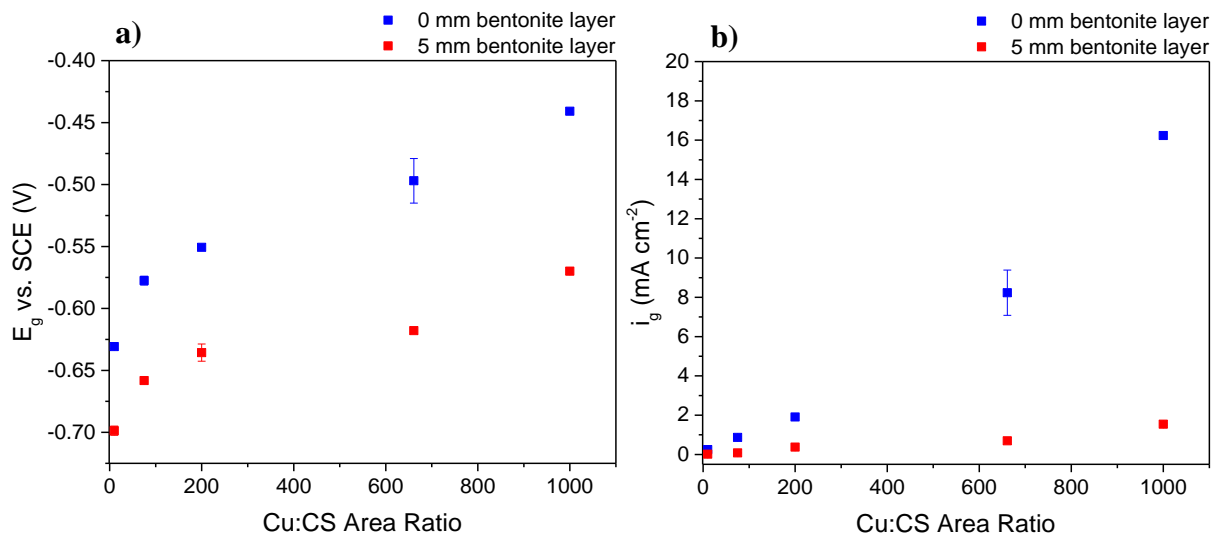


Figure 4.2 a) E_g and b) i_g on CS plotted as a function of Cu:CS area ratio in 1 M NaCl solution with bentonite absent and with the electrodes occluded by a 5 mm bentonite slurry layer.

4.3.2 Effects of Bentonite Layer Thickness

The thickness of the bentonite slurry layer was tuned by adding specific amounts of bentonite clay to the cell and stirring just enough to produce a homogeneous, and therefore repeatable, suspension. The suspension settled onto the mounted electrode arrangement, which had a fixed total surface area regardless of the relative areas of the Cu and CS and was situated at a known depth within the cell. In Figure 4.3a-b, The E_g and i_g were plotted as a function of the thickness of the bentonite layer which formed after ~ 24 hours. With the formation of only a 1 mm layer of slurry, E_g at 10:1, 75:1, and 200:1 Cu:CS area ratios dropped by 66 mV, 62 mV, and 25 mV, respectively. Increasing the layer thickness to 5 mm produced 18 mV, 23 mV, and 60 mV drops in E_g when the Cu:CS area ratio was 10:1, 75:1, and 200:1, respectively. In bentonite layers between 5 mm and 20 mm thick, the E_g only dropped by a total of 24 mV, 7 mV, and 10 mV when the Cu:CS area ratio was 10:1, 75:1, and 200:1, respectively.

The potential achieved at 20 mm of bentonite coverage remained 26 mV to 41 mV more positive than the E_g of the Cu/CS galvanic couples in de-aerated 1 M NaCl at the same area ratios,

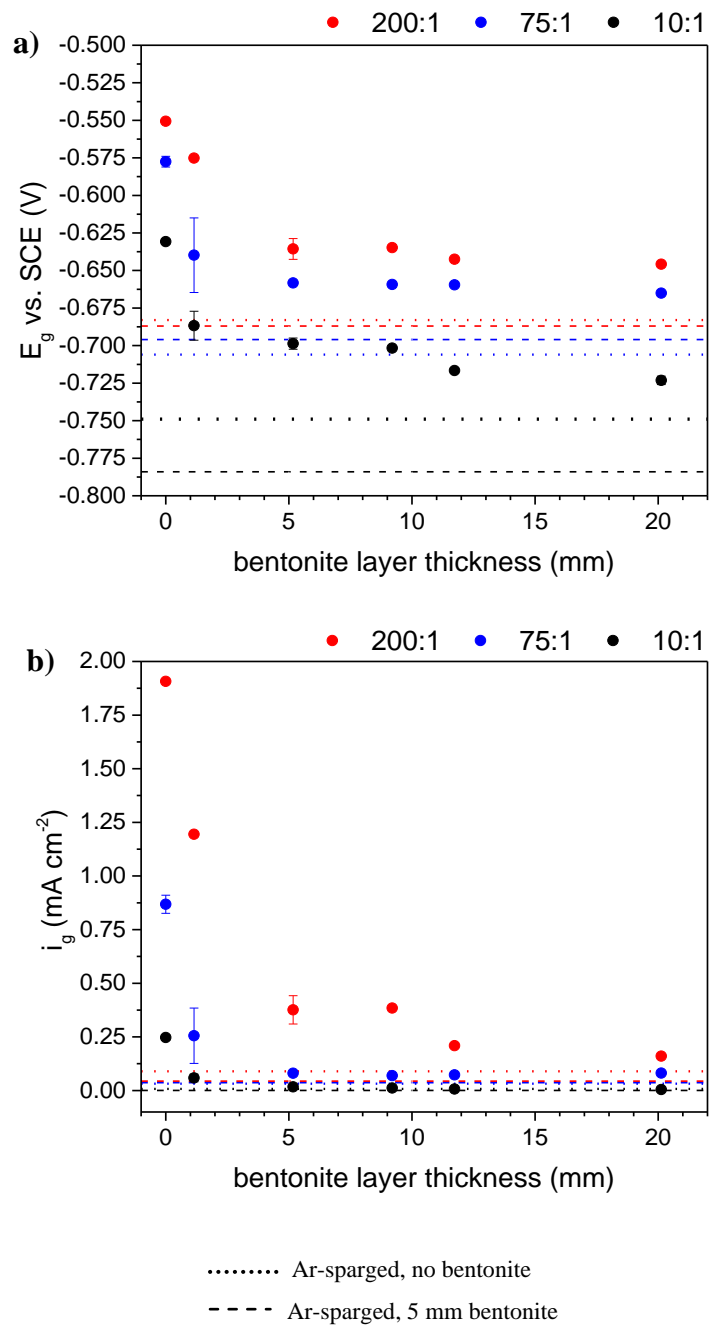


Figure 4.3 a) E_g and b) i_g on steel plotted as a function of bentonite slurry layer thickness at Cu:CS area ratios of 10:1, 75:1 and 200:1. Horizontal dashed and dotted lines correspond to steady-state values collected under Ar-sparged conditions at the Cu:CS area ratios indicated by the colour.

indicating a failure to achieve near-anoxic conditions within the bentonite clay layer. Cu/CS couples corroded under Ar-sparged conditions in the presence of bentonite exhibited steady-state E_g and i_g values even lower than those achieved in Ar-sparged solution in the absence of bentonite, with the exception of when the Cu:CS area ratio was 75:1, when the E_g was only 10 mV more

positive and i_g only 0.005 mA cm^{-2} greater in the presence of bentonite; such an effect was likely due to the ingress of a small amount of O_2 , which was more likely to occur in the single-compartment cell than in the three-compartment cell.

The evolution of E_g over time, Figure 4.4, was starkly different when bentonite was present than when it was absent. Under bentonite-free conditions, the E_g and i_g exhibited oscillatory behaviour over the course of the test. The i_g profiles matched the oscillatory pattern of the E_g profiles, suggesting that this oscillation is borne from the reactivity on the Cu electrode. When bentonite was present, the E_g profile was extremely smooth and did not exhibit such oscillations; this dampening of the transient behaviour in the presence of bentonite indicates that the events were caused by changes in O_2 flux to the Cu surface. The rapid fall in E_g and i_g in the presence of bentonite was the result of consumption of O_2 initially contained in the clay and electrolyte and was followed by a slight increase before achievement of steady-state – the result of the reintroduction of O_2 by diffusion.

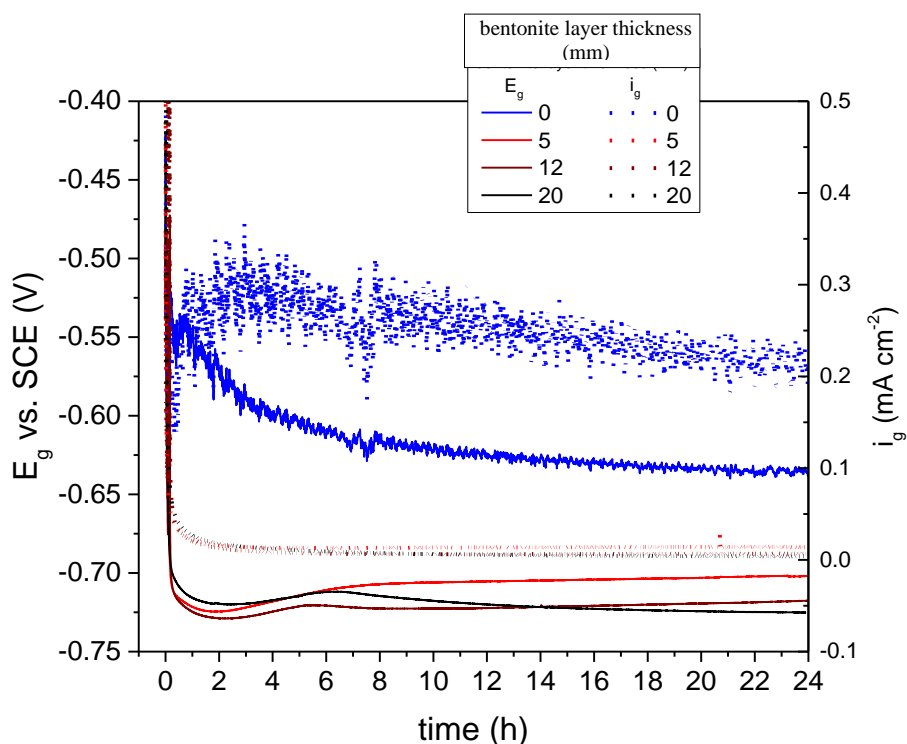


Figure 4.4 E_g and i_g plotted as a function of time for the Cu/CS galvanic couple at an area ratio of 10:1 in 1 M NaCl and varying amounts of bentonite clay.

4.3.3 Surface Analysis of Carbon Steel

SEM images of the CS surface after corrosion in the absence of bentonite slurry, Figure 4.5, revealed a compact oxide film underlying a uniform distribution of fine spinous clusters and hexagonal plates. Across the centre of the sample, the morphology of the underlying film followed a subtle pattern of parallel lines caused by the surface preparation of the sample before the experiment, suggesting that the film was quite thin and formed rapidly. The outer edges of the sample were also covered in a compact film but exhibited a pattern of etched CS grains 50 μm to 100 μm across [16], and any parallel grinding lines were much more difficult to discern.

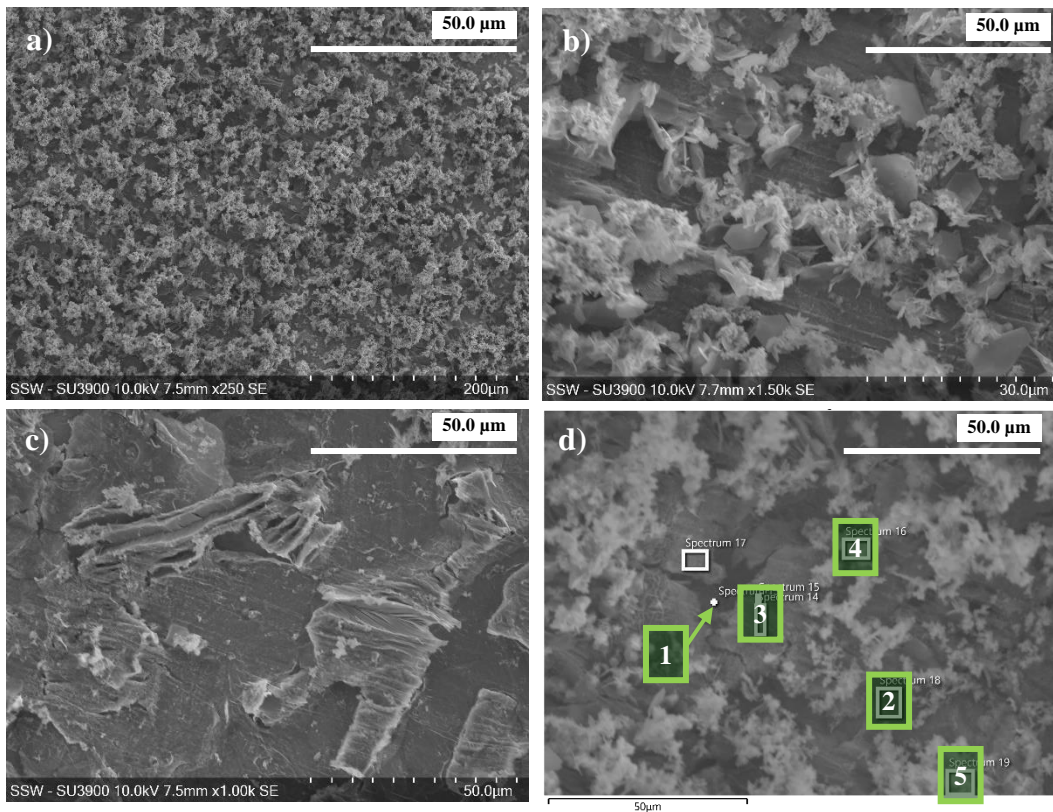


Figure 4.5 a-c) SEM images of CS corroded at a Cu:CS area ratio of 10:1 in 1 M NaCl solution without bentonite slurry, and d) SEM image with numbers 1 to 5 indicating notable locations where EDX spectra were collected.

Small perforations were observed throughout the film, as in Figure 4.5d, area 1, and were found to penetrate the entire thickness of the film, revealing bare steel (91.7% Fe by weight) below. Such film ruptures were consistent with Cl^- -initiated pitting, as oxide films formed in neutral 1 M NaCl solution have been shown to suffer local breakdown and are known to be non-protective [17]. The cluster deposits and hexagonal plates were generally found around the perforations in the film.

EDX analysis in Figure 4.5d showed the oxide film, areas 2 and 3, to be composed of between 4.3% and 10.8% O by weight, which could be indicative of O-deficiency in the film, but was more likely an indicator that the film was thin and non-uniform. X-ray information can be gathered from as deep as 10 μm [18], so a thin film would result in greater signals for Fe, Mn, Cu, and other elements associated with the base alloy, and lesser signals for O, as was seen here. The clustered deposits, Figure 4.5d, areas 4 and 5, were composed of O-rich oxides, containing between 34.2% and 35.9% O by weight.

As in Chapter 3 of this thesis, Cu was found in substantial amounts at the CS surface. EDX maps in Figure 4.6 show the collocation of bare CS and enriched Cu, consistent with the conclusion that the alloyed Cu was selectively retained as the CS corroded.

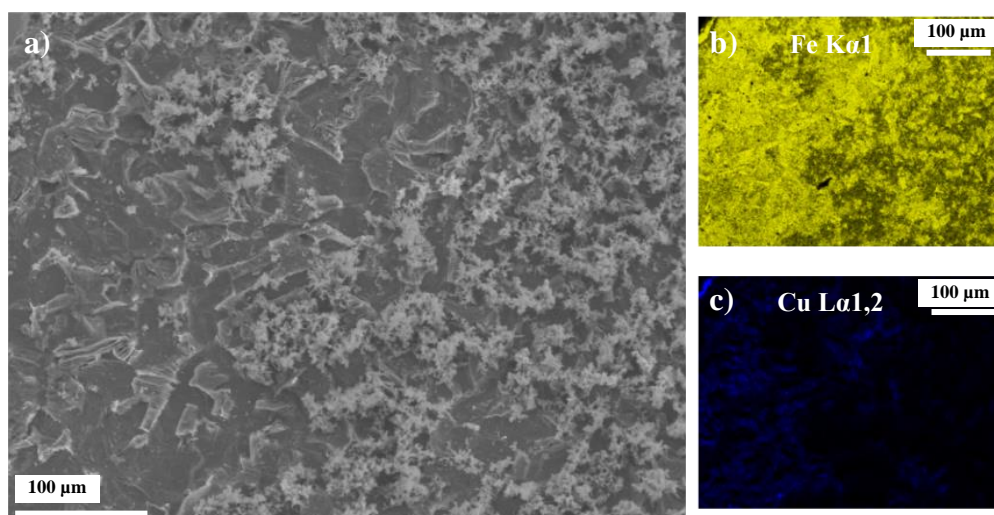


Figure 4.6 a) SEM image of CS corroded at a Cu:CS area ratio of 10:1 in 1 M NaCl without bentonite and area maps of the b) Fe, and c) Cu signals.

Raman spectroscopy, Figure 4.7, revealed a complex mixture of Fe-oxides and oxyhydroxides formed in the absence of bentonite. Goethite, which has a strong peak centred at 385 cm^{-1} , was found to be mixed with poorly crystalline maghemite, magnetite, and possibly other species such as ferrihydrite ($\text{Fe}_{10}\text{O}_{14}(\text{OH})_2$) [19] or feroxyhyte ($\delta\text{-FeOOH}$). The spectra of the latter four species share a peak at $\sim 700\text{ cm}^{-1}$, and due to peak broadening and similarity between the spectra, unambiguous assignment is challenging [20]. However, the identification of magnetite was supported by the evidence of a peak centred at 553 cm^{-1} , and maghemite was identified by the peaks at 350 cm^{-1} and 500 cm^{-1} in the top spectrum [21-22]. Additionally, there was evidence of

Fe₃C enrichment at the CS surface, based on the band from 1400 cm⁻¹ to 1600 cm⁻¹, which is consistent with graphitic C residues from Fe₃C formation [23-25]. These signals corresponded to low-lying corrosion products on the sample surface, as mapped in Figure 4.7b.

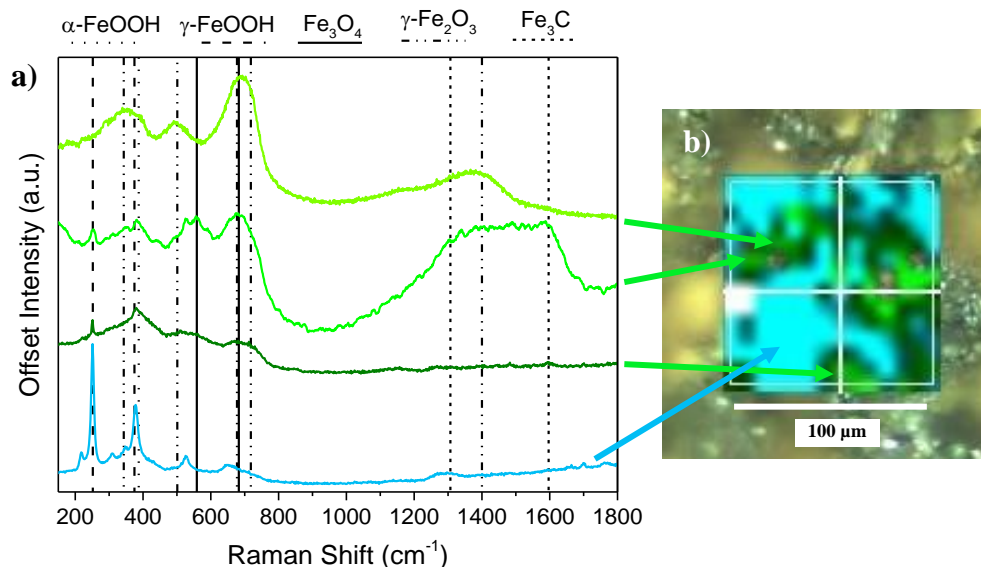


Figure 4.7 Raman a) spectra and b) area map recorded on CS after corroding at a Cu:CS area ratio of 10:1 in 1 M NaCl without bentonite.

The diffuse yellow-orange deposits atop the compact film corresponded to highly crystalline lepidocrocite [22], confirmed by the sharp peaks at 254 cm⁻¹ and 379 cm⁻¹ in the lowermost spectrum. This positively identifies the deposits, mapped in blue in Figure 4.7b, as the spinous cluster deposits observed under SEM.

Upon addition of a very thin (1 mm) bentonite layer to the surfaces of the electrodes, the CS surface was uniformly etched, with faint evidence of polishing lines, as shown in Figure 4.8. A thin film which had a very fine netted structure covered the entire surface, with isolated small corrosion deposits resting atop the film. These deposits were smaller and less abundant than those observed in the absence of bentonite. Notably, S-rich inclusions in the CS were associated with pit formation; such pitting behaviour is a common phenomenon observed in steels [26]. Additionally, the interaction between the bentonite clay particles and the CS surface contributed to the favourability of localized corrosion [27], possibly exacerbating pitting both at S-rich inclusions and elsewhere on the surface. In the presence of a 1 mm layer of bentonite, corrosion products

were observed to be retained in the clay, based on orange staining in the slurry layer radiating outwards from the location of the CS after ~24 hours of immersion.

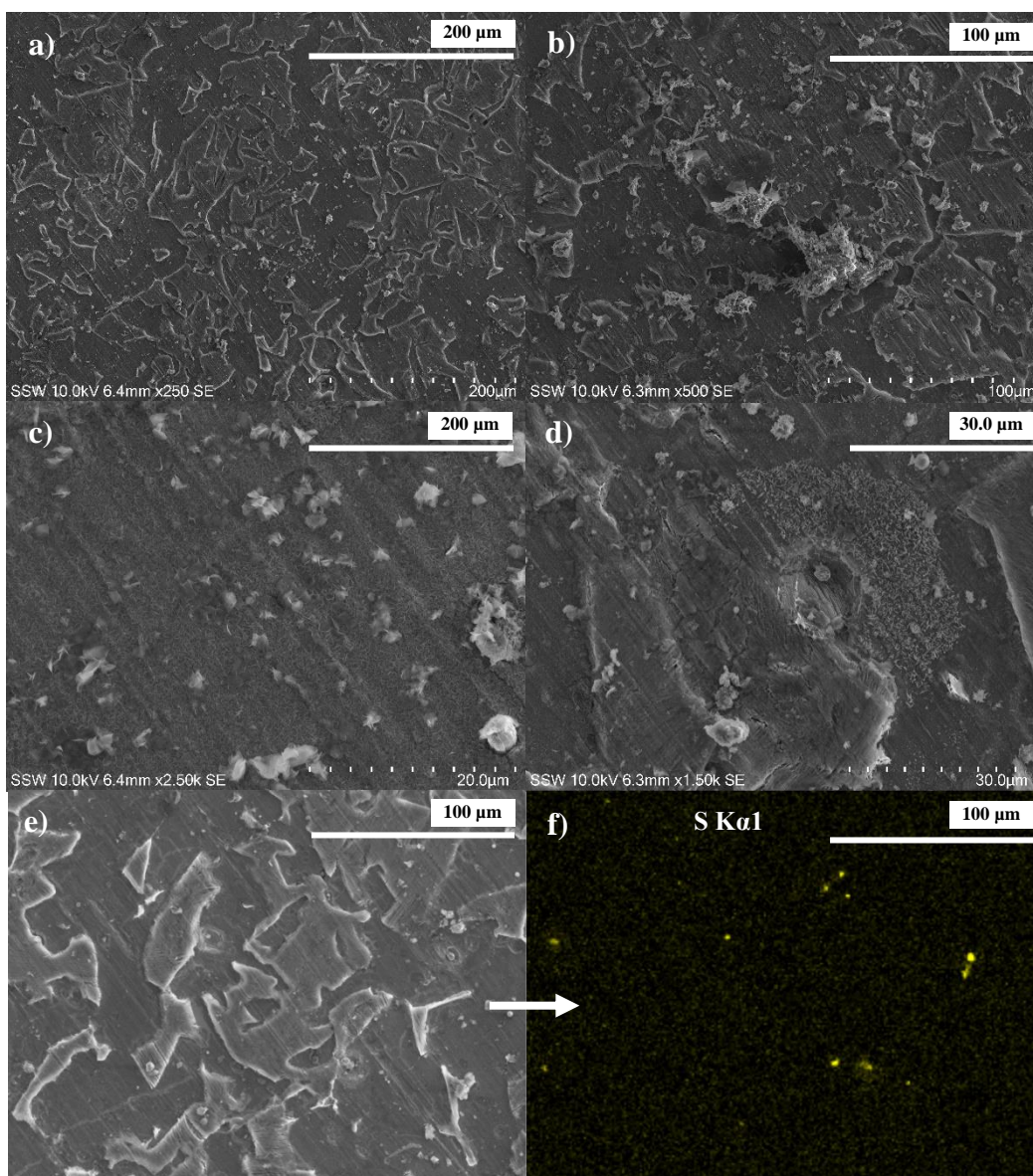


Figure 4.8a-e) SEM images of CS corroded at a Cu:CS area ratio of 10:1 in 1 M NaCl under a 1 mm bentonite layer and f) EDX area map of S signals corresponding to electron image e.

Raman spectra recorded on CS after corrosion under a 1 mm layer of bentonite, Figure 4.9, revealed a variety of corrosion products on the surface. The small corrosion product deposits exhibited sharp peaks at 255 cm^{-1} , 380 cm^{-1} , and a small peak at 1281 cm^{-1} , characteristic of lepidocrocite. The thin film was found to be composed of disordered goethite, characterized by a broad signal centred at 390 cm^{-1} , and magnetite, which gave a sharp peak at 677 cm^{-1} . A shoulder

at 739 cm^{-1} seen in several spectra, could indicate the presence of small amounts of maghemite as well. As in the absence of bentonite, a broad peak between 1246 cm^{-1} and 1667 cm^{-1} indicated that Fe_3C in pearlite grains was preferentially retained, which resulted in the etching pattern. The predominant (or lone) peak at 550 cm^{-1} was attributed to $\text{Fe}(\text{OH})_2$, which has been shown to be present in passivating layers formed in the presence of CO_3^{2-} and other groundwater ions [28-30]. Dissolution of calcite, dolomite, siderite, and magnesite constituents in the bentonite clay would result in the introduction of small amounts of CO_3^{2-} to the system [31].

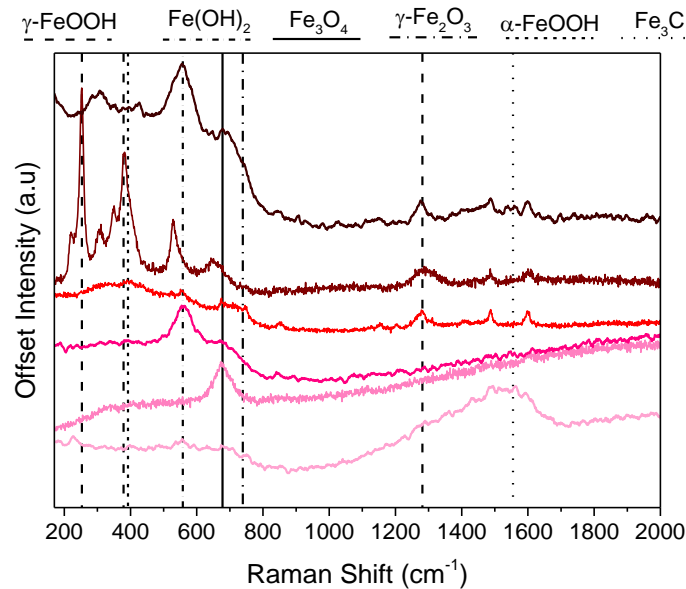


Figure 4.9 Raman spectra recorded on CS after corroding at a Cu:CS area ratio of 10:1 in 1 M NaCl under a thin (1 mm) layer of bentonite.

Increasing the thickness of the bentonite layer to and beyond 5 mm resulted in an etched pattern similar to that produced under a 1 mm bentonite layer. SEM images, Figure 4.10, revealed that the surfaces of the CS samples were covered with a thin film that left polishing lines easily discernable, and the surface lacked noticeable Fe (oxyhydr)oxide deposits. EDX analysis of a representative region of the CS surface showed strong O signals collocated with Si and Al, which therefore were attributed to adhered bentonite clay particulates, leaving the film to be only 4% to 6% O by weight. Just as in the 1 mm bentonite layer experiments, pits were found to form at the sites of S-rich inclusions in the steel, and again the bentonite likely increased the favourability of this localized corrosion. The thicker (≥ 5 mm) bentonite layer resulted in a slightly higher pit density on the CS surface.

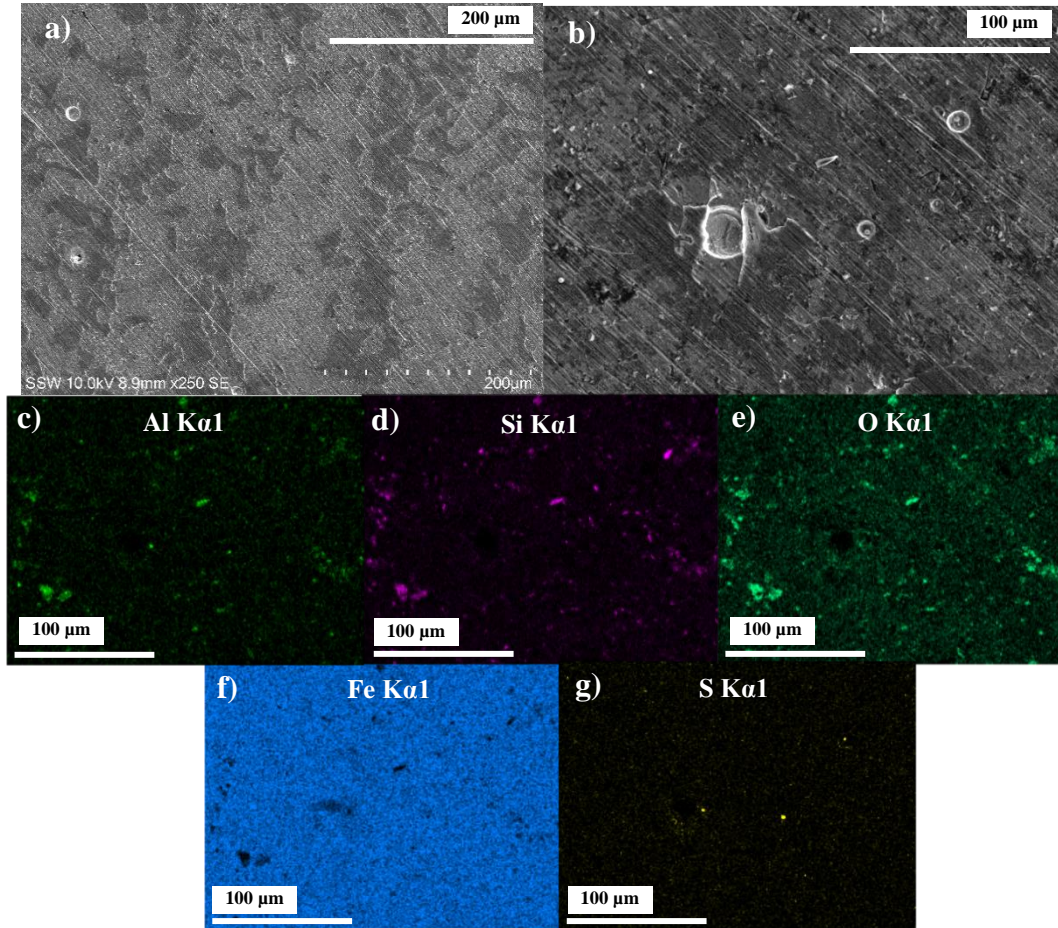


Figure 4.10 SEM images of CS corroded at a Cu:CS area ratio of 10:1 under a) a 20 mm, and b) a 5 mm bentonite layer with EDX area maps of the c) Al, d) Si, e) O, f) Fe, and g) S signals corresponding to electron image b.

As seen in Figure 4.11b, the raised grains present on the CS surface after corrosion under a ≥ 5 mm thick bentonite layer were easily discernable by optical microscope. Raman spectroscopic mapping showed that these grains corresponded to amorphous C signals, confirming that Fe_3C -rich pearlite grains were selectively retained. Some characteristic lepidocrocite signals were found at 249 cm^{-1} and 380 cm^{-1} , in addition to other signals centred at 300 cm^{-1} and 420 cm^{-1} , which were consistent with ferric chloride hexahydrate [32] ($\text{FeCl}_3 \cdot 6\text{H}_2\text{O}$), though these species were sparsely distributed on the surface. Signals in the range of 640 cm^{-1} to 670 cm^{-1} could indicate the presence of a magnetite film [22], though the weakness of these signals and the small O content across the CS surface would suggest that such a film was extremely thin. The presence of magnetite would be consistent with a deficiency of O_2 at the CS surface under the bentonite slurry layer. Generally, the Raman signals indicated that corrosion products formed under a thick bentonite layer lacked crystallinity and were sparse or thin.

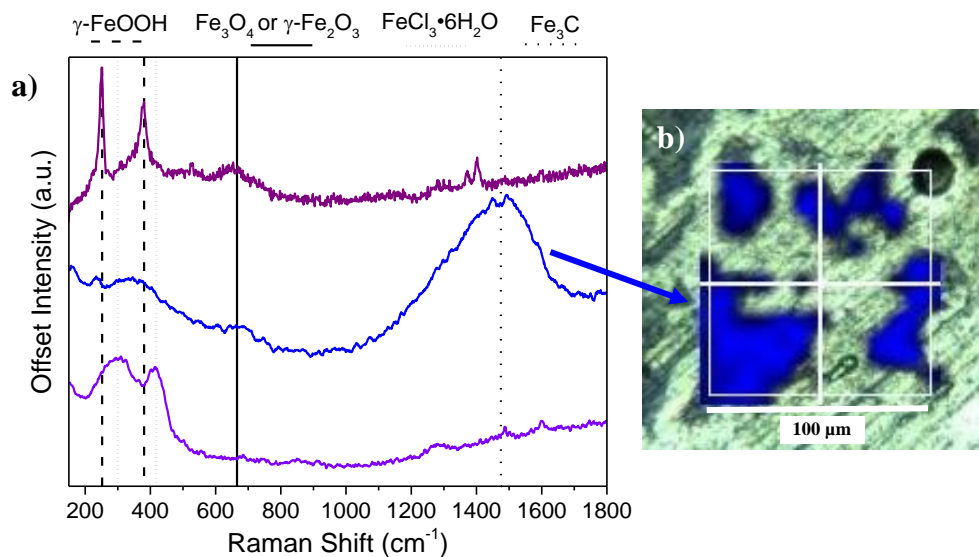


Figure 4.11 Raman a) spectra and b) area map recorded on CS after corroding at a Cu:CS area ratio of 10:1 in 1 M NaCl in the presence of a thick (>5 mm) bentonite layer.

4.3.4 EIS of Carbon Steel and Copper in Various Amounts of Bentonite

EIS data were collected on CS from a DC bias corresponding to the steady-state E_g obtained in the absence of bentonite, as well as under a 1 mm, 5 mm, 9 mm, 12 mm, or 20 mm bentonite layer. Equivalent circuits used to simulate EIS data recorded on CS are summarized in Figure 4.12. The Nyquist plots, Figure 4.13a, exhibited significantly depressed semi-circles whose radii increased regularly with increasing bentonite layer thickness, with the exception of the 9 mm layer, which had a slightly smaller radius than that of the 5 mm layer. The depressed semi-circle was consistent with non-ideal capacitive behaviour, attributed to the electric double layer (CPE_{dl}), contributions from the oxide film (CPE_{film}), and the presence of diffuse double layers in the bentonite layer near the electrode surface [33-34] (CPE_{bent}).

R_{pore} was related to geometric constraints of ruptures in the oxide film, the walls of which could act as cathodic sites [35-36], while R_{film} was the resistance of the film itself. R_P was the polarization resistance, R_{bent} was the resistance imparted by the bentonite clay near the electrode surface, and R_s was solution resistance, which included contributions from diffuse bentonite slurry more distant from the electrode surface.

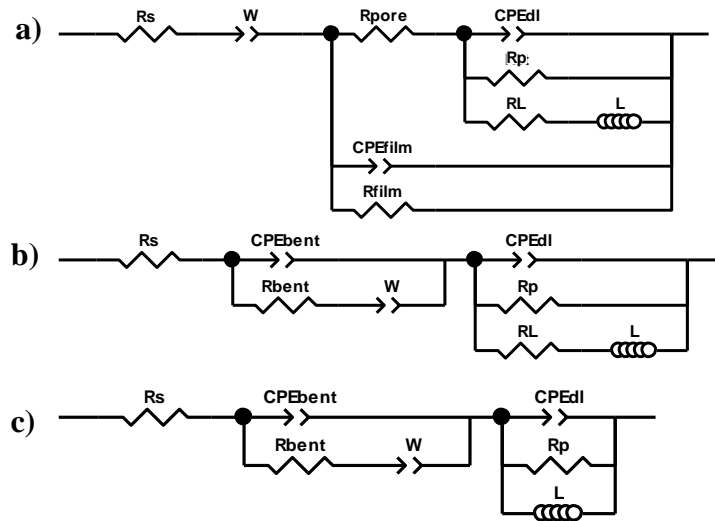


Figure 4.12 Equivalent circuits for a) CS in aerated 1 M NaCl in the absence of bentonite, b-c) CS in aerated 1 M NaCl in the presence of bentonite.

At very low frequencies, the Nyquist plots acquired in the bentonite-free experiment, and the experiments with 9 mm and 12 mm bentonite layers showed linear regions which are characteristic of a semi-finite Warburg impedance brought about by O_2 diffusion through the Fe oxide layers [17], oxide pores, and/or through the bentonite clay near the CS surface [27].

Three of the plots of EIS data recorded on CS showed inductive behaviour at very low frequency which is related to adsorbed intermediate species [37-38]. This inductive behaviour was modelled with R_L representing inductive resistance and L representing the pseudo-inductor. Though not all CS spectra explicitly displayed an inductive loop (only the 1 mm, 5 mm and 20 mm bentonite layers), such inductive behaviour is commonly observed on steel [39-40] because of the $Fe(OH)_{ads}$ intermediate intrinsic to the dissolution mechanism, and thus the inductor element was included in all CS equivalent circuits. When R_L was comparable in magnitude to R_P , it was included in the equivalent circuit used to simulate the data, however, when the bentonite layer exceeded 5 mm and E_g became more negative, the inclusion of R_L no longer improved the fitting of the circuit, implying that its magnitude was incompatible with the measurement, e.g. a large decrease in R_L compared to R_P would lead to a negligible contribution to the total impedance.

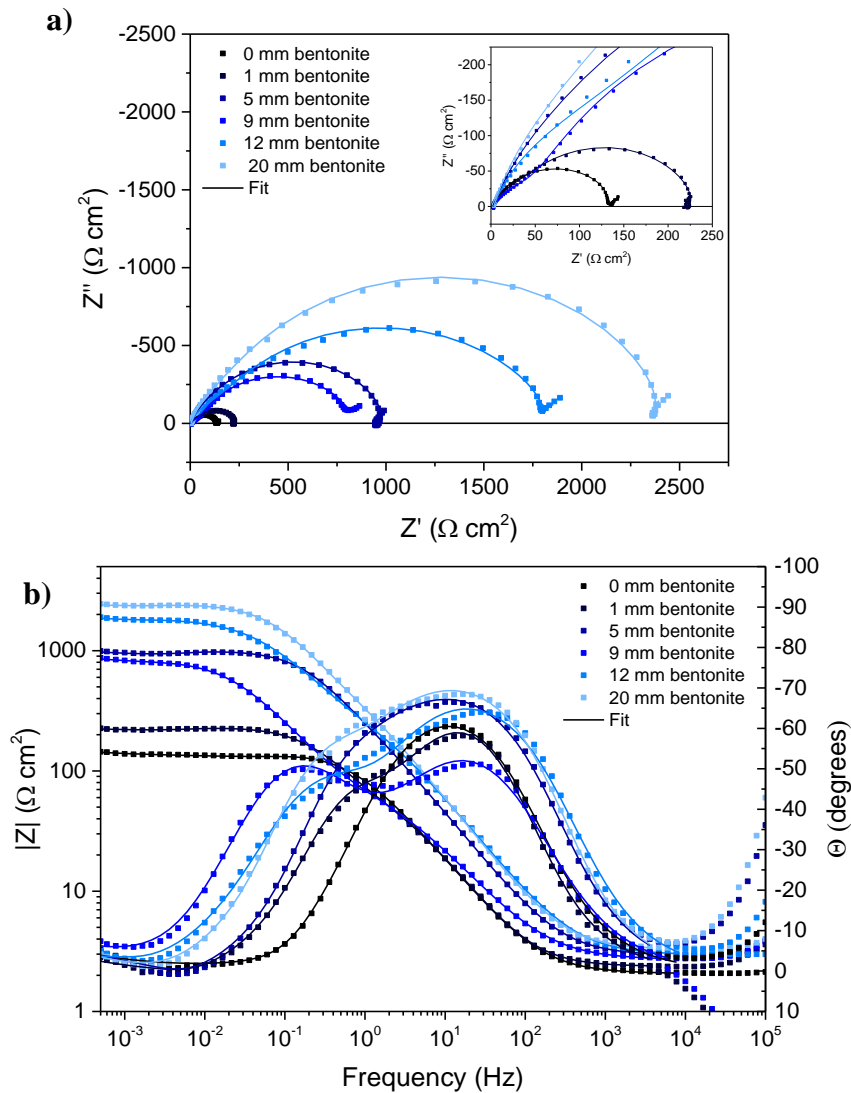


Figure 4.13 a) Nyquist and b) Bode plots of EIS data recorded on Cu from E_g , as obtained from galvanic coupling experiments under the same conditions (1 M NaCl and bentonite layers of various thickness). The solid curves are simulations generated by equivalent circuits and correspond to the experimental points of like colour.

In the absence of bentonite, the corrosion film was found to have a rather large impedance ($12,500 \Omega \text{ cm}^2$) due its composition of maghemite, lepidocrocite, and goethite, which have very low conductivity at room temperature [41]. The pathway to the CS surface provided by the open ruptures in the film contributed a much lower resistance ($84 \Omega \text{ cm}^2$) and allowed the corrosion rate to remain high.

The addition of a 1 mm layer of bentonite clay corresponded to an increase in $|Z|$ at low frequency from $140 \Omega \text{ cm}^2$ in the absence of bentonite to $230 \Omega \text{ cm}^2$ in the 1 mm bentonite layer, Figure 4.13b. When the bentonite layer thickness was increased to 5 mm and then 9 mm, the $|Z|$

rose to $990 \Omega \text{ cm}^2$, but then fell to $870 \Omega \text{ cm}^2$. This behaviour can be explained by the fact that the bentonite settled on the electrode surface by first forming a lower region of heavier particles which fell instantly, and a more diffuse upper region which took much longer to settle. In the short time after cessation of stirring of the bentonite mixture in the cell, the brief continued movement of the solution could have disturbed and prevented the buildup of that lower layer. When the total bentonite layer thickness increased to 12 mm, the $|Z|$ increased to $1,900 \Omega \text{ cm}^2$ and increased further to $2,500 \Omega \text{ cm}^2$ in a 20 mm bentonite layer, as expected. Due to the large amounts of bentonite added to the cell, burial of the electrodes occurred in the 12 mm and 20 mm cases, dampening the effect of solution circulation on establishment of the lower bentonite layer.

Figure 4.14 summarizes the values of R_S , R_P , and R_{bent} , plotted as a function of bentonite layer thickness. The elements R_S and R_{bent} were interpreted to be related to the upper diffuse region of the bentonite layer and the lower dense region of the bentonite layer, respectively. The magnitudes of R_S and R_{bent} generally increased with addition of thicker bentonite layers; this was an expected result as these elements were intrinsically linked to the bentonite itself. R_P , which represents the corrosion rate, gave an indication of secondary effects of bentonite addition. Notably, the trend in R_P followed that of R_{bent} very closely. This trend of gradually increasing R_P does not reflect the sharp decrease followed by a plateau observed in the galvanic coupling experiments.

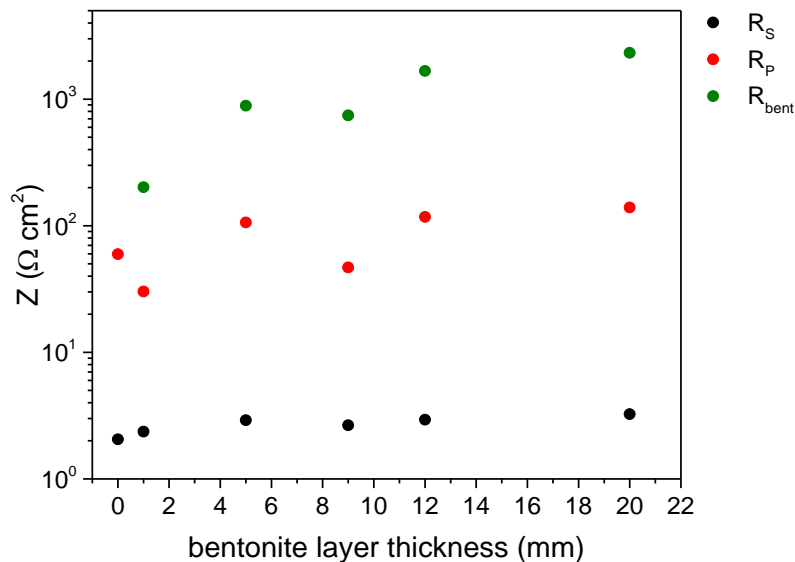


Figure 4.14 Impedance contributions from R_S , R_P , and R_{bent} plotted as a function of bentonite layer thickness for CS samples at E_g in 1 M NaCl and various amounts of bentonite.

EIS experiments were repeated under the same conditions, but with Cu as the working electrode. The circuit used to simulate Cu data is shown in Figure 4.15. The Nyquist plots, Figure 4.16a, curved slightly to the right, forming a partial semi-circle which never re-crossed the real axis. The plots took on a more linear form at lower frequencies, with the exception of the data plot acquired

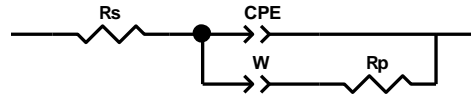


Figure 4.15 Equivalent circuit for Cu in 1M NaCl in both the absence and presence of bentonite clay.

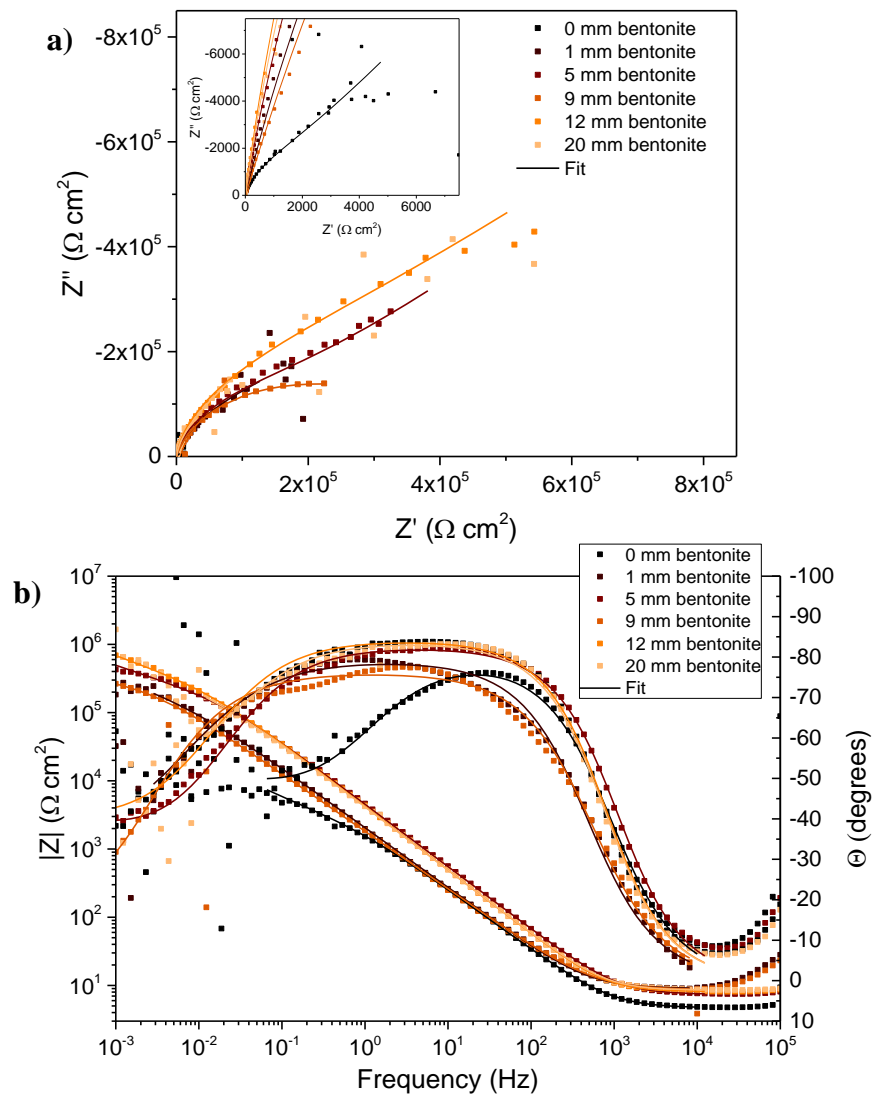


Figure 4.16 a) Nyquist and b) Bode plots of EIS data recorded on Cu from E_g , as obtained from galvanic coupling experiments under the same conditions (1 M NaCl and bentonite layers of various thickness). The solid curves are simulations generated by equivalent circuits and correspond to the experimental points of like colour.

in the presence of the 9 mm bentonite layer, which continued to curve at low frequency. The linear regions were at approximately a 45° angle in the complex plane and were accounted for with a semi-infinite Warburg element to represent the diffusion of O_2 to the electrode surface. The solution resistance was again represented by R_S , and the polarization resistance by R_P . The electric double layer at the Cu surface was represented by CPE_{dl} . In the absence of bentonite, the corrosion of Cu in simulated groundwater solutions has been modelled by Kosec et al. with consideration of an insulating oxide film [14]; in this work, the cathodic polarization of the Cu from its E_{corr} to E_g suppressed the anodic activity required to form such a film. This was confirmed by EDX analysis of the Cu, Figure 4.17, which shows that the Cu surface was undamaged and the only O signals could be attributed to Fe corrosion products which adhered to the Cu surface during the galvanic coupling to CS.

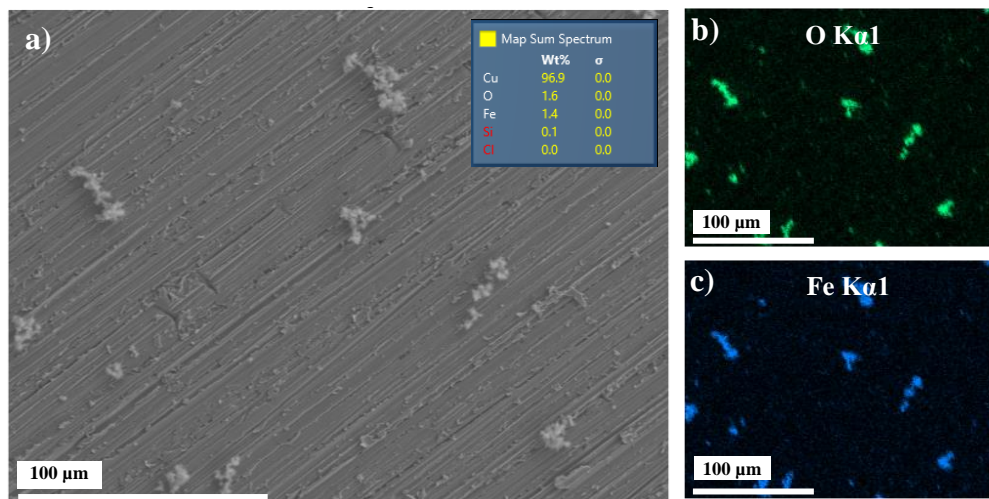


Figure 4.17 a) Electron micrograph of Cu after corrosion in aerated 1 M NaCl without bentonite, and corresponding EDX maps of b) O and c) Fe.

R_P and R_S values determined from EIS data for Cu are plotted as a function of bentonite layer thickness in Figure 4.18. In bentonite-free solution, R_P of the Cu was $3,100 \Omega \text{ cm}^2$, increasing to the order of $2 \times 10^5 \Omega \text{ cm}^2$ upon the addition of bentonite. When present, the amount of bentonite did not appear to significantly affect the R_P , though the low frequency noise in the data introduced some difficulty in determining the precise changes in $|Z|$. The large increase of R_P upon addition bentonite indicated slower corrosion of the Cu. As in the case of the CS, the addition of bentonite contributed a small increase in the R_S , due to the diffuse upper layer of the bentonite. Given the large negative polarization of the Cu to reach E_g , O_2 reduction was the only significant reaction

occurring on the surface; it follows that the addition of bentonite caused a decrease of the limiting current for O₂ reduction.

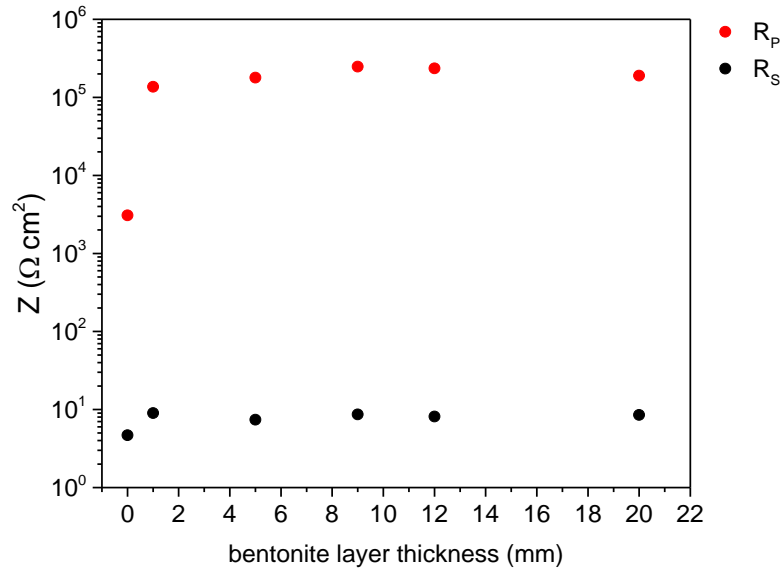


Figure 4.18 Impedance contributions from R_S and R_P plotted as a function of bentonite layer thickness for Cu samples at E_g.

4.4 Discussion

In the corrosion of CS galvanically coupled to Cu, the linear proportionality between i_g and the Cu:CS area ratio and the roughly logarithmic increase in E_g , indicated that the cathodic activity on the Cu controlled the rate of corrosion. The main cathodic reaction on the Cu in neutral, naturally aerated NaCl is the reduction of O₂ (Reaction 4.1):



With the Cu and CS immersed in the same test cell, Fe³⁺ reduction to Fe²⁺ on the Cu was also possible, though the contribution from this reaction was likely small compared to that of O₂ reduction. These relationships held true in both the presence and absence of bentonite, thus O₂ reduction remained the rate-controlling reaction in the presence of bentonite. The shift to more negative E_g and drop in i_g showed that the bentonite caused a decrease in the O₂ concentration at the Cu surface by hindering its diffusion [14], leading to a significant decline in the limiting current for O₂ reduction.

The corrosion of CS is typically influenced by the buildup of insoluble rust layers on the surface, which can inhibit O₂ reduction if they are composed of Fe^{III} phases [42]. In the absence of bentonite at a 10:1 Cu:CS area ratio, the build-up of corrosion products caused the gradual decrease in E_g because of blockage of surface reactivity while the Cu functioned effectively as an inert O₂ electrode, as evident in the stability of i_g over time. Indeed, the abundant corrosion product found on the CS was composed primarily of Fe^{III} phases: maghemite, goethite, and lepidocrocite. After corrosion at a Cu:CS area ratio of 10:1 under a thin (1 mm) layer of bentonite, the CS surface featured more O-deficient Fe^{II} and Fe^{II}/Fe^{III} phases, such as ferrous hydroxide and magnetite. When the bentonite layer increased in thickness, magnetite was again found alongside very sparse signals for Fe^{III} phases such as ferric chloride hexahydrate and lepidocrocite. The corrosion of steel in low-O₂, saturated, compacted bentonite clay has been associated with the formation of a magnetite film and some oxyhydroxide species, as well as the sorption of Fe ions in the clay [43-44]. The sparseness of Fe^{III} species observed on the surface could be explained by a combination of low O₂ concentrations in the clay and retention of Fe²⁺/Fe³⁺ in the clay, preventing the deposition of corrosion products. It is clear that adding moderate amounts of bentonite slurry inhibited the transport of O₂ more effectively than the buildup of oxidized corrosion products, and that the bentonite actively prevented the deposition of corrosion products on the surface.

Though the addition of bentonite caused a negative shift of E_g and a significant decrease in i_g , this effect was limited as the bentonite layer thickness exceeded 5 mm. At the slightly alkaline pH which prevailed in the bentonite clay (~8.5), the contribution of H⁺ reduction on CS would be negligible [45-46], also considering the unfavourable thermodynamics and kinetics of H⁺ reduction on Cu [46], and thus O₂ was the primary oxidant. In the plateaued region of the E_g and i_g plots where the bentonite layer thickness exceeded 5 mm, the O₂ concentration at the Cu surface after 24 hours was relatively low and decreased only very slightly with additional bentonite, though this plateau region occurred at more positive potentials and higher galvanic currents than would be expected if the electrode surfaces had reached fully de-aerated conditions. The slope change observed in the i_g values was reflected in the results of EIS measurements on the Cu. From the 0 mm bentonite layer to the 20 mm bentonite layer, the R_P determined from EIS increased by a factor of approximately 62, which is consistent with the factor of 53 decrease in i_g determined from galvanic coupling experiments. EIS measurements on the CS gave a clearer indication of the effect of increasing the thickness of the bentonite layer, as $|Z|$ generally increased with the bentonite layer

thickness, driven by increases in R_S , R_P , and R_{bent} . The plateau behaviour observed in i_g manifested in the R_P of Cu, which, in the presence of bentonite, exceeded R_{bent} by at least two orders of magnitude, thus contributing relatively little to the total impedance and explaining the minimal change in E_g and i_g once the layer thickness exceeded 5 mm.

4.5 Conclusions

In the investigation of Cu/CS galvanic couples over a range of Cu:CS area ratios corroding under obstructing layers of bentonite slurry, E_g and i_g measurements, complemented by EIS analysis and surface characterization, were used to determine the effect of bentonite layer thickness on the corrosion rate of CS.

- In the galvanic corrosion of CS when coupled to Cu, the addition of bentonite clay produced benign corrosion conditions through a negative shift in E_g and significant decrease in the i_g on CS. The E_g increased logarithmically and the i_g increased linearly, regardless of whether bentonite was present, indicating that the overall negative shift in E_g and i_g decrease were related to the limiting current of O_2 reduction on Cu.
- The presence of bentonite clay prevented deposition of Fe^{III} corrosion products on the CS surface. The corrosion film on all CS samples was relatively thin and non-protective, likely due to the presence of Cl^- and S-rich inclusions in the CS. The CS corroded under thick bentonite layers carried a higher pit density as a result of interaction with bentonite particles at the surface.
- As the thickness of the bentonite layer obstructing the electrode surfaces increased, the contribution of the bentonite resistance was small compared to the large R_P associated with O_2 reduction on the Cu, causing the flattening of the E_g and i_g versus bentonite layer thickness plots when the thickness exceeded 5 mm.

In the deep geological repository, the galvanic corrosion which could be possible at a through coating defect would be greatly hindered by the presence of the bentonite clay barrier. This work demonstrated that in low bentonite density, high conductivity, large Cu:CS area ratio, and an endless supply of O_2 , the galvanic corrosion of CS slowed significantly compared to that in the absence of bentonite.

4.6 References

1. F. Garisto *Seventh Case Study: Features, Events and Processes*; TR-2018-05; NWMO: Toronto, Canada, 2018.
2. O. Karnland *Chemical and mineralogical characterization of the bentonite buffer for the acceptance control procedure in a KBS-3 repository*; TR-10-60; SKB: Stockholm, Sweden, 2010.
3. F. King, D. S. Hall, P.G. Keech, *Corros. Eng. Sci. Techn.* **2017**, *52*, 25-30.
4. R. Guo *Thermal Response of a Mark II Conceptual Deep Geological Repository in Crystalline Rock*; TR-2016-03; NWMO: Toronto, Canada, 2016; pp 10-14.
5. T. E. Standish, D. Zagidulin, S. Ramamurthy, P. G. Keech, J. J. Noël, D. W. Shoesmith, *Corros. Eng. Sci. Techn.* **2017**, *52*, 65-69.
6. T. Standish, D. Zagidulin, S. Ramamurthy, P. Keech, D. Shoesmith, J. Noël, *Geosciences* **2018**, *8*, 1-14.
7. T. Standish, J. Chen, R. Jacklin, P. Jakupi, S. Ramamurthy, D. Zagidulin, P. Keech, D. Shoesmith, *Electrochim. Acta* **2016**, *211*, 12.
8. T. E. Standish, L. J. Braithwaite, D. W. Shoesmith, J. J. Noël, *J. Electrochem. Soc.* **2019**, *166*, C1-C8.
9. A. P. Rance N. R. Smart, P. A. H. Fennell *Galvanic corrosion of copper-cast iron couples*; TR-05-06; SKB: Stockholm, Sweden, January 2005, 2005; p 78.
10. J. Stoulil, M. Kouřil, L. Pavlova, D. Dobrev, J. Gondolli, *Mater. Corros.* **2018**, 1-7.
11. C. A. J. Appelo *A Review of Porosity and Diffusion in Bentonite*; 2013-29; Posiva: Eurajoki, Finland, 2013.
12. E. Wieland, H. Wanner, Y. Albinsson, P. Wersin, O. Karnland *A surface chemical model of the bentonite-water interface and its implications for modelling the near field chemistry in a repository for spent fuel*; SKB: Stockholm, Sweden, 1994.
13. M. Jonsson, *ISRN Mater. Sci.* **2012**, *2012*, 1-13.
14. T. Kosec, Z. Qin, J. Chen, A. Legat, D.W. Shoesmith, *Corros. Sci.* **2015**, *90*, 248-258.
15. J. Stoulil, M. Kouřil, D. Dobrev, *Koroze Ochr. Mater.* **2019**, *63*, 19-22.
16. Y. C. Lim, S. Sanderson, M. Mahoney, J. Chen, S. A. David, Z. Feng, *Sci. Technol. Weld Joi.* **2016**, *21*, 564-569.
17. L. Cáceres, T. Vargas, L. Herrera, *Corros. Sci.* **2009**, *51*, 971-978.

18. M. Dewar. Characterization and Evaluation of Aged 20Cr32Ni1Nb Stainless Steels. University of Alberta, Edmonton, Canada, 2013.
19. M. Villacís-García, M. Ugalde-Arzate, K. Vaca-Escobar, M. Villalobos, R. Zanella, N. Martínez-Villegas, *Bull. Mex. Geol. Soc.* **2015**, *67*, 433-446.
20. L. Bellot-Gurlet, D. Neff, S. Réguer, J. Monnier, M. Saheb, P. Dillmann, *J. Nano. Res.* **2009**, *8*, 147-156.
21. D. L. A. de Faria, S. Venancio Silva, M. T. de Oliveira, *J. Raman Spectrosc.* **1997**, *28*, 873-878.
22. M. Hanesch, *Geophys. J. Int.* **2009**, *177* (3), 941-948.
23. X. Bi, B. Ganguly, G. P. Huffman, F. E. Huggins, M. Endo, P. C. Eklund, *J. Mater. Res. Technol.* **1993**, *8*, 1666-1674.
24. C. T. Lee, Z. Qin, M. Odziemkowski, D. W. Shoesmith, *J. Electrochem. Soc.* **2006**, *153*, B33-B41.
25. E. Park, J. Zhang, S. Thomson, O. Ostrovski, R. Howe, *Metall. Mater. Trans. B* **2001**, *32B*, 839-845.
26. G. Wranglén, *Corros. Sci.* **1974**, *14*, 331-349.
27. M. Jeannin, D. Calonnec, R. Sabot, Ph. Refait, *Corros. Sci.* **2010**, *52*, 2026-2034.
28. J. Gui, T. M. Devine In *Influence of anions on the surface enhanced Raman spectra of passive films formed on iron*, 12th International Corrosion Congress, Houston, USA, NACE International: Houston, USA, 1993; pp 2052-2064.
29. M. S. Odziemkowski, T. T. Schumacher, R. W. Gillham, E. J. Reardon, *Corros. Sci.* **1998**, *40*, 371-389.
30. F. F. Eliyan, J. R. Kish, A. Alfantazi, *J. Mater. Eng. Perform.* **2015**, *24*, 2473-2480.
31. M. Fukue, Y. Fujimori, Y. Sato, T. Nakagawa, C. N. Mulligan, *Appl. Clay Sci.* **2010**, *47*, 133-138.
32. S. K. Sharma, *J. Non-Cryst. Solids* **1974**, *15*, 83-95.
33. P. Wersin, E. Curti, C. A. J. Appelo, *Appl. Clay Sci.* **2004**, *26*, 249-257.
34. V. Sreedharan, S. Puvvadi, *Géotechnique* **2013**, *63*, 876-879.
35. Y. I. Kuznetsov, D. B. Vershok, *Russ. J. Electrochem.* **2001**, *37*, 261-265.
36. L. Cáceres, L. Herrera, T. Vargas, *Corrosion* **2007**, *63*, 722-730.
37. H. Li, D. Li, L. Zhang, Y. Bai, Y. Wang, M. Lu, *RSC Adv.* **2019**, *9*, 11641-11648.

38. I. E. Castaneda-Robles, L. D. López-León, V. M. Moreno-Landeros, M. A. Baltazar-Zamora, F. J. Olguín-Coca, L. G. Lizárraga-Mendiola, *Int. J. Electrochem. Sci.* **2018**, *13*, 9039-9050.
39. H. Li, D. Li, L. Zhang, Y. Bai, Y. Wang, M. Lu, *RSC Adv.* **2019**, *9*, 11641–11648.
40. Q. Li, H. Hu, Y. Frank Cheng, *J. Petrol Sci. Eng.* **2016**, *147*, 408-415.
41. R. M. Cornell, U. Schwertmann, *The Iron Oxides: Structure, Properties, Reactions, Occurrences and Uses*. 2nd ed.; WILEY-VCH Verlag GmbH & Co. KGaA: Weinheim, Germany, 2003.
42. M. Stratmann, J. Müller, *Corros. Sci.* **1994**, *36*, 327-359.
43. N. R. Smart, B. Reddy, A. P. Rance, D. J. Nixon, N. Diomidis, *Corros. Eng. Sci. Techn.* **2017**, *52*, 113-126.
44. P. Wersin, A. Jenni, U. K. Mäder, *Clays Clay Miner.* **2015**, *63*, 51-68.
45. K. Hedenstedt, N. Simic, M. Wildlock, E. Ahlberg, *J. Electroanal. Chem.* **2016**, *783*, 1-7.
46. S. Sharifi-Asl, D. D. Macdonald, *J. Electrochem. Soc.* **2013**, *160*, H382-H391.

5. Galvanic Corrosion at a Through-Coating Defect in the Presence of Chloride and Bentonite

5.1 Introduction

Many countries are making plans to implement DGR storage of used nuclear fuel; some of these countries, including Canada, Sweden, Finland, will be storing the used fuel in steel or cast-iron containers which are protected from corrosion by an outer layer of Cu. Once placed underground, the containers must endure for time scales up to one million years, due to the long-lasting radioactivity of the fuel [1]. Cu serves as a corrosion barrier in many used fuel container designs because it displays a high degree of stability under anoxic repository conditions [2-3], and thus can ensure safe long-term containment of the used fuel.

The Swedish container, KBS-3, follows a dual-wall design in which an inner cast-iron vessel is housed within an outer copper vessel with 50 mm thick walls. The small (1-2 mm) gap between the inner and outer vessels is expected to close upon application of pressure due to the deformation of the non-load-bearing copper [4]. By contrast, the Canadian nuclear waste container, designed to contain CANDU fuel bundles, uses a CS vessel coated in ~3 mm of Cu, integrally bonded to the steel by electrodeposition and thermal cold spray coating techniques [5]. Calculated corrosion rates of the coating, with contributions from uniform corrosion due to trapped O₂, under-deposit corrosion, and microbially influenced corrosion (MIC), have produced a very conservative Cu corrosion allowance of ~1.3 mm over one million years [6], less than half the coating thickness. While this estimate is encouraging, the thin Cu coating in the Canadian design cannot be said to have the same robustness as the thick Cu shell in the Swedish design, and the calculated corrosion allowance assumes a perfectly intact Cu coating.

It is vital to investigate the possible consequences of a defect in the coating of a container sealed in the Canadian DGR. Under such conditions, galvanic coupling between the more noble Cu coating and the more active CS exposed at the base of the defect is theoretically possible and could result in accelerated degradation of the CS and eventual container failure. While O₂ is present in the DGR, galvanic corrosion will be driven by O₂ reduction on the Cu coating coupled to oxidation and subsequent dissolution of Fe from the CS substrate. The geometry of the defect will have a profound effect on the transport of reacting species to the copper surface and steel substrate, as

well as the transport of corrosion products from the steel. Previous work has suggested that a gradient in solution chemistry existed within the defect, as Fe^{2+} was produced at the CS surface and hydrolysis reactions caused a pH drop, while anions like Cl^- migrated into the defect in response to buildup of positive charge [7]. Additionally, the deposition of Fe (oxyhydr)oxides on the top Cu surface suggested that the interior of the defect was O_2 deficient, which allowed for transport of Fe^{2+} ions out of the defect before they could be oxidized further [7].

In addition to the constrained geometry of a hypothetical defect, the nature of the Cu/CS interface is expected to influence corrosion of the CS. In the Mark 2 container design, the Cu coating is to be applied to the container body and hemispherical end caps by electrodeposition. The CS is chemically de-rusted before the electrodeposited coating is applied, leaving intact any macro-scale features caused by machining, but generally creating a relatively smooth Cu/CS interface. At the weld region where the loaded container is sealed, the Cu coating is applied by thermal cold spray deposition; the adhesion of the cold spray coating relies heavily on mechanical interlocking between the Cu particle “splats” and a roughened substrate surface [8]. Thus, in order to improve coating adhesion, the CS is first abraded with alumina particles (some of which may become embedded), producing a much rougher Cu/CS interface. The Cu particle impact can also induce microstructural and hardness changes at the steel substrate [9]. The properties of the Cu/CS interface have been shown to significantly affect the preferential direction of CS corrosion, though not the total corrosion volume [10-11].

The compacted bentonite clay surrounding the used fuel container acts as a barrier to the transport of groundwater and oxidizing species towards the container. The effect of bentonite on the corrosion of the CS substrate at a coating defect is yet unstudied. In order to establish a galvanic couple between the CS substrate and the Cu coating, they must be exposed together to a conductive medium. In the case of a compacted bentonite buffer box, this conductive medium can only be established if the bentonite clay is saturated with solution and has expanded to fill the through-coating defect. At the minimum target bentonite dry density of 1.6 g cm^{-3} , the bentonite swelling pressure is expected to exceed 5 MPa and the hydraulic conductivity would be on the order of $10^{-13} \text{ m s}^{-1}$, suppressing microbial activity [12]. The establishment of a Cu/CS galvanic couple at a through-coating defect in the presence of highly compacted bentonite has not yet been studied.

This work seeks to lay groundwork for such studies by investigating galvanic corrosion at a through-coating defect in the presence of bentonite slurry which both covers the Cu coating and fully infiltrates the defect. Over intermediate-term (14-day) experiments, the progression of corrosion of CS and Cu at a through-coating defect, both in the presence and absence of bentonite, was monitored by X-ray micro-computed tomography, complemented by open circuit potential and linear polarization resistance measurements and post-mortem surface analysis.

5.2 Experimental Methods

5.2.1 Sample Preparation

Samples 2 mm in diameter were cut from blocks of A516 gr. 70 carbon steel coated with ~3 mm of Cu, by either electrodeposition or cold spray, provided by Integran Technologies (Mississauga, Canada) and National Research Council (NRC) Canada Industrial Materials Institute (Boucherville, Canada), respectively. Prior to sample preparation, the block coated by cold spray was annealed under Ar atmosphere at 350 °C for one hour to relieve residual stress in the coating by encouraging recrystallization and grain growth [13]. To simulate a through-coating defect, a 0.5 mm diameter hole was drilled through the Cu coating to the Cu/CS interface so as to expose CS at the base of the defect. Using a syringe with a 30-gauge needle, the drilled hole was flushed with tetrachloroethylene (TCE) to remove traces of lubricants and cutting fluids before the sample was sonicated in a TCE bath for five minutes.

Before each experiment, slightly wetted SiC paper was used to grind the Cu-coated end of the sample to a p600, p1200, and p2500 finish in sequence, sonicating the sample and flushing the hole with methanol between each grit. The samples were then dried under a stream of Ar. TorrSeal epoxy (Kurt J. Lesker Company) was applied to the sample, ensuring total coverage around the Cu/CS interface, and the sample was loaded vertically into the electrochemical cell from the bottom such that only the top of the Cu coating and interior of the hole was exposed within the cell. Two additional coats of TorrSeal were applied to secure the sample in place and ensure a leakproof seal. If not being used immediately, the mounted samples were stored in an anaerobic chamber to prevent unwanted oxidation.

5.2.2 Experimental Setup

The electrochemical cell consisted of a single 20 mL compartment which was tapered to a hole at the bottom where the sample was mounted, Figure 5.1. The reference electrode (saturated Ag/AgCl, +0.199 V vs. SHE), the counter electrode (a Pt wire), and Teflon tubing, which served as a gas inlet, were all secured in a rubber stopper fit into the cell lid. Experiments were conducted in solutions of reagent grade NaCl (Fisher Scientific) made to 1 M with ultrapure water (resistivity of 18.2 M Ω cm) from a Thermo Scientific Barnstead Nanopure water purification system. When filling the cell, a syringe with a 30-gauge needle was used to first load electrolyte into the drilled hole of the sample, eliminating any air bubbles within the hole. For experiments in bentonite, MX-80 Wyoming bentonite with an initial moisture content of 20%, provided by NWMO, was added to the cell to achieve a bentonite content of 50 g L⁻¹. The bentonite was carefully added after the cell was filled with electrolyte to ensure that there was a conductive path between the CS and the top face of the Cu. The cells were continuously sparged with medical grade air provided by PRAXAIR.

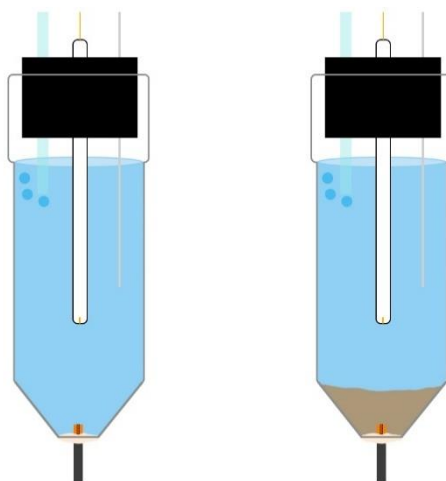


Figure 5.1 Illustration of electrochemical cell setup where the exposure conditions were aerated a) 1 M NaCl and b) 1 M NaCl with 50 g L⁻¹ bentonite clay.

Using a ModulabXM ECS potentiostat (Solartron Analytical) and the accompanying XM-Studio software, OCP was recorded for the duration of the 14-day experiments, with LPR measurements taken every 6 hours, scanning ± 5 mV around OCP at a scan rate of 10 mV min⁻¹.

5.2.3 X-ray micro-CT

X-ray micro-CT data were collected using a Zeiss Xradia 410 Versa Micro-CT with a Hamamatsu X-ray source before the start of the experiment, then after 24 h, 48 h, 72 h, 120 h, 168 h, 240 h, 288 h, and 336 h. At each time point, the entire cell was mounted in the instrument and the sample was located and centred using a 4× objective, achieving a resolution of 3.11 μm per pixel. X-ray micro-CT scans were obtained with a source accelerating voltage and power of 150 kV and 9.9 W, respectively. In order to minimize the production of water radiolysis products, gaps in electrochemical data, and blurring effects for *in-situ* scans, the total scan time was minimized by using a 5 s exposure for each of 801 projections and 180° fan rotation of the sample. The first (before the experiment) and final (after ~336 h) scans were collected using 10 s exposure times to minimize noise.

X-ray micro-CT data were processed using the Zeiss Reconstruction software and analyzed using Arivis Vision4D software (Arivis AG). Volumes of interest were segmented according to intensity values of the greyscale image slices, where very low intensity values corresponded to electrolyte-filled space in the hole and any other low-density species such as corrosion products, alumina, and bentonite, intermediate intensity values corresponded to CS, and high intensity values corresponded to Cu.

5.2.4 Surface Analysis

After completion of the final micro-CT scan, the samples were removed from the cell, rinsed in ultrapure water, dried under a stream of Ar, and stored in an anoxic chamber. The samples were then cast in Epofix epoxy resin and ground to form a cross section in the plane perpendicular to the Cu/CS interface, halfway through the drilled hole.

The samples were then analyzed using Raman spectroscopy using a Renishaw InVia Reflex Raman Spectrometer with a HeNe laser with a wavelength of 633 nm and 1800 l mm⁻¹ grating. Optical micrographs were recorded using a Keyence VHX-6000 Digital Microscope. SEM images and EDX data were collected using a Hitachi SU3500 Variable Pressure SEM with an Oxford Aztec XMax-50 SSD X-ray analyzer. All surface analysis was performed at Surface Science Western (London, Canada).

5.3 Results

5.3.1 Electrochemistry Results for Electrodeposited Cu-coated Samples

OCP measurements of the coupled potential (E_g) of the Cu/CS couple were recorded over a period of 14 days, with LPR measurements taken every 6 hours to obtain R_P values, which are inversely proportional to corrosion current. In this system, where the reactive surfaces of CS and Cu are configured in parallel, the resistances measured by the LPR method follow the expression 5.1:

$$\frac{1}{R_{\text{interfacial}}} = \frac{1}{R_{P,CS}} + \frac{1}{R_{P,Cu}} \quad (5.1)$$

where $R_{\text{interfacial}}$ is the resistance of charge transfer at the reactive interfaces in $\Omega \text{ cm}^2$, $R_{P,CS}$ and $R_{P,Cu}$ are the polarization resistances of the CS and Cu, respectively, in $\Omega \text{ cm}^2$. At E_g , the impedance of the Cu is extremely large compared to the impedance of the CS, and as a result, $\frac{1}{R_{\text{interfacial}}} \approx \frac{1}{R_{P,CS}}$.

Thus, LPR measurements of this system give information about the corrosion rate of the CS with almost no contribution from Cu corrosion. Henceforth, all R_P are assumed to equal $R_{P,CS}$. The progression of E_g and R_P of electrodeposited Cu-coated CS samples in both the absence and the

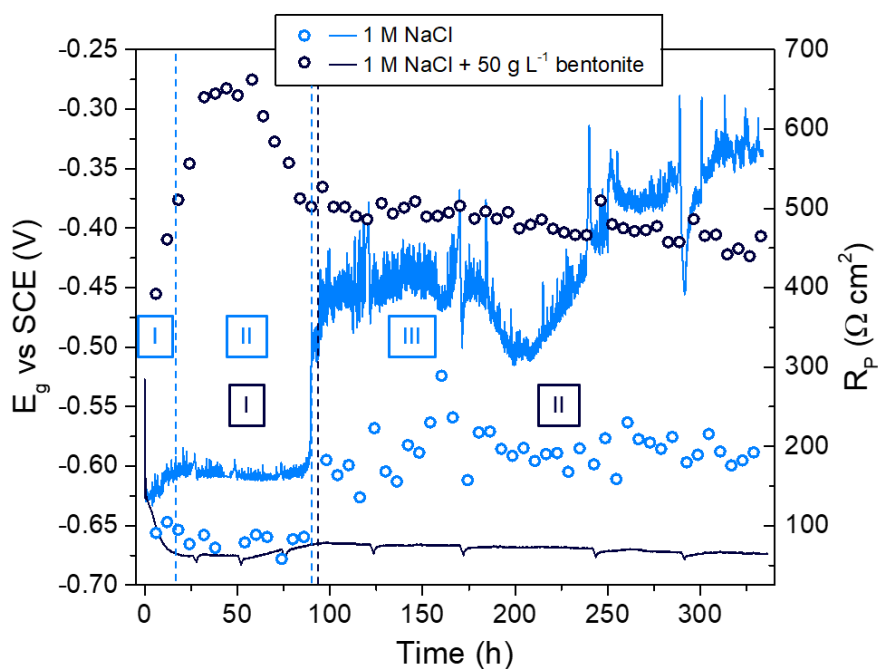


Figure 5.2 E_g and R_P values recorded on electrodeposited samples in 1 M NaCl or 1 M NaCl with 50 g L⁻¹ bentonite and plotted as a function of time.

presence of bentonite is shown in Figure 5.2. E_g values, after having been recorded versus the sat. Ag/AgCl electrode, were reported versus SCE.

In the absence of bentonite, the galvanic corrosion of the electrodeposited sample proceeded in three distinct phases. Phase I, between 0 and 18 hours, was associated an initial rapid decline in E_g , followed by a more gradual increase in E_g , likely due to buildup of an oxide film. R_P values in phase I were slightly elevated at between $91 \Omega \text{ cm}^2$ and $104 \Omega \text{ cm}^2$, which suggests that CS corrosion was slightly slower as the film formed on the surface. In phase II, spanning from 18 to 90 hours, the E_g of the electrodeposited sample stabilized at approximately -0.610 V , suggesting steady-state conditions at the CS surface. The phase II R_P values were confined in the range of $56 \Omega \text{ cm}^2$ to $88 \Omega \text{ cm}^2$. Throughout this time, the release of Fe^{2+} into the solution may have caused depletion of O_2 in the defect and magnetite formation at the base of the defect. However, the active corrosion indicates that this film was not protective. The corrosion rate did not change significantly during formation of this film because O_2 reduction on the Cu outside the defect was still occurring readily. In the transition to phase III, the E_g increased rapidly to approximately -0.450 V and R_P approximately doubled from 86 to $183 \Omega \text{ cm}^2$. This rapid increase in potential could be associated with partial passivation of the CS by a corrosion film, which decreased the rate of Fe^{2+} release. The higher R_P values in phase III indicated that the film provided some marginal corrosion protection, though due to the ongoing O_2 reduction on the Cu, the corrosion rate of the CS remained relatively high. The R_P values recorded during phase III were erratic and the E_g values were similarly unstable throughout phase III, exhibiting a brief drop to -0.505 V followed by a gradual increase to a plateau at -0.375 V and then another plateau at -0.335 V . This variability was attributed to periods in which fresh CS became exposed at the Cu/CS interface and was subsequently covered in new partially passive film growth. The rapid escalation in both E_g and R_P could also suggest a significant restructuring of a film that was formed during phases I and II.

Upon addition of bentonite to the electrochemical cell, the bentonite naturally settled atop the sample and was also allowed to fall into the hole. The recorded E_g and R_P values are plotted in Figure 5.2. The galvanic corrosion in the presence of bentonite proceeds in phases similar in nature to those in the absence of bentonite, though they differ in their duration and the E_g and R_P values achieved. In phase I, which spanned from 0 to 98 hours, the E_g initially trended in the negative direction, reaching a minimum of -0.672 V at 23 hours, where it stayed until 50 hours had passed.

The R_P initially trended upwards from $392 \Omega \text{ cm}^2$ to somewhat stabilize between $640 \Omega \text{ cm}^2$ and $662 \Omega \text{ cm}^2$ as the E_g was at its minimum. This indicated that the corrosion rate was decreasing due to the consumption of O_2 that was present in the bentonite slurry upon its addition to the cell. At a Cu:CS area ratio of 27:1, the majority of this O_2 consumption occurred on the Cu coating, including the Cu walls of the defect itself.

After reaching a minimum E_g and maximum R_P , the R_P began to fall, eventually reaching a steady-state value of $\sim 482 \Omega \text{ cm}^2$ for the duration of the experiment. As the R_P decreased significantly, the E_g shifted by only +7 mV to -0.665 V , where it also stabilized. The large increase in corrosion rate with only a small increase in E_g could have been caused by the onset of pitting, most likely at S-rich inclusions in the steel, as seen in previous galvanic coupling experiments in bentonite (chapter 4 of this thesis). The sluggish transport of the O_2 through the bentonite resulted in very high R_P values, even when the CS was actively corroding.

In phase II, from ~ 100 hours to the experiment termination, the E_g shifted by only -9 mV from its maximum at -0.665 V to -0.674 V after 336 hours – a high degree of stability. Similarly, R_P trended downward very slowly from $502 \Omega \text{ cm}^2$ at 102 hours to $465 \Omega \text{ cm}^2$ after 333 hours, with small transient increases occurring throughout phase II. The large R_P values throughout phase II in the presence of bentonite suggests that, even though the CS was actively corroding in both cases, this corrosion was occurring much more slowly in the presence of bentonite and changed very little over time. Over the course of the 14-day experiment, the CS was unable to form a partially passivating film at the very low E_g values achieved in the presence of bentonite, as evident in the lack of a sudden transition to a very positive E_g and an associated increase in R_P .

Brief upward and downward spikes observed in E_g measurements, both in the presence and absence of bentonite, were caused by the formation of short-lived radiolysis products due to X-ray exposure. The recovery of E_g after each event suggested that the system was not significantly affected by the X-ray exposure.

5.3.2 Corrosion Volume Analysis of Electrodeposited Samples by X-ray Micro-CT

Projections collected by X-ray micro-CT were consolidated into 3D reconstructions. The different phases of the sample: liquid/corrosion products, CS, and Cu, in the order of increasing X-ray attenuation, were differentiated by the greyscale value assigned according to the X-ray intensity at

the detector. The CS, with a density of 7.85 g cm^3 appeared a darker grey than the Cu, which had a density of 8.96 g cm^3 . The least dense phases: the liquid, the corrosion products, and in the case of the cold-sprayed sample, the Al_2O_3 particles embedded at the Cu/CS interface, appeared the darkest. In regions where the low-density phases were in contact, unambiguous differentiation between them could not be achieved with a high degree of confidence, though low-density phases were easily differentiated from the Cu and CS, and the Cu and CS were easily differentiated from each other. The “corroded volume” thus includes the liquid and any corrosion products from the very bottom of the hole to the level of the Cu/CS interface, less the volume of the drilled hole before corrosion.

The progression of corrosion within the defect of the electrodeposited sample in aerated 1 M NaCl is shown in Figure 5.3. In the absence of bentonite, the corrosion occurred rapidly; within 24 hours, the CS exhibited roughening at the base of the hole and some volume loss along the Cu/CS interface. The base of the hole continued to corrode fairly uniformly, resulting in an increase in the width and depth of the hole and the loss of the circular pattern (likely caused by the drilling of

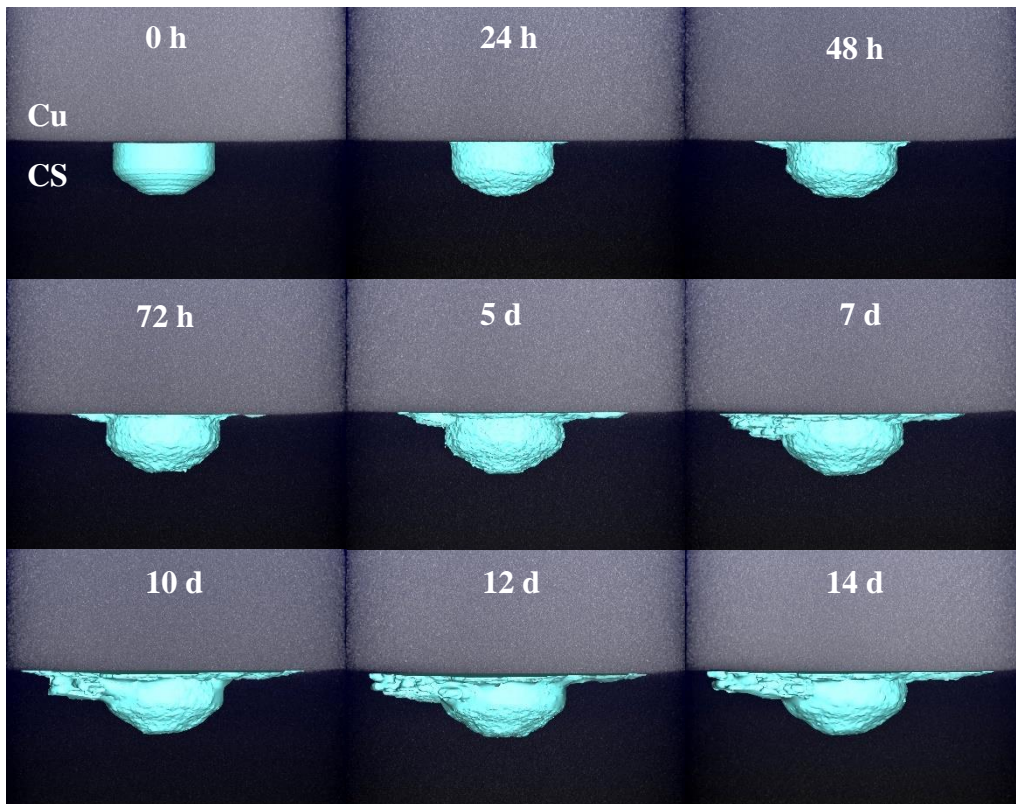


Figure 5.3 Vertical 2D cross sections through the centre of the drilled hole of an electrodeposited sample corroded in 1 M NaCl, obtained from 3D X-ray micro-CT data collected at indicated time points over the course of a corrosion experiment. The corroded volume below the Cu/CS interface was segmented and represented in turquoise.

the hole) that was initially present. Notably, the corrosion proceeded preferentially along the Cu/CS interface, extending laterally from the hole. After 5 days, at the site of what had been preferential interfacial corrosion, downward penetration into the CS had occurred as well. This pattern proceeded such that preferential corrosion along the interface would advance by some distance and then downward penetration would follow, widening the space below the corroded interface. The top-down view of the corroded interface, Figure 5.4, shows that the interfacial corrosion exhibited some preferential directionality. Interfacial corrosion initially showed a strong preference for the horizontal direction (left-to-right in Figure 5.4), aligned with grooves in the CS caused by machining of the surface before application of the coating. Interfacial corrosion proceeded in all directions, but at different rates, corroding fastest in the direction parallel to the largest machining grooves and more slowly perpendicular to those grooves.

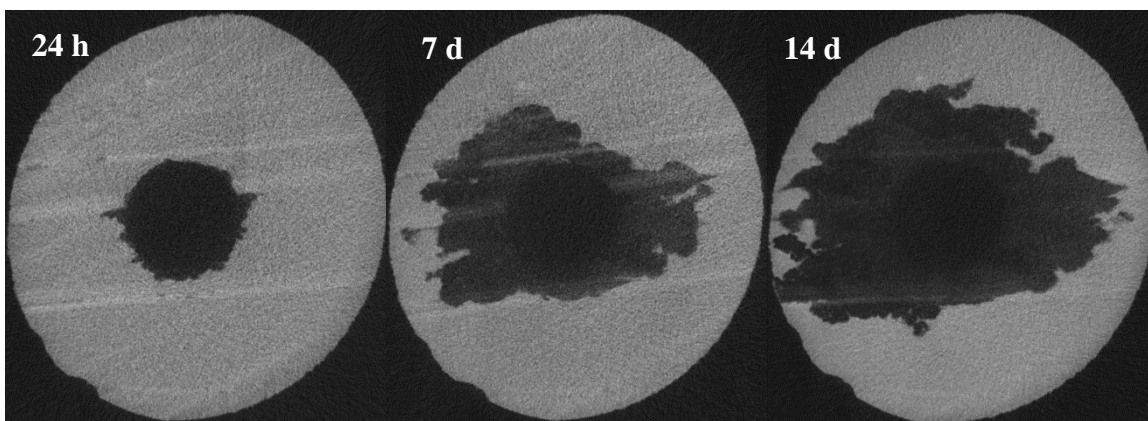


Figure 5.4 Horizontal 2D cross sections through the Cu/CS interface of an electrodeposited sample, obtained from 3D X-ray micro-CT data collected after 24 hours, 7 days, and 14 days of the sample's exposure to 1 M NaCl.

Figure 5.5 shows the corrosion within the artificial defect on an electrodeposited sample which was exposed to aerated 1 M NaCl and a layer of bentonite slurry. The extent of the corrosion was much lower than that in the absence of bentonite. In the period from 24 hours to 7 days, the only perceived corrosion was slight roughening along the base of the defect. Interfacial corrosion only began to outpace this general roughening at 7 days, at which point the first obvious sign of preferential interfacial attack was seen. This interfacial corrosion continued to grow outwards as the exposure time increased, but at a much lower rate than in the absence of bentonite. The interfacial corrosion in the absence of bentonite was very symmetric around the hole, showing no apparent preference for the direction of the machining grooves, as shown in the top-down view of the hole in Figure 5.6, though at such low corrosion rates, preference may be difficult to discern.

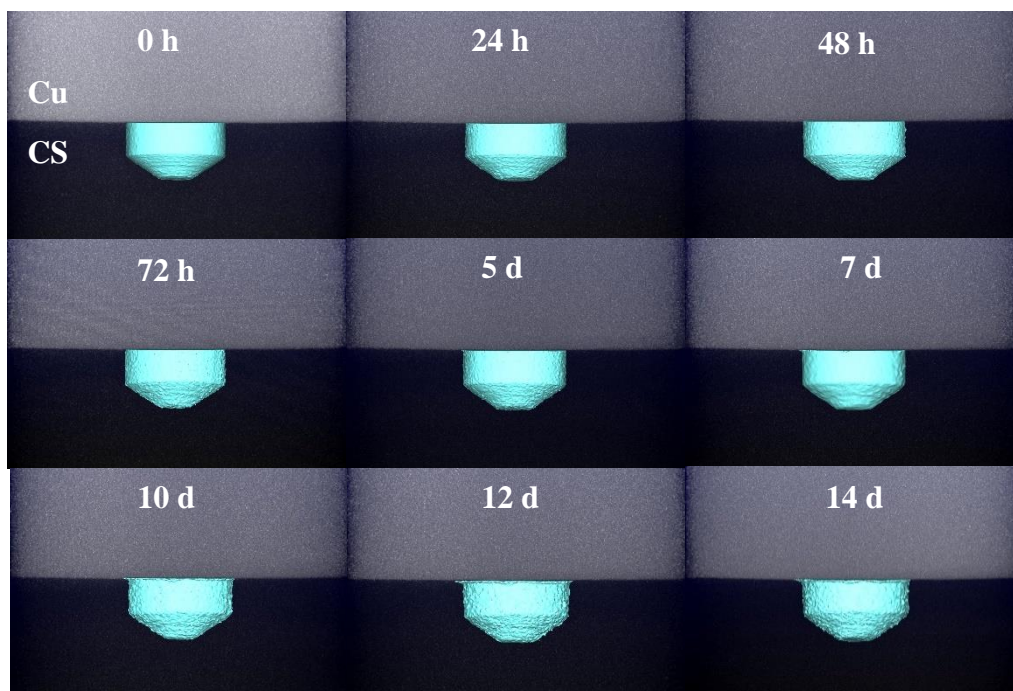


Figure 5.5 Vertical 2D cross sections through the centre of the drilled hole of an electrodeposited sample corroded in 1 M NaCl with 50 g L⁻¹ bentonite, obtained from 3D X-ray micro-CT data collected at indicated time points over the course of a corrosion experiment. The corroded volume below the Cu/CS interface was segmented and represented in turquoise.

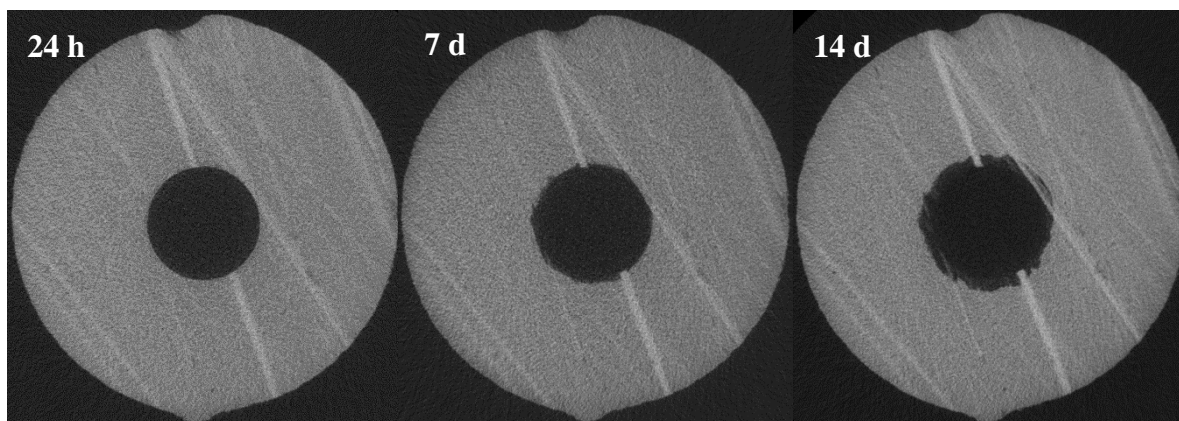


Figure 5.6 Horizontal 2D cross sections through the Cu/CS interface of an electrodeposited sample, obtained from 3D X-ray micro-CT data collected after 24 hours, 7 days, and 14 days of the sample's exposure to 1 M NaCl and 50 g L⁻¹ bentonite.

The corrosion volumes of the CS, as calculated in the Arivis software, are plotted in Figure 5.7 as a function of time. In both the presence and absence of bentonite, the corrosion volume increased linearly with time. This behaviour is consistent with previous work completed by Standish et al. [10], and confirms that the linear trend extends over time scales longer than 48 hours.

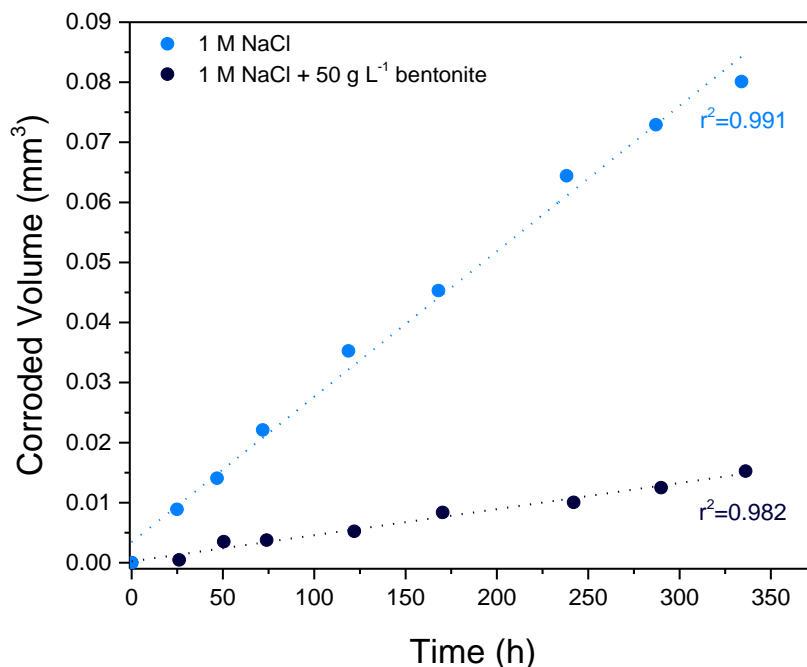


Figure 5.7 Corrosion volume (obtained through segmentation of X-ray micro-CT data) plotted as a function of time for electrodeposited samples corroded in the presence and absence of bentonite.

5.3.3 Electrochemistry Results for Cold Sprayed Cu-coated Samples

The E_g and R_p values recorded on cold sprayed samples are plotted in Figure 5.8 as a function of time. In the absence of bentonite, phase I involved rapid O_2 depletion, causing E_g to fall before stabilizing at -0.579 V until 46 hours had passed. This phase was also associated with R_p values which started at $\sim 77 \Omega \text{ cm}^2$ and fell slightly to $\sim 64 \Omega \text{ cm}^2$ as the E_g stabilized. The onset of phase II occurred after a brief drop in E_g followed by a near-recovery, after which the E_g entered a slow decline for the remainder of the experiment. This decline was also observed in the R_p values, indicating that the corrosion rate was slowly increasing over time. Notably, the cold-sprayed sample never achieved the partially passive phase III state achieved by the electrodeposited sample.

In cold-sprayed samples, the initial depletion of O_2 , as evident in the drop in E_g and high R_p , occurred more gradually in the presence of bentonite than in its absence. In the presence of bentonite, the drop in E_g led directly into steady-state conditions at -0.637 V and R_p values of $\sim 222 \Omega \text{ cm}^2$ which prevailed until ~ 115 hours. In phase III, E_g fell steadily from -0.637 V to -0.664 V after 334 hours. This slow decline in E_g was matched by a slow decline in corrosion rate, as shown by R_p values which began phase III at $222 \Omega \text{ cm}^2$ and increased to $243 \Omega \text{ cm}^2$. This

gradual decrease in E_g and the low corrosion rate was attributed to the gradual slowing of O_2 transport over time, perhaps due to the consumption of O_2 in the bentonite by oxidation of Fe^{2+} retained in the clay. Based on R_p values, the cold-sprayed samples exhibited higher corrosion rates both in the presence and the absence of bentonite, throughout the 14-day experiments.

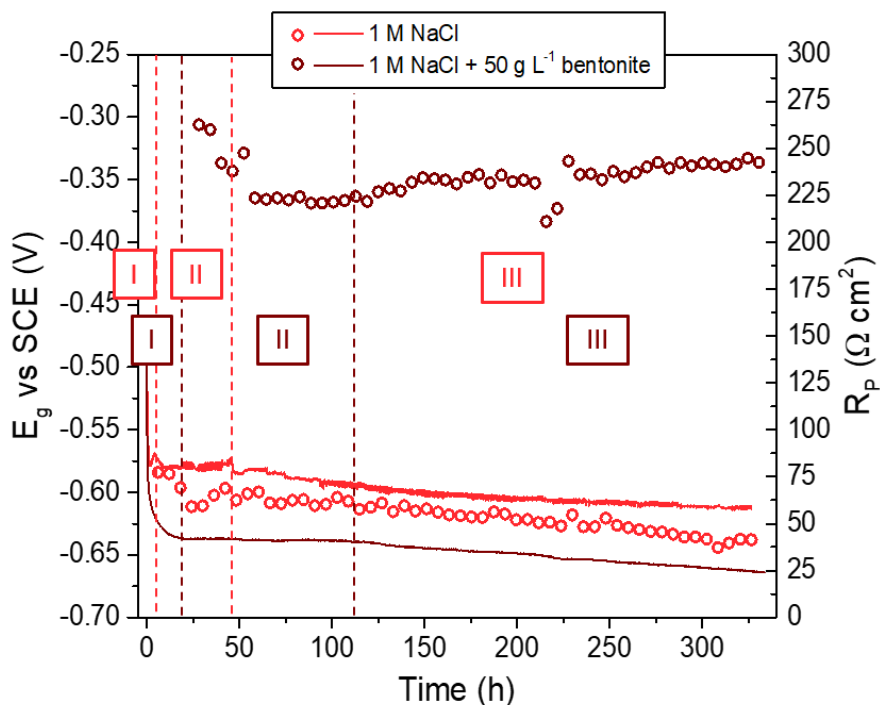


Figure 5.8 E_g and R_p values recorded on cold-sprayed samples in 1 M NaCl or 1 M NaCl with 50 g L⁻¹ bentonite and plotted as a function of time.

5.3.4 Corrosion Volume Analysis of Cold-sprayed Samples by X-ray Micro-CT

The corroded volumes of the cold-sprayed samples were segmented according to greyscale intensity in the same fashion as the electrodeposited samples. Cross sections of the segmented volumes of corrosion obtained in the absence of bentonite are shown in Figure 5.9. Roughening of the CS at the base of the defect was observed after 24 hours, along with a small amount of preferential interfacial corrosion beginning in some areas. As the exposure time increased, the CS at the base of the defect continued to roughen, while more rapid corrosion spread along the Cu/CS interface. The interfacial corrosion created a wedge of corroded volume between the Cu and CS, suggesting that the corrosion extended not only along the interface, but also that the aggressive conditions formed within the confined interfacial region contributed to some downward penetration into the CS in addition to outward propagation. Though visible interfacial corrosion

seemed to begin asymmetrically, after 72 hours, the interfacial corrosion propagated relatively symmetrically outward from the hole, suggesting that the Cu/CS interface was relatively uniformly reactive.

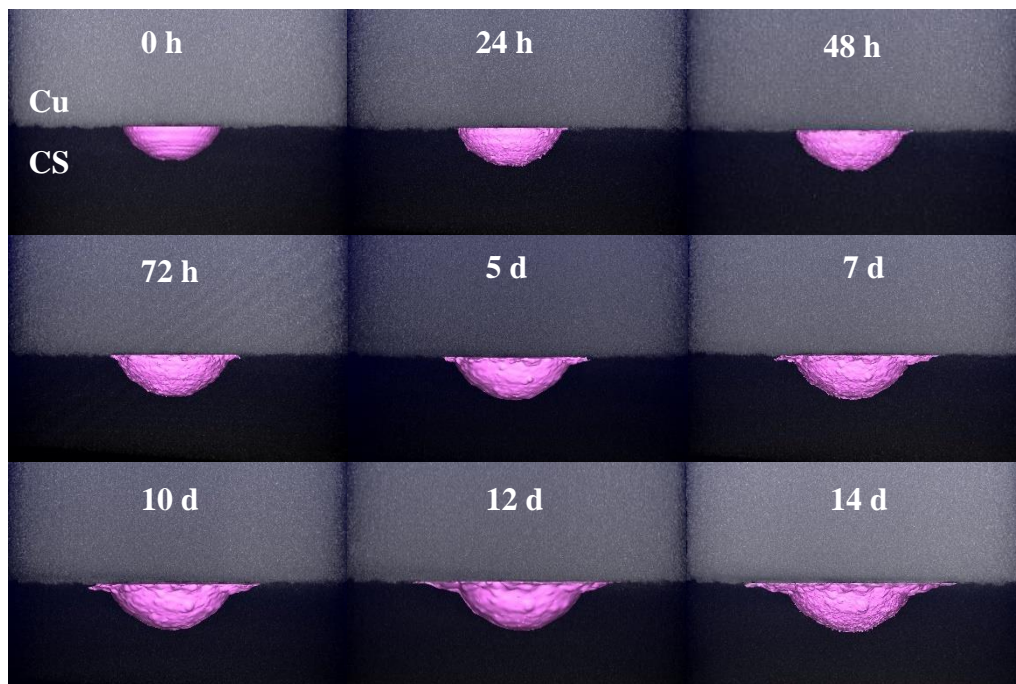


Figure 5.9 Vertical 2D cross sections through the centre of the drilled hole of a cold-sprayed sample corroded in 1 M NaCl, obtained from 3D X-ray micro-CT data collected at indicated time points over the course of a corrosion experiment. The corroded volume below the Cu/CS interface was segmented and represented in pink.

The interfaces of the cold-sprayed samples were much more uneven as a result of grit-blasting the CS before application of the Cu coating, which served to improve coating adhesion by increasing the CS surface roughness and thus surface area [14]. Interfacial cross sections of the sample exposed only to 1 M NaCl are shown in Figure 5.10. This roughness is evident in the mottled interface, displaying Cu areas (very light grey) where the coating extended below the cross-sectional plane, the CS substrate (grey), and alumina particles (dark grey) embedded at the interface present in the same plane. The interfacial cross sections show some patches of Cu overlaying the corroded region; these patches of Cu did not exhibit significant corrosion over the course of the 14-day experiment as their size and shape remained unchanged. This lack of corrosion is consistent with the nobility of Cu and the cathodic protection conferred by the galvanic couple. In fact, the presence of these Cu “splats” at the interface seemed to have encouraged some preferential CS corrosion in their immediate vicinity due to stronger galvanic effect and interfacial stresses, as opposed to propagating indiscriminately across the interface. The interfacial texture of

the cold-sprayed samples was evenly distributed around the drilled hole, so the corrosion propagated outward from the hole in all directions, showing no large-scale directional preference.

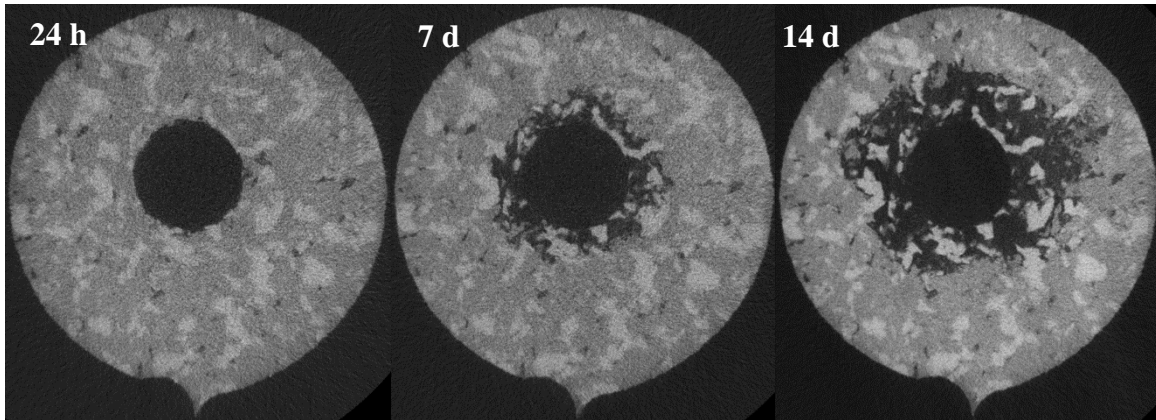


Figure 5.10 Horizontal 2D cross sections through the Cu/CS interface of a cold-sprayed sample, obtained from 3D X-ray micro-CT data collected after 24 hours, 7 days, and 14 days of the sample's exposure to 1 M NaCl.

The cold-sprayed sample exposed to bentonite, Figure 5.11, exhibited some minor roughening over the course of the 14-day experiment as well as a small amount of corrosion along the Cu/CS interface. The presence of bentonite limited the extent of corrosion significantly, in terms of limiting both interfacial corrosion and penetration depth.

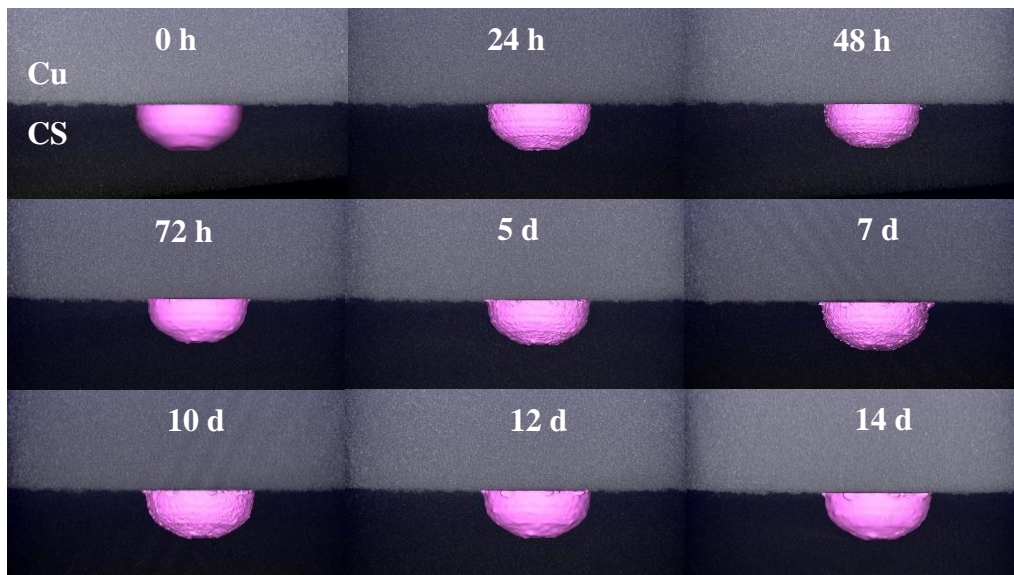


Figure 5.11 Vertical 2D cross sections through the centre of the drilled hole of a cold-sprayed sample corroded in 1 M NaCl with 50 g L^{-1} bentonite, obtained from 3D X-ray micro-CT data collected at indicated time points over the course of a corrosion experiment. The corroded volume below the Cu/CS interface was segmented and represented in pink.

The mottled Cu/CS interfacial cross sections, Figure 5.12, show almost no interfacial corrosion after 24 hours of exposure to 1 M NaCl and bentonite clay. However, by day 7, interfacial corrosion around the hole was obvious and slightly more extensive than that observed in the electrodeposited case. This corrosion proceeded in tendrils around the Cu splats at the interface in a fashion similar to the corrosion under bentonite-free conditions. After the passage of 14 days, the interfacial corrosion had extended outward from the hole, showing little directional preference.

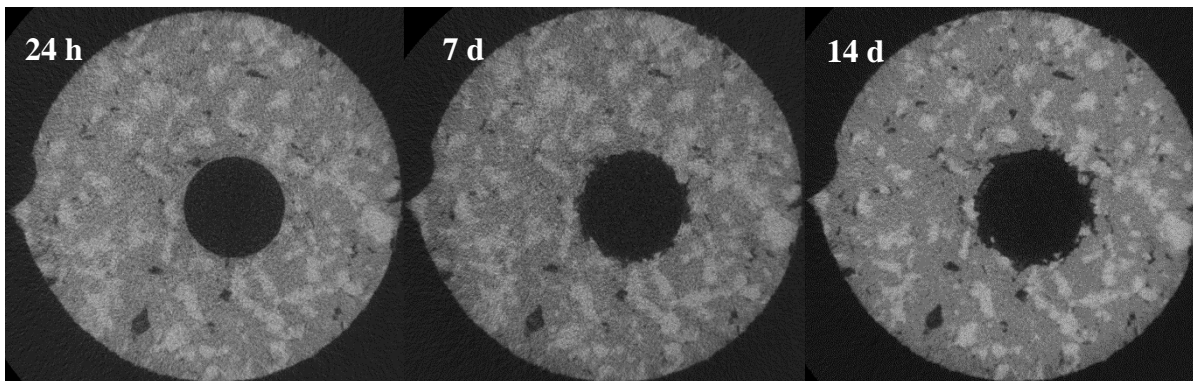


Figure 5.12 Horizontal 2D cross sections through the Cu/CS interface of a cold-sprayed sample, obtained from 3D X-ray micro-CT data collected after 24 hours, 7 days, and 14 days of the sample's exposure to 1 M NaCl and 50 g L⁻¹ bentonite.

The corroded volume of the cold sprayed samples was plotted as a function of time in Figure 5.13, including two runs of cold sprayed samples not exposed to bentonite. As in the case of the electrodeposited samples, the corroded volume of the cold sprayed samples increased linearly with time in both the presence and absence of bentonite. The first run in the absence of bentonite became compromised after 7 days, as an undesired corrosion front from the sample exterior became indistinguishable from the desired corrosion front propagating from the hole interior, though prior to 7 days, the increase in corrosion volume exhibited a strong linear trend. Though both samples corroded in the absence of bentonite exhibited a much steeper increase in corroded volume than in the presence of bentonite, the first run was markedly steeper than the second. This difference can be attributed to variations in sparging rate of each experiment, where the sparging rate of the first experiment was higher than the second, thus leading to a higher rate of corrosion.

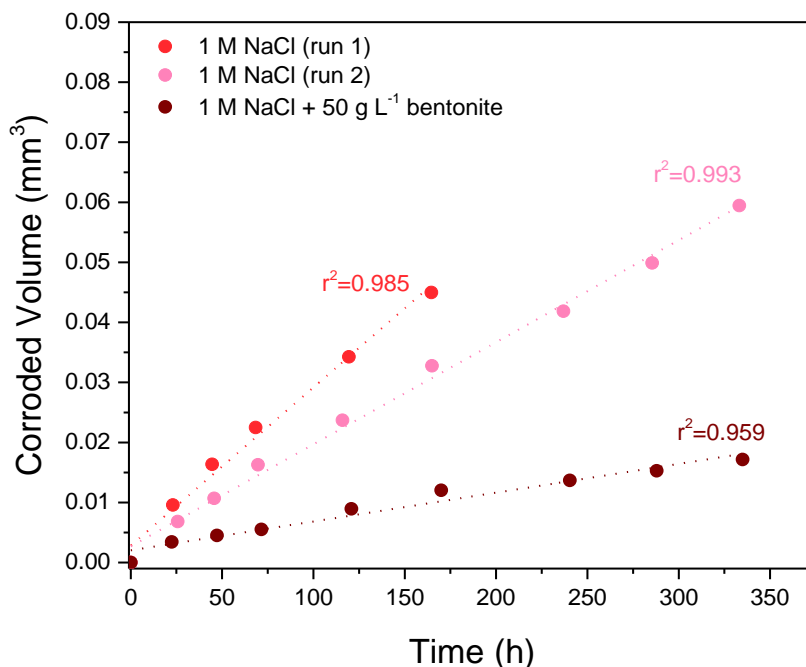


Figure 5.13 Corrosion volume (obtained through segmentation of X-ray micro-CT data) plotted as a function of time for cold-sprayed samples corroded in the presence and absence of bentonite.

5.3.5 Surface Analysis of Vertical Cross Sections

After 14 days of corrosion, samples were cast in epoxy and cross-sectioned in a plane perpendicular to the Cu/CS interface before undergoing surface analysis. Optical images of an electrodeposited sample corroded in the absence of bentonite, Figure 5.14, show the presence of yellow Fe-(oxyhydr)oxide deposits within the hole and a dark film in some regions at the base of the hole and uniformly coating the interfacial regions. The coverage of the base of the hole by the orange deposits appeared patchy; however, a closer inspection of a corroded region extending behind the plane of the cross section revealed very uniform coverage by these deposits. SEM/EDX

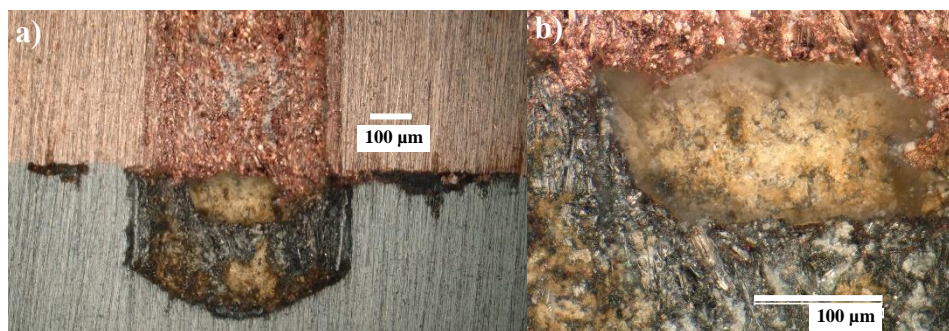


Figure 5.14 a-b) Optical micrographs of an electrodeposited sample cross sectioned perpendicular to the Cu/CS interface after corrosion in aerated 1 M NaCl.

analysis of a sample corroded under the same conditions, but whose drilled hole was injected with epoxy before cross sectioning, Figure 5.15, showed an oxide film with a thickness on the order of tens of micrometres preserved at the base of the hole, based on the layer of slightly enriched Fe and O within the hole. The interfacial region was also found to contain enriched O signal due to the presence of an oxide film. The roughness observed on the Cu walls of the drilled hole in Figure 5.14 could indicate that some Cu corrosion occurred over the course of the experiment, though X-ray micro-CT analysis of the Cu walls of a similar sample showed little change in roughness from the initial state of the sample to the final state after 14 days.

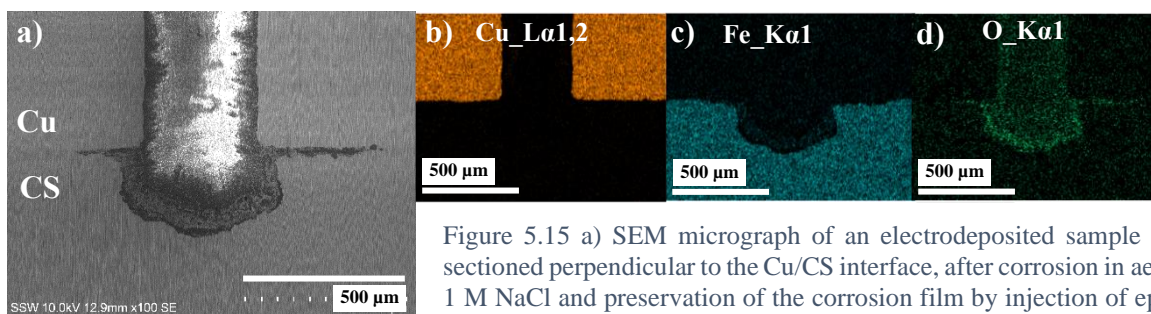


Figure 5.15 a) SEM micrograph of an electrodeposited sample cross sectioned perpendicular to the Cu/CS interface, after corrosion in aerated 1 M NaCl and preservation of the corrosion film by injection of epoxy, with associated EDX maps for b) Cu, c) Fe, and d) O signals.

Raman spectroscopy of the sample cross section, Figure 5.16, revealed that the yellow corrosion product within the hole was composed of lepidocrocite, given the sharp peaks at 252 cm^{-1} and 383 cm^{-1} [15] in spectra obtained from areas 1 and 2. Area 2 exhibited a small peak for magnetite at 670 cm^{-1} [16], suggesting the presence of a compact underlying film. Highly crystalline lepidocrocite was found collected atop the Cu coating, in areas 5 and 6. In the interfacial region, area 3, no lepidocrocite was found and a weak signal at 721 cm^{-1} indicated the presence of maghemite [16]. The Cu walls of the coating defect, area 4, gave characteristic signals for Cu_2O : a strong, broad peak at 613 cm^{-1} with a shoulder at 526 cm^{-1} , and a very strong peak at 150 cm^{-1} [17]. This is consistent with the visual assessment of corrosion damage to the Cu within the defect.

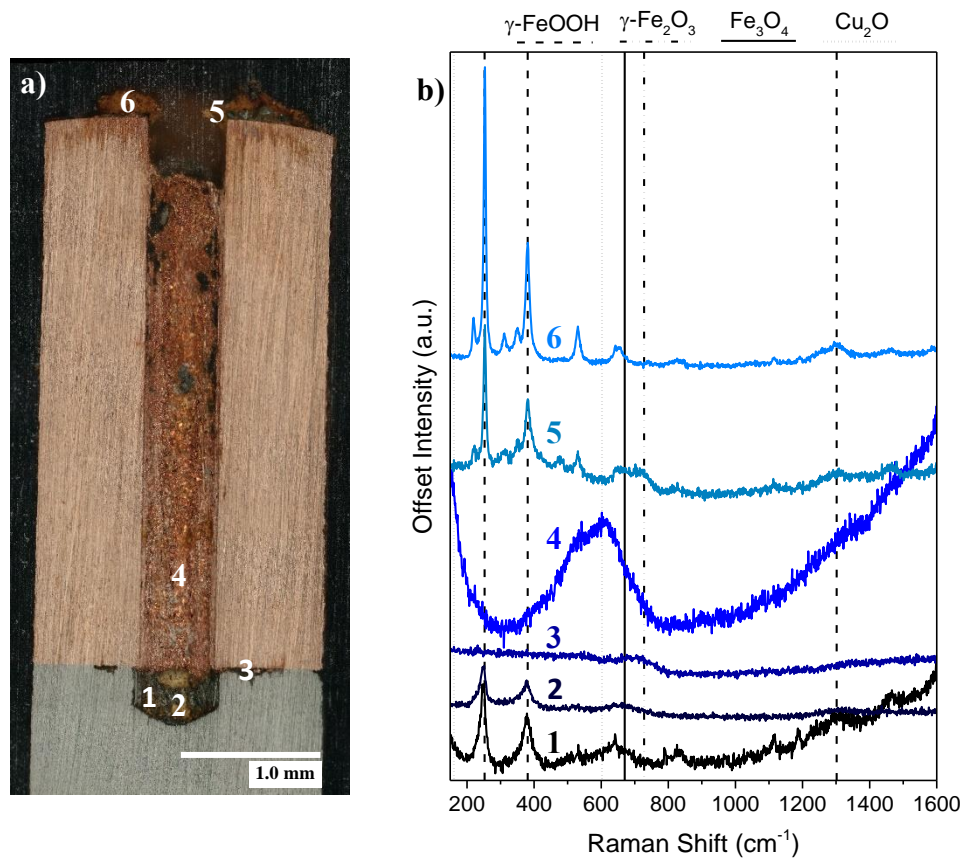


Figure 5.16 a) Optical micrograph of an electrodeposited sample, cross sectioned perpendicular to the Cu/CS interface after corrosion in aerated 1 M NaCl and b) Raman spectra obtained at the points indicated on the optical image.

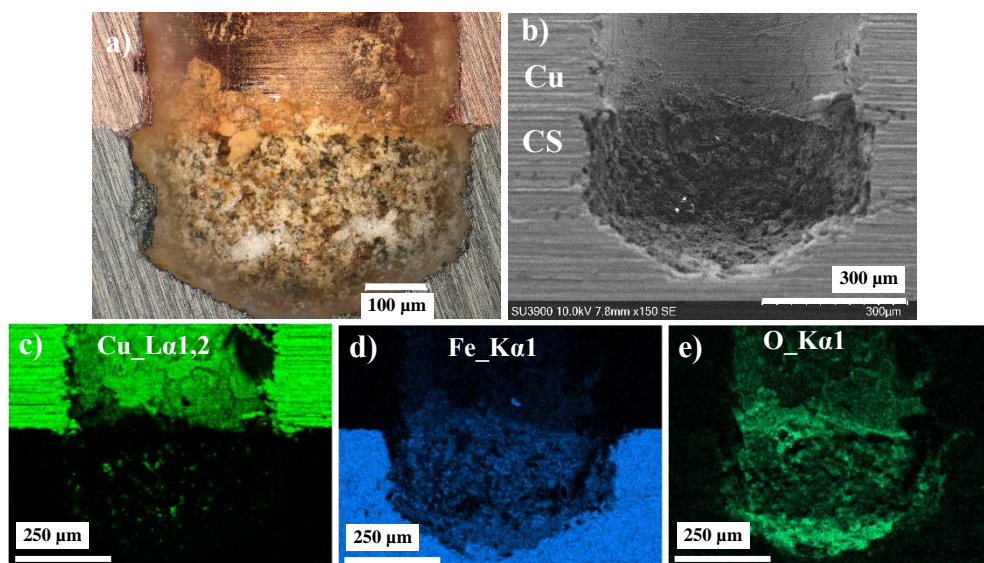


Figure 5.17 a) Optical micrograph and b) SEM micrograph of an electrodeposited sample cross-sectioned perpendicular to the Cu/CS interface, after corrosion in aerated 1 M NaCl with 50 g L⁻¹ bentonite, with associated EDX maps for c) Cu, d) Fe, and e) O signals.

An optical image of the electrodeposited sample corroded in the presence of bentonite, Figure 5.17a, revealed the CS at the base of the drilled hole to be uniformly covered in yellow-orange corrosion deposits. SEM and EDX analysis of the hole, Figure 5.17b-e, confirm the presence of Fe-(oxyhydr)oxides within the hole. Notably, the signals for Fe and O extended above the Cu/CS interface, suggesting that corrosion products had deposited a short distance up the Cu wall, but no oxides were observed to have deposited atop the Cu coating.

Raman analysis of the sample corroded in bentonite, Figure 5.18, showed that the corrosion product within the hole contained a variety of oxide and oxyhydroxide species. The most abundant species was lepidocrocite, as shown by the strong peaks at 247 cm^{-1} , 383 cm^{-1} , and 1308 cm^{-1} in areas 2, 3, 4, and 5. Area 3 was found to contain goethite, identified by the greater relative strength of the peak at 383 cm^{-1} . The preference for formation of goethite and lepidocrocite tends to favour goethite when $[\text{O}_2]$ is low [18], which is consistent with the lower E_g and i_g recorded in the presence of bentonite. Signals at 652 cm^{-1} and 725 cm^{-1} from areas 1, 3, 4, and 5 were characteristic of

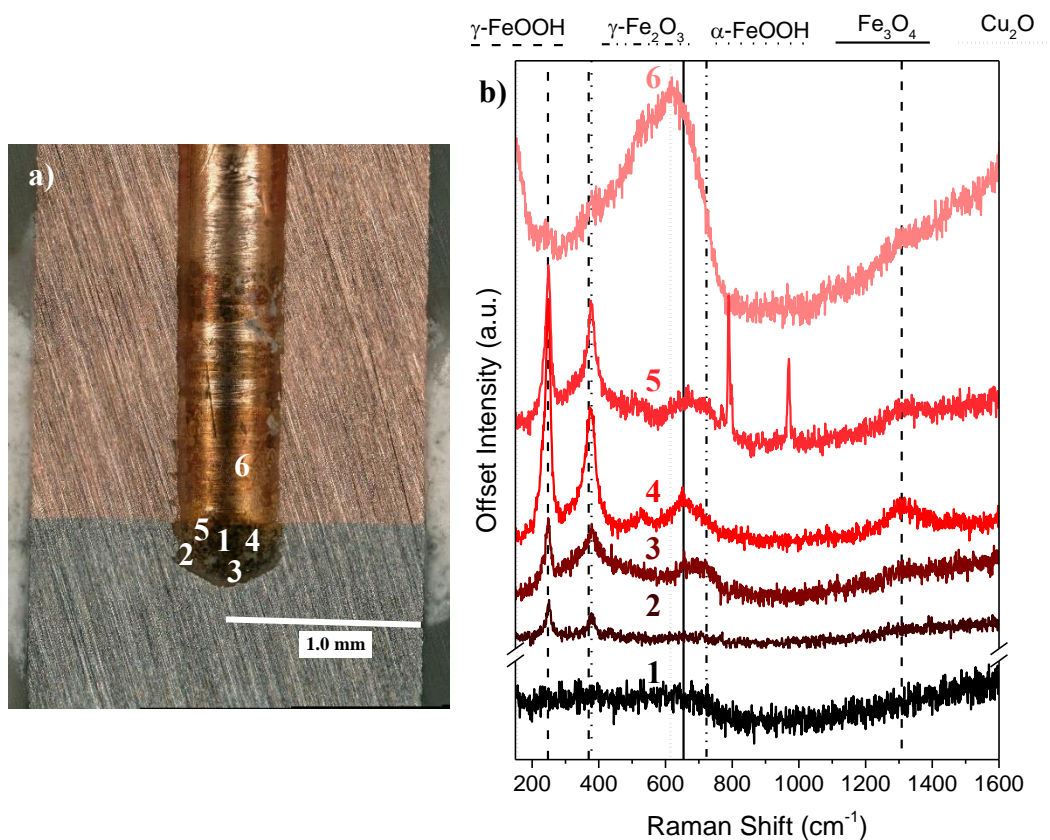


Figure 5.18 a) Optical micrograph of an electrodeposited sample, cross-sectioned perpendicular to the Cu/CS interface after corrosion in aerated 1 M NaCl with 50 g L^{-1} bentonite, and b) Raman spectra acquired at the points indicated on the optical image.

magnetite and maghemite. Previous pH measurements of bentonite showed that the bentonite tended to remain slightly alkaline, at a pH of ~ 8.6 , after exposure to corroding Cu and CS. These alkaline conditions favour magnetite formation and conversion to maghemite [19]. Peaks at 792 cm^{-1} and 970 cm^{-1} in area 5 were attributed to symmetric stretching of Si-O-Si linkages and symmetric stretching of terminal Si-O⁻ units, respectively [20]. These signals likely were caused by small bentonite particles incorporated into the corrosion film. Similar to the bentonite-free case, Raman spectra recorded on the Cu wall, area 6, gave peaks for Cu₂O, however, weak signals at $\sim 250\text{ cm}^{-1}$ and $\sim 380\text{ cm}^{-1}$ suggest that lepidocrocite had deposited in small amounts on the Cu walls. No Fe-(oxyhydr)oxide signals were obtained from the top of the Cu coating, which suggests that the bentonite acted as a barrier to transport of aqueous ferrous or ferric species out of the defect.

5.4 Discussion

The presence of bentonite slurry produced very benign conditions for CS corrosion, as evident in significantly more negative E_g values and higher R_P values; this was observed both when the Cu coating was applied by electrodeposition and by cold-spray methods. In the absence of bentonite, oxidizing conditions allowed the CS to rapidly form a protective film. At the very negative E_g values observed in the presence of bentonite, the CS failed to passivate, though its active corrosion was still very slow compared to the passive corrosion behaviour in the absence of bentonite. In the Cu/CS galvanic couple, a large fraction of O₂ reduction occurred on the Cu coating and a smaller fraction occurred on the CS; the bentonite acted as a barrier to O₂ diffusion, lowering the rate of O₂ reduction on both the Cu and CS. For the cold sprayed samples, bentonite also caused a sizable negative shift in E_g and slower corrosion, but the absence of bentonite did not result in any passivation of the CS. Rather, the corrosion rate in the absence of bentonite trended steadily upward over the course of the experiment. In work done by Standish et al., this transition to partial passivity was found to occur on cold sprayed samples under similar conditions, though its onset appeared stochastic in nature, occurring after 20 days in one instance and 1.2 hours in another [21]. Thus, the absence of the transition in this 14-day experiment does not preclude the possibility that, given addition time, the transition could occur under these conditions.

The presence of lepidocrocite at the base of the defect in both the presence and absence of bentonite was indicative of the presence of O₂ within the defect, though the emergence of goethite suggests

that the $[O_2]$ was lower when bentonite was present. In the absence of bentonite, strong signals for lepidocrocite atop the Cu suggested that a significant amount of $Fe(OH)^+$ was transported from sites of lower $[O_2]$ conditions within the defect to be oxidized in the higher $[O_2]$ areas prevailing in the bulk solution and deposited on the Cu coating. Maghemite, which can form from either the dehydroxylation of lepidocrocite at high temperature or the oxidation of magnetite [19], was found in the interfacial region. Due to the constrained geometry within the interfacial region and the resulting decrease in pH, active corrosion of the CS was likely more favourable than formation of magnetite, resulting in a very thin and unstable magnetite film which quickly converted to maghemite.

X-ray micro-CT revealed that the CS at the base of the drilled hole corroded preferentially along the Cu/CS interface in all cases (bentonite or bentonite-free, electrodeposited or cold-sprayed). The Arivis software was used to take horizontal linear measurements across the Cu/CS interface and vertical linear measurements from the interface to the base of the hole, at 10° intervals. These two-dimensional corroded distances were plotted as a function of time in Figure 5.19. The corrosion proceeded interfacially much more rapidly than downward penetration in the absence of bentonite, and marginally more rapidly in the presence of bentonite. The machining of the CS

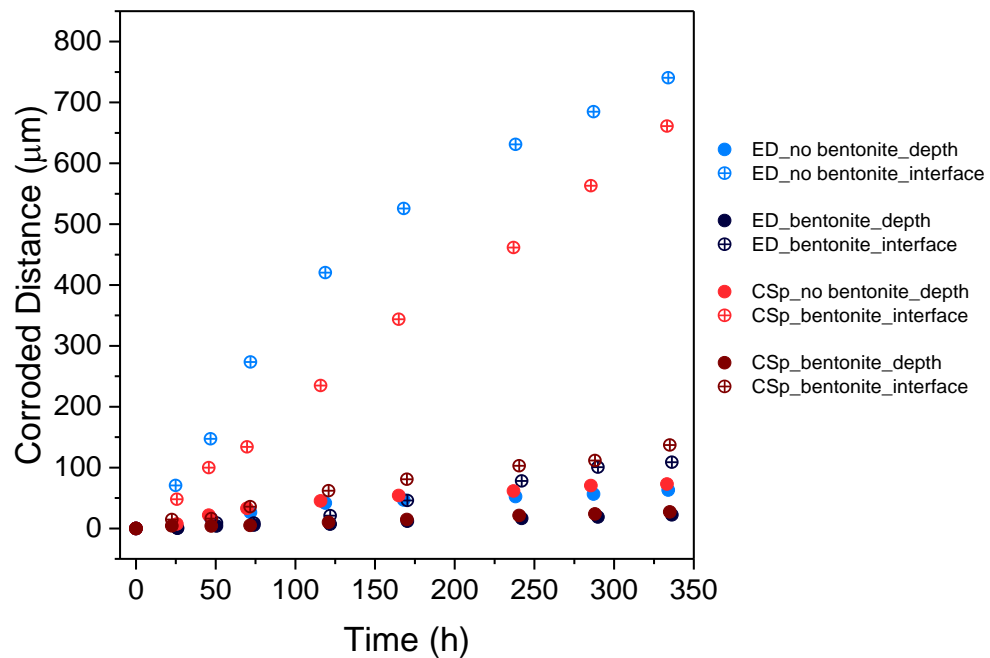


Figure 5.19 Average corroded distance across the Cu/CS interface and average corroded depth from the Cu/CS interface to the bottom of the hole, obtained from X-ray micro-CT data on cold sprayed (CSp) and electrodeposited (ED) samples in both the presence and absence of bentonite, and plotted as a function of time.

before application of the Cu coating contributed to the rapid interfacial corrosion of electrodeposited samples. Machining of mild steel has been shown to cause plastic deformation and local microstructural changes which increase its susceptibility to corrosion [22]. Grit-blasting of the CS before application of the cold sprayed Cu coating created compressive residual stress and plastic deformation of the CS surface [23], resulting in preferential interfacial corrosion in the cold-sprayed samples as well. Due to the extreme roughness of the cold sprayed interface, the corrosion could not proceed in a direct lateral fashion, but rather propagated under and around the Cu splats. For this reason, the two-dimensional analysis of the Cu/CS interface likely slightly underestimated the full extent of interfacial corrosion in the cold sprayed sample. This, in addition to the lower sparging rate, contributed to the lower interfacial corrosion rate of the cold sprayed sample in the absence of bentonite.

The preference for interfacial corrosion was dampened in the presence of bentonite due to the lower overall corrosion rate and the alkalinity of the bentonite, both of which contributed to the prevention of buildup of local acidity at confined interfacial regions. Slightly more rapid interfacial corrosion of the cold sprayed sample was indicative of lower quality adhesion of the cold sprayed coating compared to the electrodeposited coating [5, 24].

The rate of penetration downward into the CS was generally very similar between the cold-sprayed and electrodeposited samples, both in the presence and absence of bentonite, which is consistent with the fact that the only major differences between these two samples were CS surface preparation and Cu coating application technique. The susceptibility of the bulk CS to downward-penetrating corrosion should be similar between the two sample types, since the steel was the same in all cases.

The overall corrosion rates were determined based on the rates of increase of corroded volume, Figure 5.20. Given the density of 7.85 g cm^{-3} for A516 gr. 70 carbon steel, and the Fe content of 97% by weight, the corroded volume was converted to Fe mass loss by Equation 5.2,

$$m_{\text{Fe}} = C_{\text{Fe}} \times d_{\text{A516}} \times V_{\text{corroded}} \quad (5.2)$$

where m_{Fe} is the area-normalized mass of Fe lost due to corrosion (in g cm^{-2}), C_{Fe} is equal to 0.98 and is the fraction of Fe in the CS, d_{A516} is equal to 7.85 g cm^{-3} , and is the density of A516 gr. 70 carbon steel, and V_{corroded} is the corroded volume (in cm^3). Extraction of the slope of mass loss vs.

time plots for each sample (cold-sprayed and electrodeposited, in the presence and absence of bentonite), allowed for the determination of the corrosion rate. The presence of bentonite suppressed the corrosion rate by over 80% in both the electrodeposited and cold-sprayed samples. The corrosion rates were slightly higher in the cold-sprayed samples, both in the absence and presence of bentonite, as a result of lower coating adhesion and the resulting preferential interfacial corrosion, though there was some variability due to sensitivity of the system to the sparging rate.

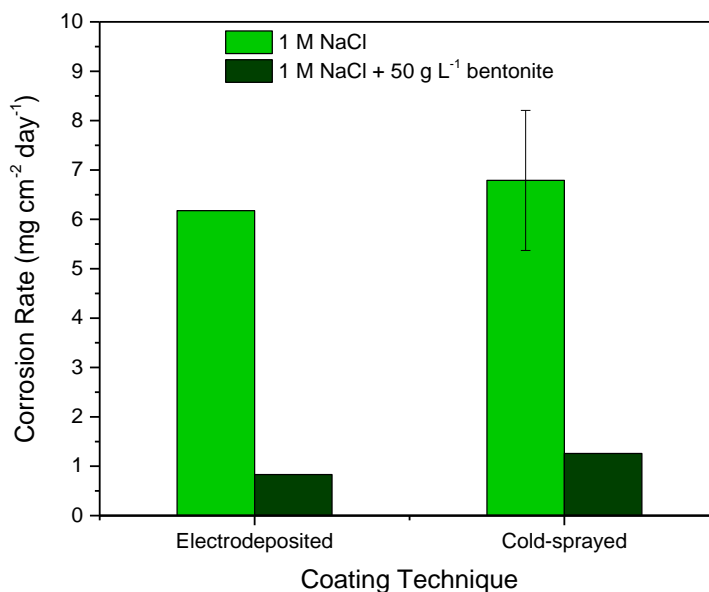


Figure 5.20 Corrosion rates of electrodeposited and cold-sprayed samples in 1 M NaCl, with and without bentonite.

5.5 Conclusions

In the scenario in which the Cu-coated CS used nuclear fuel container suffered a through-coating defect, galvanically accelerated corrosion of the CS substrate would be theoretically possible. Cu-coated CS samples with small holes drilled through the coatings (to simulate defects) were galvanically corroded, and OCP and LPR measurements coupled with *in situ* X-ray micro-CT and post-mortem Raman spectroscopy and SEM/EDX were used to evaluate the corrosion. The results provided a comparison between the corrosion susceptibility of the cold sprayed Cu/CS interface and the electrodeposited Cu/CS interface, relating to the different surface treatments of the CS prior to coating application. Additionally, due to the intended enclosure of the UFC in a compacted bentonite clay buffer box, the exposure of the samples to bentonite slurry was performed to provide

valuable preliminary information about the effect of bentonite clay on galvanic corrosion at a through-coating defect.

- In the absence of bentonite, the CS demonstrated the ability to form a protective oxide barrier, though the transition to such a state was rapid and stochastic in nature. Formation of a protective film was associated with higher R_P values, though the linear increase in corrosion volume suggests that the protection was not effective, and asymmetric growth of the corroded volume suggests that the film coverage was not uniform. The oxide layer, when cross-sectioned and viewed under SEM, was observed to be thick but porous, and composed largely of lepidocrocite.
- In the presence of bentonite, the very negative E_g values and high R_P values suggested that the bentonite was acting as a barrier to O_2 diffusion to both the Cu and the CS surfaces. Such benign conditions were also reflected in the X-ray micro-CT analysis, which showed minimal corrosion damage and >80% reduction in corrosion rates compared to bentonite-free conditions. The bentonite also acted as a barrier to transport of aqueous ferric and ferrous species, which allowed the formation of corrosion products on the CS at the base of the hole but prevented their upward transport and deposition atop the Cu coating.
- In all cases, the Cu/CS interface was more susceptible to corrosion than the bulk CS, due to residual stress and plastic deformation induced by CS surface modification before coating application. The lower adhesion of cold-sprayed coatings made the Cu/CS interface of cold-sprayed samples slightly more susceptible to corrosion than that of electrodeposited samples (though limitations of the 2D measurement and variation in sparging rate made this effect difficult to quantify).
- The machining grooves at the interface of electrodeposited samples caused some preference for interfacial corrosion parallel to those lines, due to introduction of residual stress from plastic deformation. In cold-sprayed samples, interfacial corrosion occurred symmetrically around the drilled hole and corrosion propagated preferentially around Cu splats at the Cu/CS interface. When interfacial corrosion was less extensive, as in the presence of bentonite, corrosion occurred symmetrically around the hole in both electrodeposited and cold-sprayed samples.

This work demonstrated the effectiveness of bentonite slurry to create benign corrosion conditions in a through-coating defect. Further work should investigate if a Cu/CS galvanic couple can be established in compacted bentonite, given the geometry of a through coating defect, and how the presence of compacted bentonite affects the corrosion rate of the CS substrate.

5.6 References

1. F. King, D. S. Hall, P.G. Keech, *Corros. Eng. Sci. Techn.* **2017**, *52*, 25-30.
2. C. Lilja *Corrosion calculations report for the safety assessment SR-Site*; TR-10-66; SKB: 2010.
3. F. King, *Corrosion* **2013**, *69*, 986-1011.
4. F. King *Durability of High Level Waste and Spent Fuel Disposal Containers – an overview of the combined effect of chemical and mechanical degradation mechanisms*; 7697/TR/03 Appendix C; Quintessa: 2016.
5. C. H. Boyle, S. A. Meguid, *Nucl. Eng. Des.* **2015**, *293*, 403-412.
6. J. R. Scully, D. Feron, H. Hanninen *Review of the NWMO Copper Corrosion Program*; NWMO-TR-2016-11; Nuclear Waste Management Organization: Toronto, Canada, August 2016, 2016; p 31.
7. T. Standish, J. Chen, R. Jacklin, P. Jakupi, S. Ramamurthy, D. Zagidulin, P. Keech, D. Shoesmith, *Electrochim. Acta* **2016**, *211*, 12.
8. D. Poirier, J.-G. Legoux, P. Vo, B. Blais, J. D. Giallonardo, P. G. Keech, *J Therm. Spray Tech.* **2019**, *28*, 444-459.
9. M. Fukumoto, H. Terada, M. Mashiko, K. Sato, M. Yamada, E. Yamaguchi, *Mater. Trans.* **2009**, *50*, 1482-1488.
10. T. Standish, D. Zagidulin, S. Ramamurthy, P. Keech, D. Shoesmith, J. Noël, *Geosciences* **2018**, *8*, 1-14.
11. T. E. Standish, D. Zagidulin, S. Ramamurthy, P. G. Keech, J. J. Noël, D. W. Shoesmith, *Corros. Eng. Sci. Techn.* **2017**, *52*, 65-69.
12. M. V. Villar *MX-80 Bentonite. Thermo-Hydro-Mechanical Characterisation Performed at CIEMAT in the Context of the Prototype Project*; CIEMAT/DIAE/54540/2/04; Ciemat: Madrid, Spain, 2004.
13. W. Li, C. Li, H. Liao, *J. Therm. Spray. Technol.* **2006**, *15*, 206-211.
14. M. Vijay, A. Tieu, W. Yan, B. Daniels, M. Xu, Enhancing the adhesion strength of cold gas dynamic sprayed coatings by preparing the substrates with the high-frequency pulsed waterjet. In *WJTA-IMCA Conference and Expo*, New Orleans, United States, 2015.
15. A. Liu, J. Liu, B. Pan, W. Zhang, *RSC Adv.* **2014**, *4* (101), 57377-57382.
16. M. Hanesch, *Geophys. J. Int.* **2009**, *177* (3), 941-948.

17. G. Niaura, *Electrochim. Acta* **2000**, 45 (21), 3507-3519.
18. C. Rémazeilles, Ph. Refait, *Corros. Sci.* **2007**, 49, 844-857.
19. R. M. Cornell, U. Schwertmann, *The Iron Oxides: Structure, Properties, Reactions, Occurrences and Uses*. 2nd ed.; WILEY-VCH Verlag GmbH & Co. KGaA: Weinheim, Germany, 2003.
20. B. Karmakar, Fundamentals of Glass and Glass Nanocomposites. In *Glass Nanocomposites*, William Andrew Applied Science Publishers: Norwich, United States, 2016; pp 3-53.
21. T. E. Standish. Galvanic corrosion of copper-coated carbon steel for used nuclear fuel containers. The University of Western Ontario, London, Canada, 2019.
22. M. Prakash, S. Shekhar, A. P. Moon, K. Mondal, *J. Mater. Process. Technol.* **2015**, 219, 70-83.
23. K. Poorna Chander, M. Vashista, K. Sabbiruddin, S. Paul, P. P. Bandyopadhyay, *Mater. Des.* **2009**, 30, 2895-2902.
24. R. Fernández, D. MacDonald, A. Nastić, B. Jodoin, A. Tieu, M. Vijay, *J. Therm. Spray. Technol.* **2016**, 25, 1577-1587.

6. Conclusions and Future Work

6.1 Conclusions

In this work, the corrosion behaviour of CS in the Cu/CS galvanic couple was investigated under conditions that are relevant to the DGR environment near the Cu-coated used fuel container. The investigation of this system was vital in the assessment of the risk of container failure due to an undetected defect through the Cu coating and possible galvanic corrosion. In such a scenario, the Cu:CS area ratio would be large, and thus a unique setup was used to conduct galvanic corrosion experiments over a range of Cu:CS area ratios from 1:1 to ~2500:1 with a high degree of radial symmetry. External coupling of the Cu and CS electrodes through a zero-resistance ammeter allowed for measurement of the galvanic current and coupled potential simultaneously; measurements were taken until steady-state was achieved.

The galvanic current density on CS was found to increase linearly with increasing Cu:CS area ratio while the coupled potential increased logarithmically. Coupled potential and galvanic current density values extracted from the intersection of Cu and CS PDP curves mirrored the trends from galvanic coupling experiments. PDP curves also revealed that the cathodic reaction on Cu, O₂ reduction, was under mass transport control and at its limiting current at all Cu:CS area ratios, which suggests that O₂ reduction was rate-controlling. As the Cu:CS area ratio increased, the proportion of O₂ reduction which occurred on the CS decreased, such that when the Cu:CS area ratio was greater than 100:1, the coupled potential was in or beyond the Tafel region of the CS anodic curve, where cathodic activity on the CS was negligible.

In the study of the effects of Cl⁻, the [Cl⁻] was found to have a great effect on the O₂ solubility, such that very low [Cl⁻] was associated with highly oxidizing conditions. The resulting low conductivity at low [Cl⁻] was also associated with a significant decrease in galvanic current density. This decrease was likely caused in part by a constriction of galvanic throwing power, though at the lowest Cl⁻ levels (0.001 M), apparent passivation of the CS surface also contributed to suppression of galvanic current.

Bentonite clay, a key barrier in the DGR which will be in intimate contact with the used fuel container, is expected to have a significant influence on the Cu/CS galvanic couple formed at a through-coating defect. Studies were conducted in the presence of layers of bentonite clay slurry

in order to determine effects of the bentonite clay chemistry on the galvanic corrosion of the Cu/CS couple. With the addition of an obstructing layer (5 mm) of bentonite slurry, the galvanic current density remained linearly dependent on Cu:CS area ratio and the coupled potential increased logarithmically, just as it had in the absence of bentonite. However, the coupled potential showed a large negative shift, and the galvanic current density decreased by an order of magnitude in the presence of bentonite, indicating a decrease in the rate of O₂ diffusion to the electrode surfaces. Increasing the thickness of the bentonite slurry layer beyond 5 mm did not continue to produce significantly more benign corrosion conditions, but rather a plateau in E_g and i_g was observed. From EIS measurements, it was determined that the impedance on CS increased with bentonite layer thickness, however, impedance on the Cu mirrored the plateau i_g observed previously. Thus, this plateau was attributed to the bentonite causing a large decrease in diffusion rate of O₂ to the Cu, which resulted in much greater impedance than any increase in impedance on CS due to bentonite. Despite the obstruction of O₂ diffusion, even the thickest (~20 mm) layer of bentonite failed to produce anoxic conditions at the surfaces of the Cu and CS electrodes. The obstructing layer of bentonite also prevented deposition of ferric oxide and oxyhydroxide species on the CS surface, instead forming a very thin magnetite film and corroding preferentially through grain etching and pitting.

A defect through the Cu coating would introduce a constrained geometry and therefore local differences in chemistry within the defect. Additionally, the Cu/CS interfaces are very different depending on the surface treatment required for application of electrodeposited or cold sprayed coatings. 14-day corrosion experiments were conducted using Cu-coated CS samples with small holes drilled through the Cu coating, in the presence and absence of bentonite slurry, and X-ray micro-CT was used to monitor the corrosion propagation within the defect in three dimensions.

The addition of bentonite led to a significant decrease in the corrosion rate of the CS at the base of the defect, as determined by volumes loss calculations of 3D reconstructions of the corroded region and confirmed by R_P measurements. Both the cold sprayed and the electrodeposited Cu/CS interfaces were more reactive than the bulk CS due to plastic deformation of the CS before coating application. This resulted in interfacial corrosion proceeding at a much higher rate than penetration into the CS. This phenomenon was also assisted by the development of local acidity in the crevice formed by interfacial corrosion and a stronger galvanic effect at the interface. In the absence of

bentonite, the CS was able to form a semi-protective film, though the formation event was stochastic and not always observed, while such an event was not observed at all in the presence of bentonite, likely due to the low coupled potential and retention of corrosion products in the bentonite clay. Corrosion products, primarily lepidocrocite, were found on the CS samples at the bases of the defects, but only in the absence of bentonite were corrosion products observed atop the Cu coating, which implied that ferrous and ferric species were being retained in the bentonite clay near the CS surface.

Ultimately, it was shown that even the addition of small amounts of bentonite slurry, which has relatively high hydraulic conductivity and minimal swelling pressure, could create very benign conditions for galvanic corrosion and very low corrosion rates compared to bentonite-free conditions. The obstruction of O₂ diffusion to the Cu surface lowered the rate of O₂ reduction, which was the rate-controlling reaction for Cu/CS galvanic corrosion. The presence of a compacted bentonite clay buffer box, with very low hydraulic conductivity, will likely slow the galvanic corrosion rate of the CS even further, due to both constriction of galvanic throwing power and the increasingly tortuous path for O₂ diffusion. However, the preference for localized corrosion may increase, as was seen in the presence of bentonite slurry. Galvanic corrosion at a through coating defect will depend on multiple criteria being simultaneously met: a significant defect through the entire thickness of the Cu coating, which escaped detection, oxidizing conditions (O₂ or some other oxidant present in the DGR) and an environment, to which both the CS and Cu are exposed, that provides an ionically conductive path between the dissimilar metals. These conditions are unlikely to be met in the DGR, given the short-lived O₂ inventory and very slow diffusion of any remotely produced oxidants, the very slow ingress of conductive groundwater and the ability of bentonite clay to retain that water in its layered structure, and the careful inspection of the containers which will be undertaken before container emplacement.

6.2 Future Work

This research built primarily on the work of Dr. Thalia Standish on galvanic corrosion at coating defects [1], and laid the groundwork for future investigation of interactions between the Cu/CS galvanic couple and bentonite clay. Moving forward with this research, it would be of great value to focus on the following areas:

- Further investigation of galvanic corrosion in low-conductivity environments in order to deconvolute the effects of constriction of galvanic throwing power and CS passivation on the decrease in galvanic corrosion rate. Such an endeavour could be achieved by replacing O_2 with an oxidant that is a solution-borne, neutral molecule, such as H_2O_2 . These experiments could be performed in constantly Ar-sparged, low conductivity solution over a range of Cu:CS area ratios with various concentrations of the oxidant. Constant sparging would be required to drive out O_2 generated via H_2O_2 decomposition (if that is the oxidant used). By monitoring changes in i_g and corrosion film properties, the effects of galvanic throwing power and oxidant concentration can be elucidated.
- Experimental and computational studies of the potential profiles across the Cu and CS surfaces at different area ratios should be performed in the presence and absence of bentonite slurry. Microelectrodes arranged across the Cu and CS electrode surfaces could be used to independently measure local redox potentials, and those measurements could be used to create a potential map of the galvanic effect as a function of distance from the Cu/CS bimetallic junction. These data could assist in determining throwing power under a given set of conditions, such as in low solution conductivity or under bentonite slurry, and to predict what the Cu:CS area ratio might be at the scale of a realistic through-coating defect in a UFC.
- Further investigation into the interactions between ferrous and ferric species and bentonite clay would be highly beneficial. Mössbauer spectroscopy, X-ray fluorescence spectroscopy, and X-ray diffraction [2] should be used to study the degree to which Fe ions or small Fe (oxyhydr)oxide crystals are retained in the clay and the effect that these species have on the properties of the clay as corrosion proceeds.
- Studies focusing on sulfide-related corrosion of the Cu/CS galvanic couple should be performed, considering that HS^- , which will be produced remotely by sulfate-reducing bacteria, will act as a long-term oxidant after the trapped O_2 has been consumed. Both Cu and CS interact strongly with HS^- and S^{2-} , so it would be valuable to investigate how the Cu/CS galvanic couple will behave in the presence of these species. Galvanic corrosion studies, like those performed in Chapter One of this thesis, could be performed to establish trends of coupled potential and galvanic current density over time in the presence of HS^- . Then, artificial coupling (as in Chapter Two of this thesis), followed by cathodic stripping

voltammetry and surface analysis, could give insight into which sulfide species formed on the CS and Cu, and the nature of the galvanic couple under those conditions.

- Continuing studies of galvanic corrosion at a through-coating defect should be performed in saturated compacted bentonite in order to determine the feasibility of forming a galvanic couple under such conditions, i.e. the formation of an ionically conductive path form between the Cu and CS through either leakage from the bentonite or forceful entry of bentonite into the defect as a result of swelling pressure. These experiments would likely be long-term and performed under pressure. X-ray micro-CT could be used to analyze samples corroded for different amounts of time in order to determine when galvanic corrosion starts, as well as the CS corrosion rates.

Finally, the purpose of this body of research is to supplement the development of finite element computational models which will be used to predict the long-term ($>10^5$ years) corrosion of the used nuclear fuel container. Such predictive models can help quantify the risks related to each of the corrosion processes which may compromise the used nuclear fuel container during its underground containment.

6.3 References

1. T. E. Standish. Galvanic corrosion of copper-coated carbon steel for used nuclear fuel containers. The University of Western Ontario, London, Canada, 2019.
2. A. Komlósi, E. Kuzmann, N. M. Nagy, Z. Homonnay, S. Kubuki, *Clays Clay Miner.* **2007**, *55*, 89-95.

Copyright and Permissions

Copyright

The content in the *Journal of The Electrochemical Society* is protected by copyright. It is published on behalf of ECS by IOP Publishing Limited.

The *Journal of The Electrochemical Society* is a hybrid journal. You can therefore choose whether you publish your article on a subscription or a gold open access basis.

Upon submission of an article, authors are requested to complete a copyright and publication agreement. Where an article is published on a subscription basis, copyright is transferred to The Electrochemical Society if the article is accepted. If the article is published on a gold open access basis then the author grants an exclusive licence to publish. We require a copyright form whether the article will be published on a gold open access or a subscription basis.

Subscription Articles

You may choose to publish your article on a subscription basis (part 1 of the copyright form).

Subscription articles are fully protected by copyright. Original content from them can only be used in accordance with <https://publishingsupport.iopscience.iop.org/questions/electrochemical-society-ecs/>.

Gold Open Access Articles

You may choose to publish your article on a gold open access basis (part 2 of the copyright form).

Where an article is being published on a gold open access basis, the author grants ECS and IOP Publishing a royalty-free, exclusive, freely transferrable, worldwide, perpetual licence for the full term of copyright.

Gold open access articles are made available under the Creative Commons Attribution 4.0 International licence (CC BY 4.0) (<https://creativecommons.org/licenses/by/4.0/>), the Creative Commons Attribution NonCommercial NoDerivatives 4.0 International licence (CC BY-NC-ND 4.0) (<https://creativecommons.org/licenses/by-nc-nd/4.0/>) or any successor to that licence.

If you are unsure whether the article from which you wish to use content is gold open access, it should have a red box with OPEN ACCESS at the top of the first page and the licence type (CC BY) at the bottom of the first page.

Please note you must still obtain express permission from the copyright owner to reuse any third-party content contained within an article.

Permissions

Users who wish to make use of content in any way not permitted above will require IOP Publishing's permission.

For permission to make multiple copies of articles, include material in coursepacks or to share articles via email or the Intranet, please obtain permission via the CCC. Before doing so, check that your institution does not already have a licence in place permitting the use you plan to make.

Curriculum Vitae

Lindsay Braithwaite

EDUCATION

M.Sc. Physical/Analytical Chemistry **2018 to present**

The University of Western Ontario

- NSERC Canada Graduate Scholarship (Master's) recipient
- Ontario Graduate Scholarship recipient
- Winner of an EFC Student Travel Grant for Nuclear Corrosion Summer School
- Travel sponsorship to CNA Conference and Trade Show 2020
- Western Science Entrance Scholarship recipient

B.Sc. (Hons.) Chemistry **2013 to 2018**

The University of Western Ontario

- Western Scholarship of Excellence recipient
- Dean's List

PUBLICATIONS

T. E. Standish, **L. J. Braithwaite**, J. J. Noël, D. W. Shoesmith, Influence of Area Ratio and Chloride Concentration on the Galvanic Coupling of Copper and Carbon Steel, *J. Electrochem. Soc.*, 166, 2019, C1-C8.

RESEARCH

Galvanic Corrosion of Copper-Coated Steel Used Nuclear Fuel Containers **2018 to present**

Graduate Researcher, The University of Western Ontario

Supervised by Dr. James Noël

Corrosion of Simulated Used Nuclear Fuel (SIMFUEL) in the Presence of H₂O₂ **2017 to 2018**

Undergraduate Researcher, The University of Western Ontario

Supervised by Dr. James Noël and Dr. David Shoesmith

PROFESSIONAL EXPERIENCE

Innovation Catalyst (Engineering Projects), Nuclear Promise X **present**

Graduate Teaching Assistant, The University of Western Ontario **2019**

Analytical Chemistry Lab Technician, Parmalat London R&D **2016 to 2017**

Server, Boston Pizza Markham **2015 to 2016**

Coach, Markham Gymnastics Club

2009 to 2016

VOLUNTEER EXPERIENCE

Section Officer (Secretary), National Association of Corrosion Engineers (NACE) 2019 to 2020

Volunteer, Let's Talk Science 2018 to present

Hackathon Participant, Nuclear Innovation Institute 2019

Volunteer, Thames Valley Science and Engineering Fair 2019

Volunteer, The University of Western Ontario 2019

Varsity Athlete, The University of Western Ontario 2013 to 2017

GRADUATE COURSEWORK AND WORKSHOPS

Electrochemistry (Dr. James Noël), The University of Western Ontario 2020

Surface Science (Dr. Lyudmila Goncharova), The University of Western Ontario 2019

Spectroscopy and Microscopy in Materials Research (Dr. Francois Lagugné-Labarthe),
The University of Western Ontario 2018

Design-Driven Innovation (Dr. Darren Meister), The University of Western Ontario 2019

Nuclear Corrosion Summer School (various lecturers), EFC/MEACTOS/WP4 2019

PRESENTATIONS

Oral Presentations

- Corrosion of Carbon Steel Galvanically Coupled to Copper in Clay Media in the Disposal of Used Nuclear Fuel
Lindsay Braithwaite, Katarina Albrechtas, Dmitrij Zagidulin, David Shoesmith, James Noël
UNENE Workshop, 2019, Toronto, Canada
- Corrosion of Carbon Steel Galvanically Coupled to Copper in Clay Media in the Disposal of Used Nuclear Fuel
Lindsay Braithwaite, Katarina Albrechtas, Dmitrij Zagidulin, David Shoesmith, James Noël
ECS Western Student Chapter Symposium, 2019 London, Canada
- The Role of the Copper-to-Steel Area Ratio in the Galvanic Corrosion of Steel in the Presence of Chloride
Lindsay Braithwaite, Thalia Standish, David Shoesmith, James Noël
NACE Northern Area Eastern Conference, 2019, Ottawa, Canada

- The Role of the Copper-to-Steel Area Ratio in the Galvanic Corrosion of Steel in the Presence of Chloride
Lindsay Braithwaite, Thalia Standish, David Shoesmith, James Noël
NACE Southern Ontario Student Section Research Symposium, 2019, London, Canada
- Galvanic Corrosion of Used Nuclear Fuel Containers Under Long-Term Disposal Conditions
Lindsay Braithwaite, Thalia Standish, David Shoesmith, James Noël
Electrochemical Society Student Chapter Research Symposium, 2018, London, Ontario
- The Effect of H₂O₂ on the Corrosion of Simulated Spent Nuclear Fuel
Lindsay Braithwaite, Ziyang Zhu, James Noël, David Shoesmith
Southern Ontario Undergraduate Student Chemistry Conference, 2018, Waterloo, Ontario

Poster Presentations

- Corrosion of Carbon Steel Galvanically Coupled to Copper in Clay Media Relevant to the Disposal of Used Nuclear Fuel
Lindsay Braithwaite, Katarina Albrechtas, Dmitriy Zagidulin, David Shoesmith, James Noël
UNENE Workshop, 2019, Toronto, Canada
- The Role of the Copper-to-Steel Area Ratio in the Galvanic Corrosion of Steel in the Presence of Chloride
Lindsay Braithwaite, Thalia Standish, David Shoesmith, James Noël
NACE Northern Area Eastern Conference, 2019, Ottawa, Canada
- The Role of the Copper-to-Steel Area Ratio in the Galvanic Corrosion of Steel in the Presence of Chloride
Lindsay Braithwaite, Thalia Standish, David Shoesmith, James Noël
NACE Southern Ontario Student Section Research Symposium, 2019, London, Canada
- The Role of the Copper-to-Steel Area Ratio in the Galvanic Corrosion of Steel in the Presence of Chloride
Lindsay Braithwaite, Thalia Standish, David Shoesmith, James Noël
Canadian Chemistry Conference and Exhibition, 2019, Quebec City, Canada

PROFESSIONAL AFFILIATIONS

Section Secretary, Student Member, National Association of Corrosion Engineers	2018 to 2020
Student Chapter Member, Electrochemical Society	2018 to 2020
Member, Women in Nuclear (Bruce Chapter)	2018 to 2020